

**A STUDY OF PROCESSING, MICROSTRUCTURE AND MECHANICAL
PROPERTIES OF ULTRA-HIGH STRENGTH MICROALLOYED STEEL HOT BAND
COILS FOR AUTOMOTIVE APPLICATIONS**

by

Bing Ma

B.S. in Materials Science and Engineering, Harbin Institute of Technology, China, 2011

Submitted to the Graduate Faculty of
Swanson School of Engineering in partial fulfillment
of the requirements for the degree of
Doctor of Philosophy

University of Pittsburgh

2017

UNIVERSITY OF PITTSBURGH
SWANSON SCHOOL OF ENGINEERING

This dissertation was presented

by

Bing Ma

It was defended on

July 14th, 2017

and approved by

Scott Mao, Ph.D., Professor, Mechanical Engineering and Materials Science

Ian Nettleship, Ph.D., Associate Professor, Mechanical Engineering and Materials Science

Patrick Smolinski, Ph.D., Associate Professor, Mechanical Engineering and Materials Science

Luis E. Vallejo, Professor, Ph.D., Civil and Environmental Engineering

Dissertation Director: Anthony J. DeArdo, Ph.D., Professor, Mechanical Engineering and

Materials Science

Copyright © by Bing Ma

2017

**A STUDY OF PROCESSING, MICROSTRUCTURE AND MECHANICAL
PROPERTIES OF ULTRA-HIGH STRENGTH MICROALLOYED STEEL HOT BAND
COILS FOR AUTOMOTIVE APPLICATIONS**

Bing Ma, Ph.D.

University of Pittsburgh, 2017

In the automotive industry, thin gauge high strength steels require not only good tensile ductility, but also good sheared edge ductility or a good hole expansion ratio (HER) value. These properties can be achieved through producing a microstructure consisting of a single-phase ferrite and strengthened by microalloyed precipitates. The objective of this current study was to develop a hot band steel with a ferrite-based microstructure with a tensile strength higher than 1200MPa, total elongation larger than 10%, good HER values and low temperature toughness. The steel being studied in this project has the following nominal composition (wt %): 0.14C, 0.35Mo, 0.163Ti and 0.294V. In this investigation, the relationship between the microstructure and mechanical properties with different finish rolling and coiling temperatures were explored. It was found that the finish rolling temperature did not have an obvious influence on either microstructure or mechanical properties. However, the coiling temperatures strongly affected both microstructure and mechanical properties. Steels with a coiling temperature of 610°C, exhibited predominately polygonal ferrite and a few acicular ferrite grains. The corresponding tensile strength was over 1200MPa, total elongation of about 20%; however, the low temperature toughness and HER were rather low. The fracture surface from broken CVN specimens shows nearly pure brittle fracture.

When the coiling temperature was reduced to 530°C, the microstructure appears to be a mixture of granular bainite and coarse quasi-polygonal ferrite grains. Here, the tensile strength drops to under 1000MPa, but the low temperature toughness and HER improve greatly. With a further lower coiling temperature of 450°C, the microstructure is a mixture of granular bainite, quasi-polygonal ferrite and upper bainite. In this case, the tensile strength increases to about 1100MPa, and the steels have intermediate low temperature toughness and HER. Studies showed that the high strength of the steels with the highest coiling temperature were due to the excessively formed fine precipitates at the coiling temperature of 610°; while the strength of steels with lower coiling temperatures originates predominately from dislocation strengthening. Because of the very high percentage of Ti and low amount of N, coarser TiN inclusions were formed in the liquid and in the interdendritic pools separating the dendritic δ ferrite grains. These hyper-stoichiometric TiN particles with a size larger than 3 microns can be observed throughout the steels. The relatively low toughness and HER values can be attributed, at least partially, to the large amount of coarse TiN inclusions found in all steel conditions. In addition, the low values found with 610°C coiling can be partly attributed to excessive precipitation hardening, while the low values found with 450°C coiling is the result of high levels of MA microconstituent. The scientific hypothesis guiding this study is that excessively large amounts of TiN particles are detrimental to toughness and sheared edge ductility (HER) in high strength steels.

TABLE OF CONTENTS

| | | |
|--------------|---|-----------|
| 1.0 | INTRODUCTION..... | 1 |
| 2.0 | BACKGROUND | 7 |
| 2.1 | THERMOMECHANICAL PROCESSING (TMP) | 7 |
| 2.1.1 | Austenite conditioning..... | 7 |
| 2.1.2 | Cooling rate | 13 |
| 2.1.3 | Finish cooling temperature | 15 |
| 2.2 | BAINITIC TRANSFORMATION..... | 17 |
| 2.2.1 | Transformation Mechanism | 19 |
| 2.2.2 | The Influential Factors on the Bainite Transformation..... | 24 |
| 2.3 | FORMATION OF MARTENSITE/AUSTENITE CONSTITUENT | 28 |
| 2.3.1 | The Formation Mechanism of M/A Constituent..... | 29 |
| 2.3.2 | The Influence Factors on the Formation of M/A Constituents | 29 |
| 2.4 | STRENGTHENING MECHANISM | 32 |
| 2.4.1 | Grain boundary strengthening..... | 33 |
| 2.4.2 | Solid solution strengthening..... | 35 |
| 2.4.3 | Transformation strengthening | 37 |
| 2.4.4 | Precipitation strengthening..... | 40 |
| 2.5 | DUCTILE FRACTURE MECHANISM..... | 43 |
| 2.6 | TOUGHNESS MECHANISM | 46 |

| | | |
|--------------|---|-----------|
| 3.0 | STATEMENT OF OBJECTIVE | 50 |
| 4.0 | MATERIALS AND EXPERIMENTAL PROCEDURE | 52 |
| 4.1 | MELTING, HOT ROLLING (THERMO-MECHANICAL) AND COOLING PROCESSING | 52 |
| 4.2 | MECHANICAL TESTING | 53 |
| 4.2.1 | Micro-hardness | 53 |
| 4.2.2 | Tensile test | 54 |
| 4.2.3 | Charpy V-notch test | 54 |
| 4.2.4 | Hole expansion test | 55 |
| 4.3 | MICROSTRUCTURE ANALYSIS | 56 |
| 4.3.1 | Optical microscopy | 57 |
| 4.3.2 | Scanning electron microscopy | 57 |
| 4.3.3 | Electron backscattered diffraction..... | 58 |
| 4.3.4 | Transmission electron microscopy | 58 |
| 5.0 | RESULT | 60 |
| 5.1 | MICROSTRUCTURES OF THE HOT BAND..... | 60 |
| 5.2 | MECHANICAL PROPERTIES OF THE HOT BANDS | 79 |
| 5.2.1 | Hardness test | 79 |
| 5.2.2 | Tensile test | 80 |
| 5.2.3 | Charpy V-notch impact test..... | 84 |
| 5.2.4 | Hole Expansion Test | 90 |
| 6.0 | DISCUSSION | 92 |
| 6.1 | THE EFFECTS OF THERMOMECHANICAL PROCESSING PARAMETERS ON THE MICROSTRUCTURE..... | 92 |
| 6.1.1 | The effect of the finish rolling temperature on the microstructure | 92 |

| | | |
|-------|---|-----|
| 6.1.2 | The effect of the coiling temperature on the formation of bainite and ferrite | 100 |
| 6.2 | THE INFLUENCE OF THE THERMOMECHANICAL PROCESSING PARAMETERS ON THE MECHANICAL PROPERTIES..... | 114 |
| 6.2.1 | The influence factors on the strength..... | 114 |
| 6.2.2 | The influence factors on the toughness..... | 128 |
| 6.2.3 | The influence factors on the hole expansion test results | 135 |
| 6.3 | EFFECT OF TIN PARTICLES ON THE MECHANICAL PROPERTIES OF THE STEELS..... | 139 |
| 6.4 | PRECIPITATION STRENGTHENING STUDY | 149 |
| 7.0 | CONCLUSION..... | 153 |
| 8.0 | FUTURE WORK..... | 156 |
| | BIBLIOGRAPHY..... | 158 |

LIST OF TABLES

| | |
|---|-----|
| Table 4.1: Chemical composition of the steel (wt%)..... | 52 |
| Table 4.2: Processing parameters of the steels | 53 |
| Table 5.1: Volume fraction and average size of M/A constituents..... | 73 |
| Table 5.2: Vicker's hardness of steel conditions, VHN(300gf)..... | 79 |
| Table 5.3: Tensile properties of the steels | 81 |
| Table 5.4: Absorbed energy of the Charpy V-notch impact test, J..... | 84 |
| Table 5.5: Shear Area Percentage of Fracture Surface | 87 |
| Table 5.6: Hole expansion ratio of the hot band steels..... | 90 |
| Table 6.1: Austenitic GB interfacial area per unit volume (S_v), mm^{-1} | 96 |
| Table 6.2: Grain Size from EBSD, μm | 98 |
| Table 6.3: Kernel Average Misorientation, $^\circ$ | 113 |
| Table 6.4: Dislocation density based on KAM, mm^{-2} | 114 |
| Table 6.5: Contribution from dislocation strengthening from EBSD data, MPa..... | 116 |
| Table 6.6: Strengthening contribution from different types of carbides precipitates, MPa..... | 120 |
| Table 6.7: Calculated volume fraction of TiN inclusions..... | 142 |
| Table 6.8: Volume fraction of precipitates during hot rolling with different CT (FRT 870°C). | 152 |

LIST OF FIGURES

| | |
|--|----|
| Figure 1.1: Schematic of different steel grades in an elongation vs. tensile strength map..... | 1 |
| Figure 1.2: Effect of different microstructures on the hole expansion ratio..... | 3 |
| Figure 1.3: Process for producing hot rolled high strength steel sheets with a high hole expanding ratio | 4 |
| Figure 2.1: Schematic of TMCP and microstructures evolution | 9 |
| Figure 2.2: Grain coarsening behavior of V and V-Ti steels during reheating..... | 9 |
| Figure 2.3: Effect of various of microalloying elements on the recrystallization stop temperature of austenite in a low carbon 1.4wt% Mn steel | 10 |
| Figure 2.4: Dependence of grain size and 50% shear FATT on the finish rolling temperature of pearlite-reduced steels alloyed with vanadium and columbium | 11 |
| Figure 2.5: Variation of ferrite grain size with effective austenite interface area per unit volume | 12 |
| Figure 2.6: Variation of austenite to ferrite transformation temperature with deformation below recrystallization temperature..... | 12 |
| Figure 2.7: Dependence of grain refinement ratio on austenite grain size and cooling rate..... | 14 |
| Figure 2.8: Effect of cooling rate from FRT of 1030 ~ to FCT on the ferrite grain size, yield stress, and toughness | 14 |
| Figure 2.9: Effect of finish rolling temperature on the ferrite grain size and yield strength | 15 |
| Figure 2.10: The effect of coiling temperature on the morphology of cementite..... | 16 |
| Figure 2.11: Continuous cooling transformation diagram for a Ni-Cr-Mo steel..... | 17 |
| Figure 2.12: Schematic CCT diagram of a Ni-Cr-Mo steel showing three forms of bainite..... | 18 |
| Figure 2.13: Gibbs free energy of different phases..... | 19 |

| | |
|--|----|
| Figure 2.14: (a)TEM of upper bainite of Si-Mn-Cr steel isothermally transformed at 400°C; (b)Microstructure of lower bainite; (c) Light micrograph of granular bainite in a Cr-Mo steel | 21 |
| Figure 2.15: Microstructure of (a) Inverse bainite; (b) Pearlite bainite; (c) Columnar bainite and (d) Grain boundary lower bainite | 23 |
| Figure 2.16: (a) Mn and (b) Cr influence on the transformation of bainite | 25 |
| Figure 2.17: (a) Influence of PAGES and austenitization temperature on the transformation of bainite; (b) Influence of the austenitization temperature on the bainite transformation | 25 |
| Figure 2.18: Influence of cooling rate on the transformation of bainite | 27 |
| Figure 2.19: Schematic showing carbon concentration gradient at the interface of ferrite and austenite during (a) rapid cooling and (b) slow cooling | 28 |
| Figure 2.20: (a)Influence of carbon on the formation of M/A; (b) Influence of Mo and Mn on the formation of M/A | 30 |
| Figure 2.21: Morphologies of M/A constituents under different cooling rate..... | 31 |
| Figure 2.22: Schematic diagram of granular bainite resulted from ferrite | 32 |
| Figure 2.23: Effect of ferrite grain size on yield strength and impact toughness | 34 |
| Figure 2.24 : Solid solution strengthening mechanism..... | 36 |
| Figure 2.25: Solid solution strengthening of ferrite..... | 37 |
| Figure 2.26: Strength variation with temperature of maximum transformation rate in steels with 0.1 wt% carbon after Pickering | 38 |
| Figure 2.27: (a) Tensile strength of DP steel as a function of volume fraction of martensite with different carbon concentration; (b) Effect of carbon on the tensile strength of martensite | 39 |
| Figure 2.28: Effect of aging time on the yield strength for precipitation in FCC systems such as aluminum alloys | 42 |
| Figure 2.29: The stages in the ductile fracture of a tensile test specimen | 44 |
| Figure 2.30: Theoretical models for void growth (a) Decohesion (Prolate Spheroid); (b) Decohesion (Oblate Spheroid); (c) Particle Cracking..... | 46 |
| Figure 2.31: Energy absorbed in a tensile test with different steels | 47 |
| Figure 2.32: Charpy V-notch result of different materials at different temperature..... | 48 |

| | |
|---|----|
| Figure 4.1: Thermo-mechanical processing..... | 52 |
| Figure 4.2: Schematic of hole expansion test | 56 |
| Figure 5.1: Optical microstructure of steels at finish rolling temperature of 870°C with coiling temperatures of (a) 610°C; (b) 530°C; (c) 450°C | 62 |
| Figure 5.2: Optical microstructure of steels at finish rolling temperature of 810°C with coiling temperatures of (a) 610°C; (b) 530°C; (c) 450°C | 63 |
| Figure 5.3: Optical microstructure of steels at finish rolling temperature of 750°C with coiling temperatures of (a) 610°C; (b) 530°C; (c) 450°C | 64 |
| Figure 5.4: Scanning electron microstructure of steels at finish rolling temperature of 870°C with coiling temperatures of (a) and (b) 610°C; (c) and (d) 530°C; (e) and (f) 450°C..... | 65 |
| Figure 5.5: Scanning electron microstructure of steels at finish rolling temperature of 810°C with coiling temperatures of (a) and (b) 610°C; (c) and (d) 530°C; (e) and (f) 450°C..... | 66 |
| Figure 5.6: Scanning electron microstructure of steels at finish rolling temperature of 750°C with coiling temperatures of (a) and (b) 610°C; (c) and (d) 530°C; (e) and (f) 450°C..... | 67 |
| Figure 5.7: Optical microstructure of steels at finish rolling temperature of 870°C with coiling temperatures of (a) 610°C; (b) 530°C; (c) 450°C | 70 |
| Figure 5.8: Optical Microstructure of steels at finish rolling temperature of 810°C with coiling temperatures of (a) 610°C; (b) 530°C; (c) 450°C | 71 |
| Figure 5.9: Optical Microstructure of steels at finish rolling temperature of 750°C with coiling temperatures of (a) 610°C; (b) 530°C; (c) 450°C | 72 |
| Figure 5.10: Morphology of carbide of steels with coiling temperature of (a) 530°C; (b) 450°C | 73 |
| Figure 5.11: Observation of M/A in the steels with coiling temperature of (a) 610°C; (b) 530°C; (c) 450°C | 74 |
| Figure 5.12: Observation of inclusions on the surface of an as polished specimen | 75 |
| Figure 5.13: SEM/EDAX results of coarse inclusions | 76 |
| Figure 5.14: SEM/EDAX results of fine inclusions | 76 |
| Figure 5.15: GBCD of steels with finish rolling temperature of (a) 870°C; (b) 810°C; (c) 750°C | 78 |
| Figure 5.16: Vicker's hardness number of steel condition | 79 |
| Figure 5.17: Engineering strain-stress curve of steels (a) 870°C; (b) 810°C; (c) 750°C..... | 82 |

| | |
|--|-----|
| Figure 5.18: Tensile strength of the hot band steels | 83 |
| Figure 5.19: Absorbed energy of Charpy impact test result | 85 |
| Figure 5.20: Relationship between absorbed energy and tensile strength | 85 |
| Figure 5.21: Optical micrograph of Charpy V-notch specimens fracture surface with finish rolling temperature of (a) 870°C; (b) 810°C; (c) 750°C. The coiling temperature decreases from left to right..... | 86 |
| Figure 5.22: Relationship between the shear area percentage and absorbed energy | 87 |
| Figure 5.23: SEM micrographs of fracture surface of steels with a coiling temperature of (a) 610°C; (b) 530°C; (c) 450°C..... | 88 |
| Figure 5.24: Observation of TiN on the fracture surface of Charpy specimens | 89 |
| Figure 5.25: Optical micrograph of hole expansion specimens with a coiling temperature of (a) 610°C; (b) 530°C; (c) 450°C..... | 90 |
| Figure 5.26: Higher magnification of the crack on the surface of steel with a coiling temperature of 610°C. Note the long surface crack with little hole expansion. | 91 |
| Figure 6.1: Optical microstructure of prior austenite grains with a finish rolling temperature of (a) 870°C; (b) 810°C; (c) 750°C..... | 95 |
| Figure 6.2: Techniques for measuring the SV value in interconnected and discontinuous systems | 96 |
| Figure 6.3: The general effect of microalloying additions on the grain coarsening temperature of austenite in C-Mn steels containing a volume fraction of 0.0005 of alloy carbide or nitride | 97 |
| Figure 6.4: Accumulated grain area fraction curve of steels at coiling temperature of (a) 610°C; (b) 530°C; (c) 450°C..... | 99 |
| Figure 6.5: Continuous cooling transformation diagram..... | 101 |
| Figure 6.6: Image quality map and inverse pole figures of the steels with a finish rolling temperature of 870°C at a coiling temperature of (a) 610°C; (b) 530°C; (c) 450°C . | 107 |
| Figure 6.7: Image quality map and inverse pole figures of the steels with a finish rolling temperature of 810°C at a coiling temperature of (a) 610°C; (b) 530°C; (C) 450°C. | 108 |
| Figure 6.8: Image quality map and inverse pole figures of the steels with a finish rolling temperature of 750°C at a coiling temperature of (a) 610°C; (b) 530°C; (C) 450°C. | 109 |
| Figure 6.9: Misorientation angle of steels with finish rolling temperature of (a) 870°C; (b) 810°C; (c) 750°C | 110 |

| | |
|---|-----|
| Figure 6.10: Kernel average misorientation map of steels with (a) finish rolling temperature 870°C, coiling temperature 610°C; (b) finish rolling temperature 870°C, coiling temperature 530°C; (c)) finish rolling temperature 870°C, coiling temperature 450°C; (d) finish rolling temperature 810°C, coiling temperature 610°C; (e) finish rolling temperature 810°C, coiling temperature 530°C; (f)) finish rolling temperature 810°C, coiling temperature 450°C; (g) finish rolling temperature 750°C, coiling temperature 610°C; (h) finish rolling temperature 750°C, coiling temperature 530°C; (i) finish rolling temperature 750°C, coiling temperature 450°C | 111 |
| Figure 6.11: KAM map of point to point misorientation..... | 112 |
| Figure 6.12: Subgrain structure within quasi-polygonal ferrite grain from EBSD (a) IPF; (b) zoomed IPF; (c) KAM of the zoom area..... | 112 |
| Figure 6.13: KAM results ° (a) 610°C; (b) 530°C; (C) 450°C | 113 |
| Figure 6.14: Engineering stress-strain curve zoomed in with a finish rolling temperature of 870°C | 116 |
| Figure 6.15: Yield ratio bar chart of all the steels..... | 118 |
| Figure 6.16: JMatPro calculation of volume fraction and particle size of carbides at different holding temperatures (a) 610°C; (b) 530°C; (C) 450°C | 119 |
| Figure 6.17: Optical micrograph of 30% cold rolled steel with a finish rolling temperature of 870°C and coiling temperature of 610°C aged at 600°C for (a) 0min; (b) 10min; (c) 30min; (d) 60min; (e) 120min; (f) 240min | 123 |
| Figure 6.18: Optical micrograph of 30% cold rolled steel with a finish rolling temperature of 870°C and coiling temperature of 530°C aged at 600°C for (a) 0min; (b) 10min; (c) 30min; (d) 60min; (e) 120min; (f) 240min | 124 |
| Figure 6.19: Optical micrograph of 30% cold rolled steel with a finish rolling temperature of 870°C and coiling temperature of 450°C aged at 600°C for (a) 0min; (b) 10min; (c) 30min; (d) 60min; (e) 120min; (f) 240min | 125 |
| Figure 6.20: Vicker’s hardness number of the cold rolled and aged steels with a finish rolling temperature of 870°C and a coiling temperature of (a) 610°C; (b) 530°C; (c) 450°C | 126 |
| Figure 6.21: Fracture surface on the tensile specimens with a finish rolling temperature of 750°C and a coiling temperature of (a) 610°C; (b) 530°C; (c) 450°C | 127 |
| Figure 6.22: Observation of TiN on the fracture surface of a tensile specimen | 128 |
| Figure 6.23: Accumulated grain area fraction curve of steels at finish rolling temperature of (a) 870°C; (b) 810°C; (c) 750°C..... | 130 |

| | |
|---|-----|
| Figure 6.24: Variation in (a) hardness and (b) impact energy of 7020 alloy specimens aged at 413 K for various times following 96 h natural ageing | 131 |
| Figure 6.25: Optical micrograph of secondary crack through prior austenite grains | 133 |
| Figure 6.26: Optical micrograph of secondary crack through ferrite grains..... | 134 |
| Figure 6.27: Cleavage initiation site on the fracture surface of Charpy specimens | 135 |
| Figure 6.28: Optical micrograph of crack path on the surface of specimen with a coiling temperature of 610°C | 136 |
| Figure 6.29: SEM micrograph of crack path on the surface of specimen with a coiling temperature of 610°C | 137 |
| Figure 6.30: SEM micrographs of fracture surface specimen with a coiling temperature of 610°C | 138 |
| Figure 6.31: (a) HER of the hot band coil, cold rolled piece and cold rolled and aged piece; (b) Optical pictures of the hole expansion specimens after test | 139 |
| Figure 6.32: Phase diagram from JMatPro calculation..... | 141 |
| Figure 6.33: Comparison of optical micrograph in (a) bright field and (b) dark field | 143 |
| Figure 6.34: Dark field optical micrograph of (a) slab; (b) hot band steel | 144 |
| Figure 6.35: SEM micrographs of inclusions in the slab..... | 144 |
| Figure 6.36: SEM micrographs of inclusions in the hot band | 145 |
| Figure 6.37: SEM micrographs of TiN inclusions on the fracture surface of (a) tensile specimen; (b) Charpy specimen; (c) hole expansion specimen | 146 |
| Figure 6.38: Contour map of Charpy transition temperature obtained by the polynomial expression in steel with 0.02wt% Sol.Al | 147 |
| Figure 6.39: Influence of (a) TiN volume fraction and (b) TiN spacing on the fracture toughness | 148 |
| Figure 6.40: Relationship between fracture toughness and allowable stress and crack size | 149 |
| Figure 6.41: Dark field OM of steels with a coiling temperature of 610°C and finish rolling temperature of (a) 870°C; (b) 810°C; (c) 750°C..... | 150 |
| Figure 6.42: TEM micrograph of carbon replica of a steel with finish rolling temperature of 870°C and coiling temperature of 610°C at different magnifications..... | 152 |

Figure 6.43: TEM carbon replica of precipitates in steel with a coiling temperature of (a) 610°C;
(b) 530°C; (c) 450°C 152

1.0 INTRODUCTION

The steel industry and its products have been developing for hundreds of years, evolving from high or mild carbon steel to plain carbon steel to microalloyed steel to achieve better ductility, toughness and weldability, and also maintain or improve the strength and performance at the same time ^[1, 2]. For different purpose of applications, i.e. structural steel, pipeline steel, tool steel, rail steel, etc., a corresponding chemical composition, hot rolling, heating treatment and forming process can be applied in the manufacturing. Figure 1.1 is the schematic of the distribution of different types of steels used in the automotive industry in a total elongation versus tensile strength map.

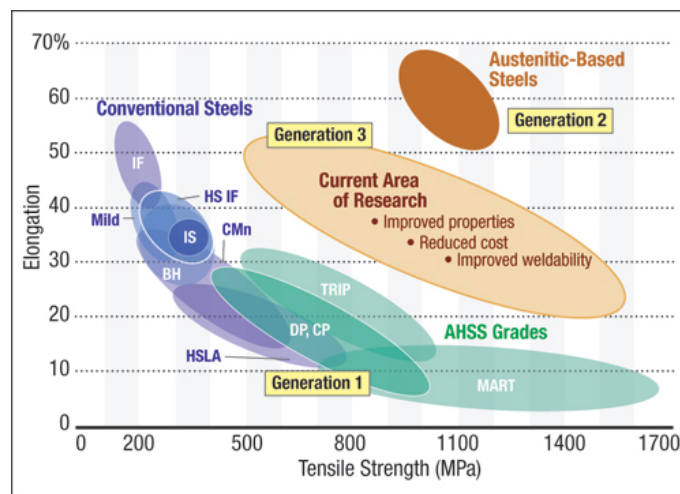


Figure 1.1: Schematic of different steel grades in an elongation vs. tensile strength map

From Figure 1.1, it can be observed the steels are mostly being divided into three categories or generations. In the first generation steels, the advanced high strength steels (AHSS) such as dual-phase, TRIP assisted and complex phase steels clearly have their advantage in the strength when compared with the other conventional steels, and still have acceptable ductility. Especially in the automotive industry, in order to achieve more weight reduction in the body-in-white (BIW), and remain high strength without any degradation of crash performance in the meantime, various types of the AHSS have been adopted over the past decades to achieve a better balance of low cost, light weight and mechanical properties^[3-6]. However, there are several factors hindering the broad application of the AHSS, such as high production cost, poor formability, poor shape fixability, weldability problems, delayed fracture and coating problems of hot dip Zn coated steels sheets^[7]. Compared with conventional HSLA steels, whose microstructure is comprised mostly of ferrite and pearlite, the yield strength ranges from 300MPa to 420MPa and tensile strength from 384MPa to 500MPa^[8], the AHSS can provide much higher strength, generally with yield strength over 300MPa and tensile strength over 600MPa^[4], including dual phase (DP) steels, transformation induced plastic (TRIP) steels, complex phase (CP) steels and martensitic (MART) steels. It has been well demonstrated that the higher strength in the AHSS is due to the combination of grain refinement, solid solution strengthening, dislocation (transformation) strengthening and precipitation strengthening. However, because of the limitation of the ductility of the AHSS, especially for the local or edge stretchability, further improvement still needs to be done before this family of steels finds wider applications in automotive manufacturing^[4].

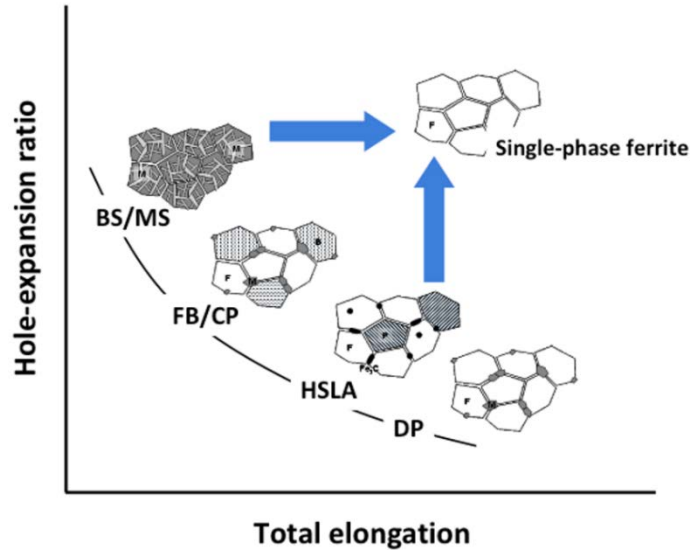


Figure 1.2: Effect of different microstructures on the hole expansion ratio

As Figure 1.2 shows, although DP 580, DP 980 are all successfully commercialized, and have a good combination of the strength and ductility, but because of the large strength/hardness difference between the martensite and ferrite, the hole expansion ratio is unsatisfactory^[9, 10]. In addition, the boron bearing martensitic steels manufactured by hot stamping, have a good combination of reduced weight, improved safety, crashworthiness quality and surface corrosion protection^[11, 12], and have been regarded as an alternative technology to the conventionally produce cold formed AHSS automotive parts^[13]. Their limited ductility is not a problem since they are hot stamped to the final size and shape before being in-die quenched to room temperature. These hot stamped steels are successfully used in bumper and A, B pillars in the BIW.

Recently, in a major shift in design philosophy, JFE STEEL (Japan) has developed a NANO-HITEN steel with single ferritic matrix with nano-sized (Ti, Mo)C precipitates within grains or on the grain boundaries. It has been claimed in the literature that these steels can reach an ultimate tensile strength (UTS) of 805MPa, with 20% elongation (TEL) and 100% hole expansion ratio (HER)^[14]. A little later, TATA STEEL (Europe) produced a steel grade called XPF1000 with

single ferritic matrix and has a UTS over 950MPa due to the Nb, V, Mo nano-precipitates and fine ferrite grain size. In this case, it was claimed that precipitation hardening made a contribution to strength of 466MPa^[15]. Both of these new steels were produced as hot band coils of gauge 3-4mm through conventional thermomechanical processing (hot rolling, water spray cooling and coiling to room temperature). Because of the single phase ferrite microstructure, i.e., the absence of hard bainite and/or martensite, these steels show superior local elongation (HER).

However, in order to produce hot rolled steels with even higher strength, approaching strength in the Giga Pascal range, alloying composition and thermal mechanical processing had to be redesigned. As shown in Figure 1.3^[16], this new process was designed to produce very high strength hot rolled steel sheet coils with a high hole expansion ratio. High Ti was added to low carbon steels to form TiC precipitates during or just after ferrite transformation during coiling to help provide the required strength.

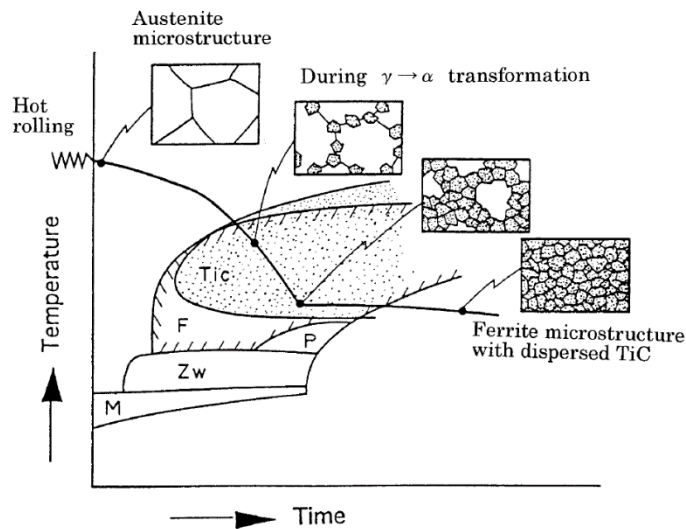


Figure 1.3: Process for producing hot rolled high strength steel sheets with a high hole expanding ratio

In the research described here, a new chemical composition and different thermomechanical processing were designed to manufacture high strength steel hot band coils

with 3mm thickness. The relationships between the microstructures, mechanical properties, finish rolling temperature and coiling temperature were investigated in this study.

The finish rolling temperature is important to the microstructure and mechanical properties of the steels. Different finish rolling temperature could result in different levels of precipitation in austenite and possibly influence the final grain size. In addition, the different strain levels introduced into the steel before coil cooling caused by the different finishing temperatures will affect both the CCT curve for the transformation, and the kinetics of both the phase transformation and precipitation during coil cooling^[17-19]. Usually, the low finish rolling temperature will end up with higher strength because of the higher dislocation density it brought into the steel, which would speed up the transformation leading to finer microstructures, and also promote the nucleation of the precipitates.

The coiling temperature is normally obtained by water spray cooling at approximately 30°C/s from the finish rolling temperature to the designated temperature, at which time the hot band is wrapped into a coil. The coil then cools to room temperature at about 30°C/h.

Typically, the strength increases with lower coiling temperatures, mainly because low coiling temperatures can produce low temperature transformation products which may contain more defects like dislocations, sub-grain boundaries and cause higher strength. Also, lower coiling temperatures would result in finer precipitates, as long as the diffusion rates are adequately high. The large temperature drop from austenite at the finishing temperature to ferrite at the coiling temperature will produce microstructures with supersaturated compositions due to the lower solubility of C, N, V and Ti at lower temperatures. Therefore, assuming sufficient diffusivity, this supersaturation will drive the formation of precipitates during the slow cooling or aging, and cause extra strength to the steel. However, if the coiling temperature is too low, according to the

formation mechanism of the precipitation and the role of diffusivity, the precipitates are not likely to form, even though the matrix is over saturated with excess microalloying elements. Moreover, two major precipitates in the steels are carbides and nitrides, even just for one type, different carbide alloying elements will have distinctively different solubility over temperatures or phases. Therefore, depending on the alloying elements put into the steel, and what kind of precipitates need to be formed within that phase, a proper coiling temperature can be chosen.

The different contributions from the microstructures, precipitation and dislocations and/or inclusions to the final strength and toughness will be discussed in this thesis.

2.0 BACKGROUND

2.1 THERMOMECHANICAL PROCESSING (TMP)

Steels can be processed to have variety of microstructures and related properties. Depending on the desired microstructures, even with the same chemical composition, different heating and cooling paths can be designed to accomplish that. The whole thermomechanical processing treatment begins with the austenitization or reheating phase, followed by roughing and finishing passes and to the final cooling and coiling. HSLA steels require good toughness and high strength, and the strength is associated with different strengthening mechanisms, of which the most effective way is through microstructure refinement ^[20-23].

2.1.1 Austenite conditioning

The change in the austenite grain size, shape and defect structures from austenitization, to high temperature roughing passes to lower temperature finishing passes can provide a lot of information about the influence of the process parameters. Having a good understanding of the austenite grain size can be helpful to optimize the procedure. And a small prior austenite grain size can result in a fine microstructure at room temperature with good mechanical properties. Austenite grain size can be affected by the austenitizing temperature, rolling temperature and rolling strain and strain rate.

Figure 2.1 shows the microstructure evolution during hot deformation^[24]. During the reheating treatment, ideally, most of the alloying elements will dissolved in the solid solution, and the segregated elements will be redistributed, the steel becomes homogenized. According to V. J. Pogorzelsky^[25], when comparing plain carbon steel with vanadium or niobium bearing steels in the reheating experiment, it was found that higher reheating temperature results in a higher strength in microalloyed steels, but the effect was minimum in the plain carbon steels, that was because the higher reheating temperature is associated with more complete solution of microalloying elements in the austenite. These dissolved elements then act to increase the strength through hardenability, solute drag and precipitation effects.

However, the austenitizing temperature should not be too high to avoid the coarsening of the austenite grains. To achieve that, microalloying elements, like V, Ti, N were added to the steel. Since the nitrides can precipitate at very high temperature, they can be very effective at pinning the austenite grain boundaries. Figure 2.2 shows the reheating temperature vs. the austenite grain size for different microalloyed steels^[26], it can be seen that the adding of microalloying element can increase the grain coarsening temperature (T_{GC}), especially Ti; adding Ti to the V-N steel can form fine and stable TiN particles and inhibit the austenite grain boundaries movement. The increase of the T_{GC} temperature can expand the operation window for the roughing passes to form small, recrystallized austenite grains.

Once the steels cool down to the roughing temperature, the deformation will turn the austenite grains into a smaller equiaxed grains as a result of a completion of recrystallization which is shown in Figure 2.1. The recrystallization stop temperature (T_R) temperature can be affected by the alloying elements as shown in Figure 2.3^[27]. Nb and Ti are the most effective elements to raise the T_R temperature due to the retardation of the recrystallization. Solute Ti and Nb can have a

solute drag effect at higher temperature. Meantime, oversaturated solutes can precipitate as carbides or nitrides by strain-induced precipitation to bring about the non-recrystallization region and retard the recrystallization^[28, 29]. The modification of T_R temperature can provide different temperature range to conduct hot rolling for different purposes.

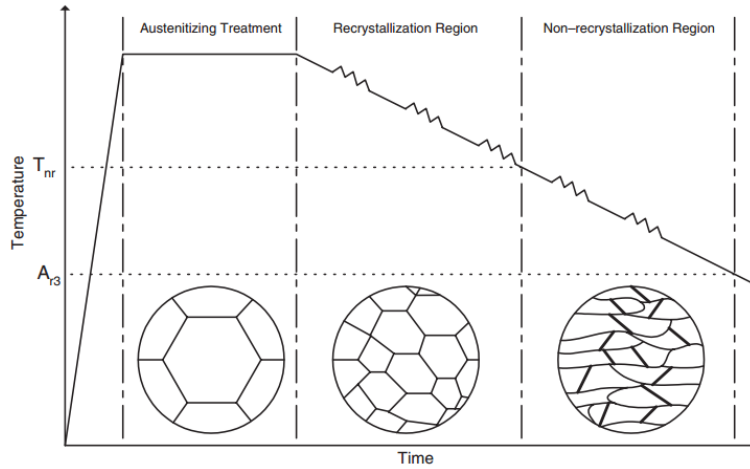


Figure 2.1: Schematic of TMCP and microstructures evolution

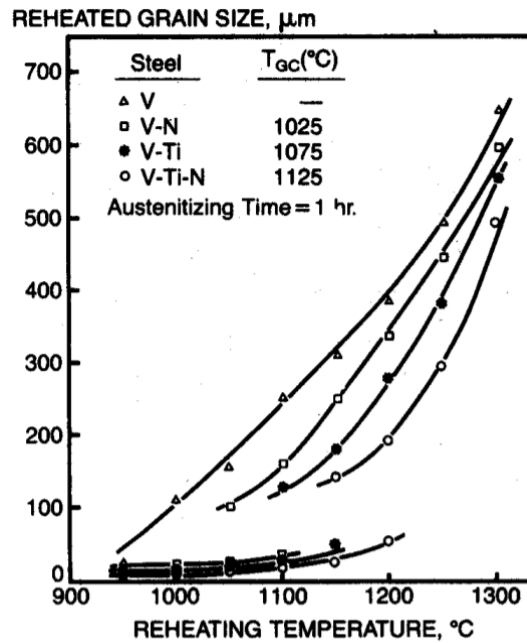


Figure 2.2: Grain coarsening behavior of V and V-Ti steels during reheating

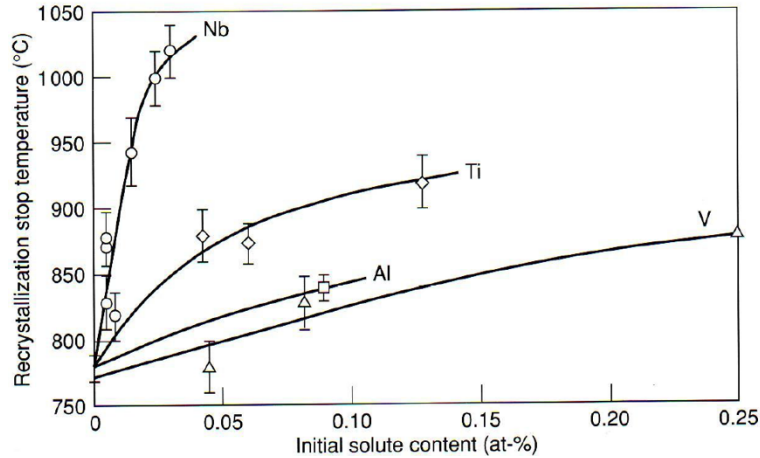


Figure 2.3: Effect of various of microalloying elements on the recrystallization stop temperature of austenite in a low carbon 1.4wt% Mn steel

In general, rolling under the T_R temperature comes with an increase in the strength, it is because the low finishing temperature will intensify the carbonitrides precipitation since the heavy reduction increases the number of nuclei. But sometimes, a loss in the strength can be found which is related to the larger size of precipitates formed during hot deformation and those precipitates do not contribute to the ferrite strengthening. Consequently, less microalloying elements were left in the solid solution to form fine strengthening precipitates in the ferrite. Figure 2.4 shows the 50% shear FATT and grain diameter change with the finish rolling temperature and reheating temperature^[19]. Lowering the reheating temperature and finish rolling temperature can decrease the grain size and increase the toughness as a result.

Hot deformation under T_R temperature can result in an increase in the interfacial area because of the elongated austenite grains and the introduction of deformation bands within the grains. As the phase transformation continues, those defects will become suitable nucleation sites for the ferrite to form. The grain refinement is achieved by maximization of nucleation rate and minimization of the growth rate. It is necessary to maximize the austenite grain boundary per unit

volume (S_v) at the onset of the phase transformation [30, 31]. Moreover, as the extent of the hot deformation increases, the nucleation sites at the austenite grains boundaries and within the grains also increase. Figure 2.5 shows the relationship between the austenite interface area per unit volume and the ferrite grain size [30]. It can be seen that as the ferrite grain size decreases as the S_v increases, and also, the transformation from deformed austenite produces much fine ferrite grains than that from recrystallization austenite. However, some researchers pointed out that for a fine grained austenite structure (less than $20\mu\text{m}$), whether or not it is deformed or recrystallized, the S_v does not affect the ferrite grain size too much [21, 30, 32].

As for the rolling reduction, it can also influence the transformation. From Figure 2.6 [33], it can be seen that for deformation below the recrystallization stop temperature, the transformation start temperature seems independent of the rolling temperature, while the reduction rate shows a big impact on it [34-37]. The transformation temperature increase as more hot reduction was applied which signifies the transition from non-polygonal ferrite to polygonal ferrite.

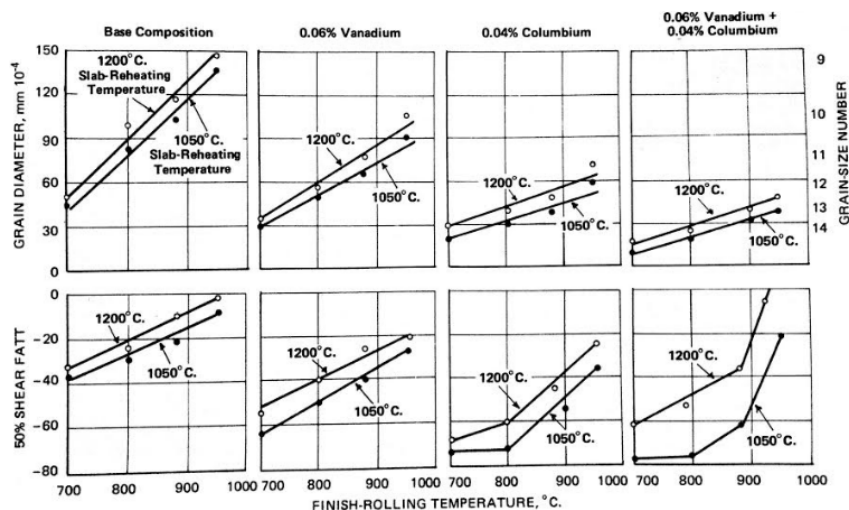


Figure 2.4: Dependence of grain size and 50% shear FATT on the finish rolling temperature of pearlite-reduced steels alloyed with vanadium and columbium

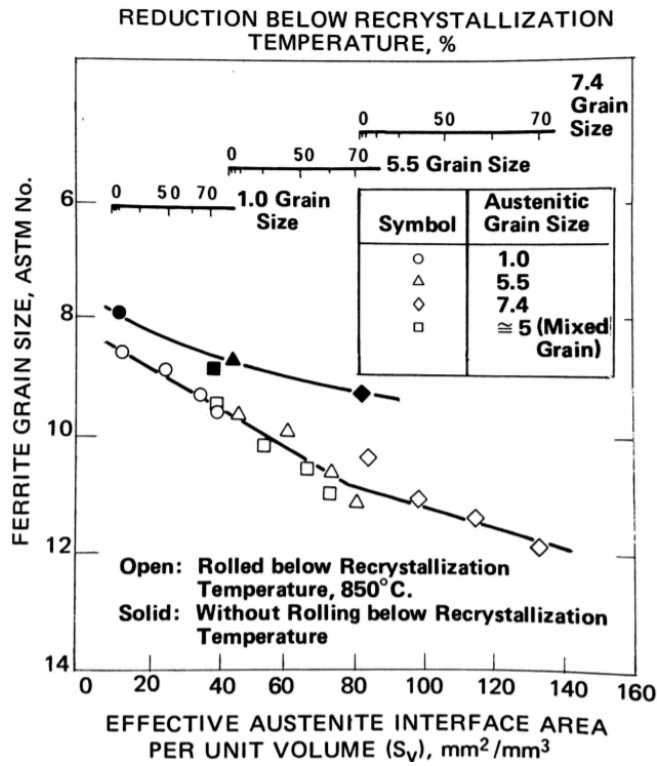


Figure 2.5: Variation of ferrite grain size with effective austenite interface area per unit volume

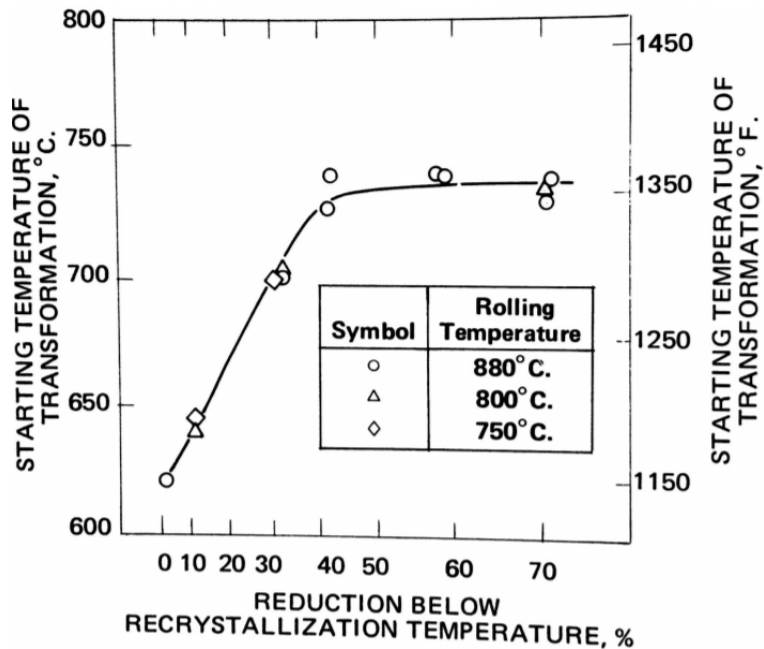


Figure 2.6: Variation of austenite to ferrite transformation temperature with deformation below recrystallization temperature

2.1.2 Cooling rate

Once the fine austenite grains have been obtained during hot deformation, it is important to preserve them before getting to the coiling temperature and transforming them to the finest ferrite grain structure. And one way is to increase the transformation ratio $d\gamma/d\alpha$. The transformation ratio is the ratio of the true austenite grain size to the grain size of the resulting ferrite, and for a given S_v , the ratio can be increased (ferrite grain size decreased) through increasing the cooling rate after hot rolling. As Figure 2.7 shows, for given microalloying element and same austenite grain size, a higher cooling rate can have a smaller ferrite size^[26].

Besides that, a high cooling rate can enhance the precipitation strengthening effect by lowering the interphase precipitation temperature which decreases the precipitates size and spacing. Figure 2.8 shows the effect of cooling rate on the ferrite grain size, yield strength and toughness^[21]. It can be seen that the cooling rate has significant influence on the microstructure and mechanical properties. From continuous cooling studies, it is known that the cooling rate can affect the phase transformation temperature, because at faster cooling rate, the extent of undercooling will give extra driving force to the steel which allows it to transform at lower temperatures.

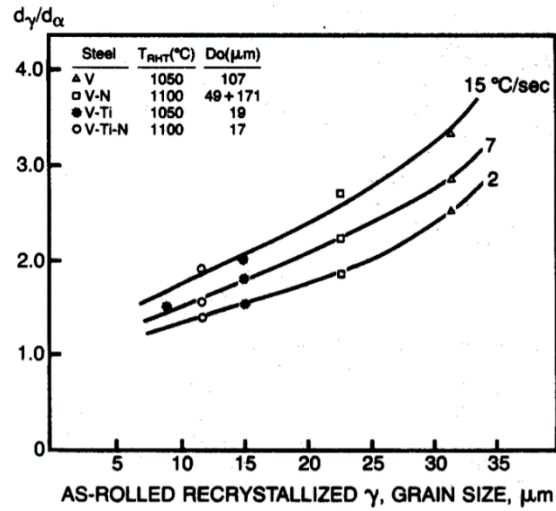


Figure 2.7: Dependence of grain refinement ratio on austenite grain size and cooling rate

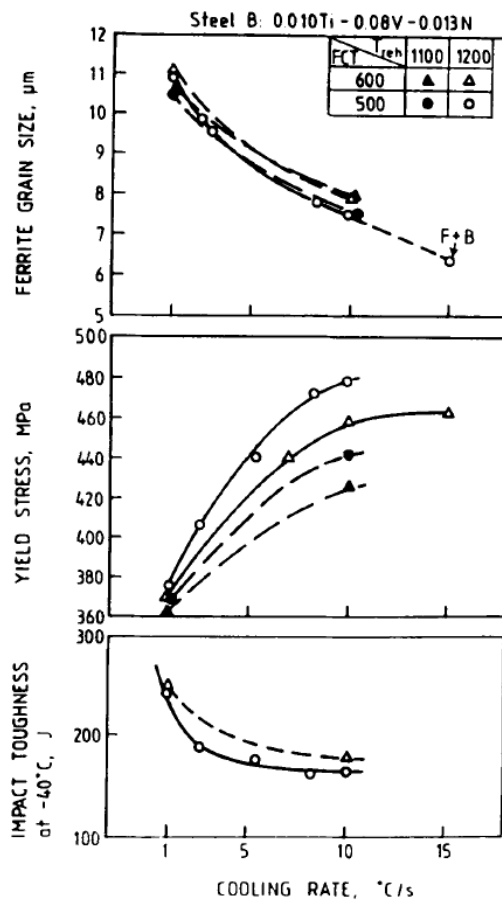


Figure 2.8: Effect of cooling rate from FRT of 1030 ~ to FCT on the ferrite grain size, yield stress, and toughness

2.1.3 Finish cooling temperature

After hot rolling, the steel is usually cooled down by accelerated cooling process to a predetermined temperature below the ferrite transformation temperature. The finish cooling temperature is also called coiling temperature. From Figure 2.9^[21], it can be seen that the ferrite grain size decrease as the finish cooling temperature decreases, however the grain size does not change much in the low temperature range of 600°C to 400°C, while the microstructure changes to ferrite/bainite instead of ferrite/pearlite. Whereas, the yield strength depends strongly on the finish cooling temperature, the strength increase remarkably with the decreasing of the finish cooling temperature until the appearance of bainite. Interestingly, the yield strength of low Ti/N steels drops after the formation of bainite. It can be explained that overcooling of bainite can reduce the potential of precipitation strengthening during the slow cooling from the coiling temperature. For steels with different coiling temperatures, the cementite morphology could change.

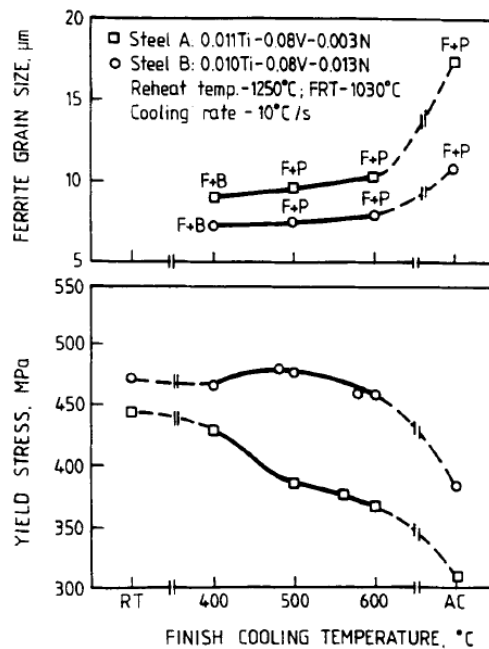


Figure 2.9: Effect of finish rolling temperature on the ferrite grain size and yield strength

Figure 2.10 shows the effect of coiling temperature on the morphology of the cementite^[38]. The pearlite constituent changes from a banded structure to dispersed colonies as the coiling temperature decreases. As the coiling temperature keeps decreasing, instead of pearlite, cementite shows up and appears as a spheroidized particles on the grain boundaries at 560°C, and randomly distributed in the matrix at 500°C, and the toughness is lowered by the low coiling temperature, in spite of the absence of pearlite.

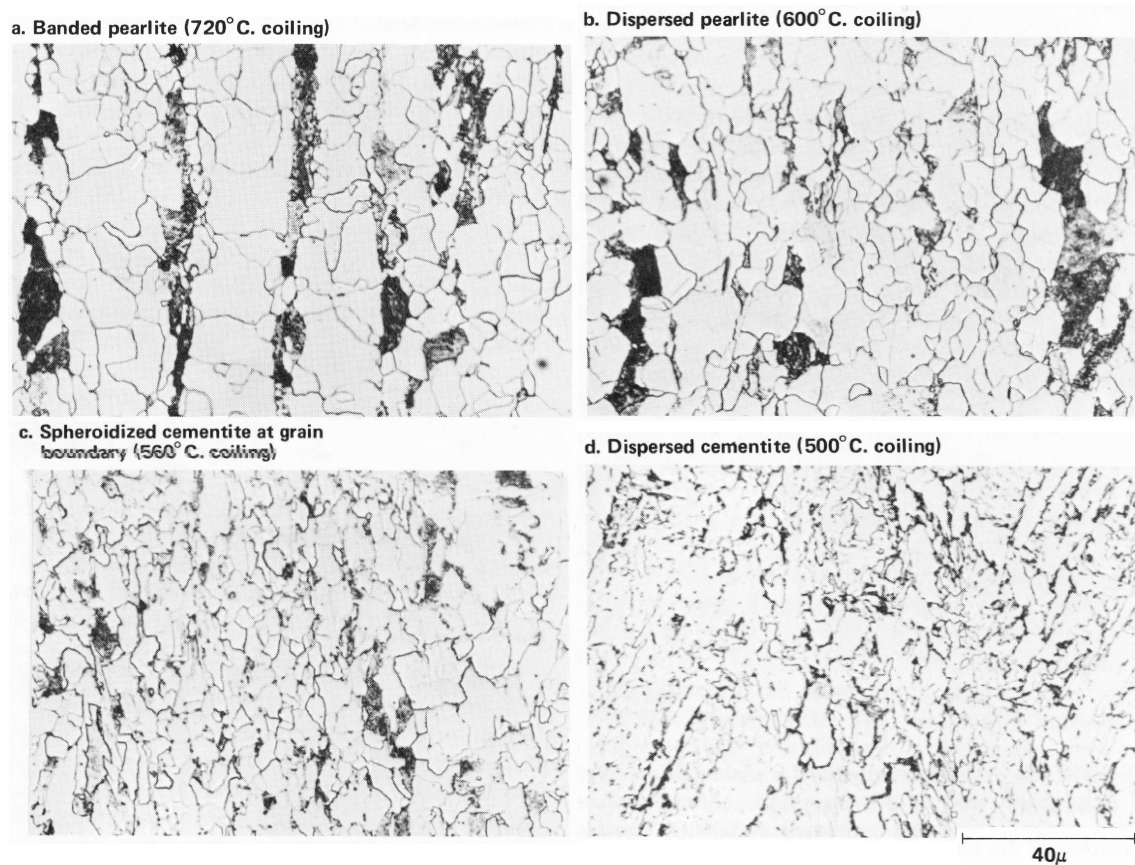


Figure 2.10: The effect of coiling temperature on the morphology of cementite

2.2 BAINITIC TRANSFORMATION

Since their superior balanced properties of strength, toughness and economy, bainitic steels have wide applications including steam turbine, pressure vessels, plates and bars for high strength steel structures [39].

Bainite was first described by Davenport and Bain [40] in 1930 in the isothermal transformation study to decompose the austenite at temperatures between 150°C and 550°C as “acicular, dark etching aggregate” which was unlike either pearlite or martensite observed in the same steel, and was named martensite-troostite at that time. The isothermal bainite is usually distinguished as “upper” or “lower” bainite depending on whether the carbides are distributed between each ferrite regions or within them [41-43].

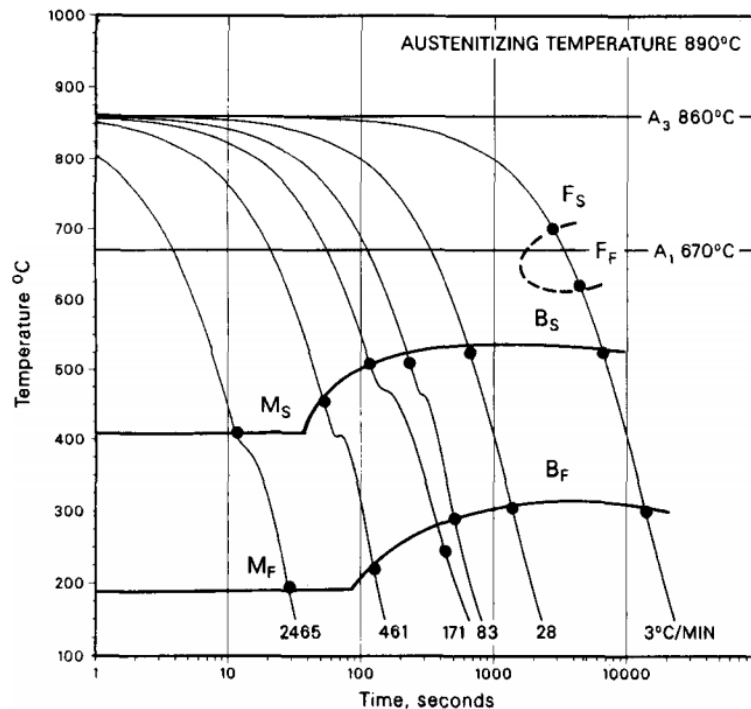


Figure 2.11: Continuous cooling transformation diagram for a Ni-Cr-Mo steel

However, from industrial perspective, the bainite transformation during continuous cooling can draw more attention. It can be seen from the continuous cooling transformation (CCT) diagram in Figure 2.11^[39], the polygonal ferrite transformation region shifts to the right side and leaves a broad, flat bainite transformation region which can cover over a wide range of cooling rates (from 4°C/min to 600°C/min), and that makes it possible to manufacture a heavy section with a similar mechanical properties as the thinner sections.

The bainite transformation can occur during a wide range of cooling rates, but the situation is very complicated because of the morphology of the microstructure presented is rather variant. The microstructure of bainite can be a result from the growth of accicular ferrite associated with a second phase constituent which could be martensite, carbide or austenite, depending on the nature of austenite, diffusion of carbon and other alloying elements.

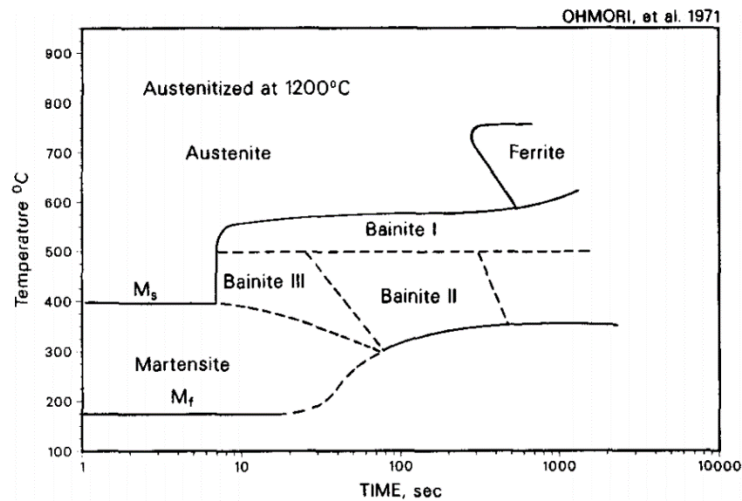


Figure 2.12: Schematic CCT diagram of a Ni-Cr-Mo steel showing three forms of bainite

Early efforts made by Ohmori et al. ^[44] is shown in Figure 2.12. Using both replicas and thin foils, after checking the morphologies and crystallographic details, the microstructures were separated into three classifications. The Bainite I is a carbide free acicular ferrite with well defined films of retained austenite (and/or martensite) at the lath boundaries, Bainite II is similar to upper

bainite, with cementite decorating between ferrite laths. Bainite III is similar to lower bainite, with cementite forming within ferrite laths. Each kind of bainte will have its own distinctive characteristics and formation mechnism which will be disscussed in detail in the following part.

2.2.1 Transformation Mechanism

The phase transformation of bainite is just like other phase changes, including an incubation period, followed by nucleation and growth. During the continuous cooling transformation, the bainite can be formed in a certain range of temperatures and cooling rates. According to some researchers [43, 45-47], the transformation of the bainite includes a diffusionless shear transformation of first formed ferrite and partitioning or re-distribution of carbon.

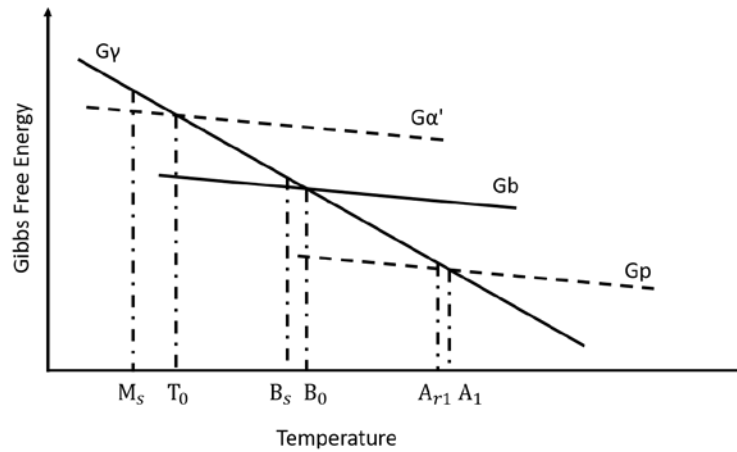


Figure 2.13: Gibbs free energy of different phases

Figure 2.13 shows the free energy change vs. temperautre in austenite, martensite, bainite and pearlite. The B₀ is the temperature where bainite and austenite have the same free energy, the energy change during the phase transformation can be descrtibed in the followig equation:

$$\Delta G = V \cdot \Delta g_v + S\sigma + \varepsilon V \quad (2.1)$$

where ΔG is the change of Gibbs free energy in the whole system, V is the volume of the new phase, Δg_v is the energy difference between the parent and the new phase, S is the new interfacial area, σ is the surface energy per area and ε is the volume strain energy. The last two terms on the right side of the equation are the drag force with positive values, so as long as $|V \cdot \Delta g_v| > S\sigma + \varepsilon V$, and keeps a negative value which gives a negative value of ΔG , it is possible to nucleate. At temperature of B_0 , Δg_v equals to 0, in order to have a negative value of Δg_v , the transformation temperature need to be lowered to B_s .

Numerous researches have been done to predict the bainite transformation start temperature (B_s). Steven and Haynes^[48] developed an empirical equation (Eq. 2.2) to calculate B_s based on the alloying compositions of the material. And Kunitake and Okada^[49] proposed another B_s equation (Eq. 2.3) by pointing out the influence of Ni and Cr. However, this one seems to overestimate the coefficient of Si. Both of these equations probably are based on the steels with less than 1.0 wt% of Si. Kirkaldy and Venugopalan^[50] made a modification to Steven and Haynes' equation for the prediction of B_s of both low and high alloy steels (Eq. 2.4).

$$B_s (\text{°C}) = 830 - 270C - 90Mn - 37Ni - 70Cr - 83Mo \quad (2.2)$$

$$B_s (\text{°C}) = 732 - 202C + 216Si - 85Mn - 37Ni - 47Cr - 39Mo \quad (2.3)$$

$$B_s (\text{°C}) = 656 - 57.7C - 75Si - 35Mn - 15.3Ni - 34Cr - 41.2Mo \text{ (in weight percent)} \quad (2.4)$$

Although all the equations above were established based on the data from the isothermal transformation, and other researchers also published different equations to predict the B_s temperature, these equations may still be used to approximate the B_s during continuous cooling. The bainite transformation finish (B_f) temperature is the temperature where 100% of bainite can form. When the B_f temperature is lower than martensite transformation start (M_s) temperature,

instead of forming a fully bainitic structure, part of retained austenite will transform into martensite.

Before the transformation starts, the non-uniformly distributed carbon atoms in the undercooled austenite result in carbon rich and lean regions. Inside the carbon lean regions, the ferrite will nucleate when the size of the nucleus is larger than the critical size at that temperature, ferrite will keep growing. Because of the temperature of austenite is too low to allow the iron atoms to diffuse, so the growth of the ferrite is by a shear mode, followed by subsequent diffusion of carbon, with the possibility of carbides precipitation.

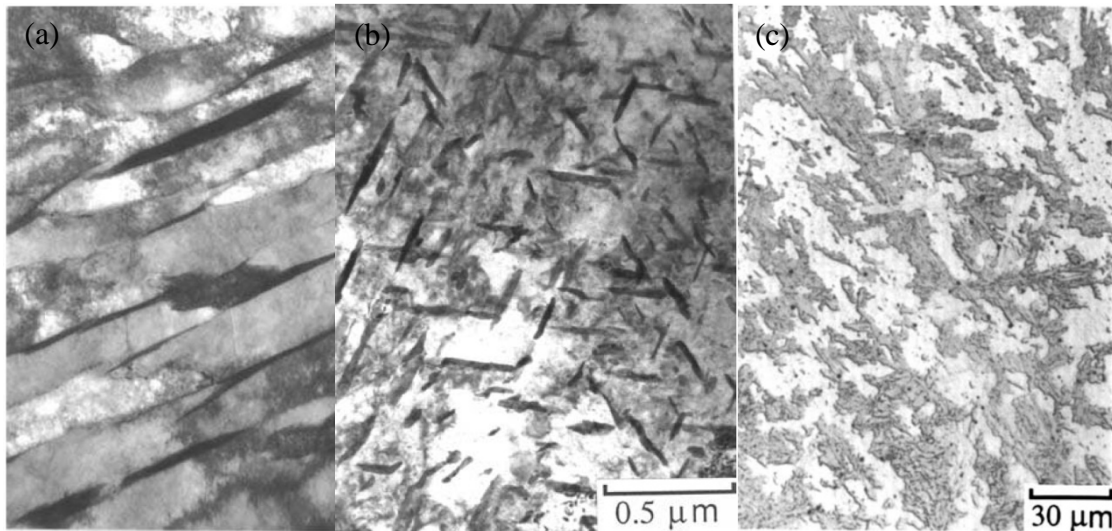


Figure 2.14: (a)TEM of upper bainite of Si-Mn-Cr steel isothermally transformed at 400°C; (b)Microstructure of lower bainite; (c) Light micrograph of granular bainite in a Cr-Mo steel

The ferrite will nucleate first at the austenite grain boundaries or carbon lean regions near them, and grow inward into the grains. In the meantime, the carbon atoms in the advancing interface and inside the supersaturated ferrite will keep diffusing to both sides of the ferrite lath, given that the diffusion coefficient of carbon in ferrite is higher than in austenite, when the carbon concentration at the phase boundary reaches the local solubility limit, cementite will form. The

precipitation of carbides is peripheral to the new formed ferrite, and reduces the carbon concentration in the residual austenite, which can even accelerate the formation of ferrite and form upper bainite (Figure 2.14 (a)^[51]) in the end. The upper bainite transformation temperature range is just below the pearlite transformation region, typically below 500°C^[52].

For the lower bainite (Figure 2.14 (b)^[53]), when the transformation temperature is lower, non-lamellar aggregated ferrite will form from the austenite grain boundaries or carbon lean regions inside the grains in a shear mode, and is often characterized as acicular. The carbon atoms don't have enough energy to diffuse to the phase boundaries, and will probably precipitate on some sub-grain boundaries or crystal planes, or even be trapped by dislocations inside the grains.

Granular bainite (Figure 2.14 (c)^[54]) was described as coarse plates decorated by particles with an almost entirely granular aspect, together with islands of martensite and retained austenite. It was first found by Habraken and coworkers^[55-57] back in the 1950s in some low and mild carbon alloying steels. This kind of microstructure is supposed to occur only during continuous cooling^[45]. In modern times, numerous researches have reported finding of granular bainite in both the bulk steel^[58] and in the HAZ during welding^[59, 60].

The transformation mechanism is similar to other types of bainite, during continuous cooling, carbon atoms diffuse from the carbon lean region where the ferrite will nucleate to the residual austenite nearby, which causes carbon diffusion within the austenite region because of the concentration gradient of carbon sloping from a high chemical potential near the interphase boundary to a lower one near the grain centers. When this diffusion inside the austenite is completed, the carbon concentration gradient at the phase boundary is less than that in the equilibrium condition. In order to maintain that balance, the ferrite continues to keep growing. When the residual austenite was surrounded by the ferrite grains, during final cooling, those region

will transform into retained austenite or martensite or the so-called martensite/austenite (M/A) constituent^[61]. Depending on the transformation temperature, these M/A islands and morphologies of ferrite will have different appearances^[62].

Previously mentioned bainite types are the most commonly ones observed in many high strength steels^[45]. Besides that, there are still other types of bainite, i.e. inverse bainite, columnar bainite, pearlitic bainite, grain boundary and lower bainite which are shown in Figure 2.15^[45, 63, 64], but these will not be discussed here in detail.

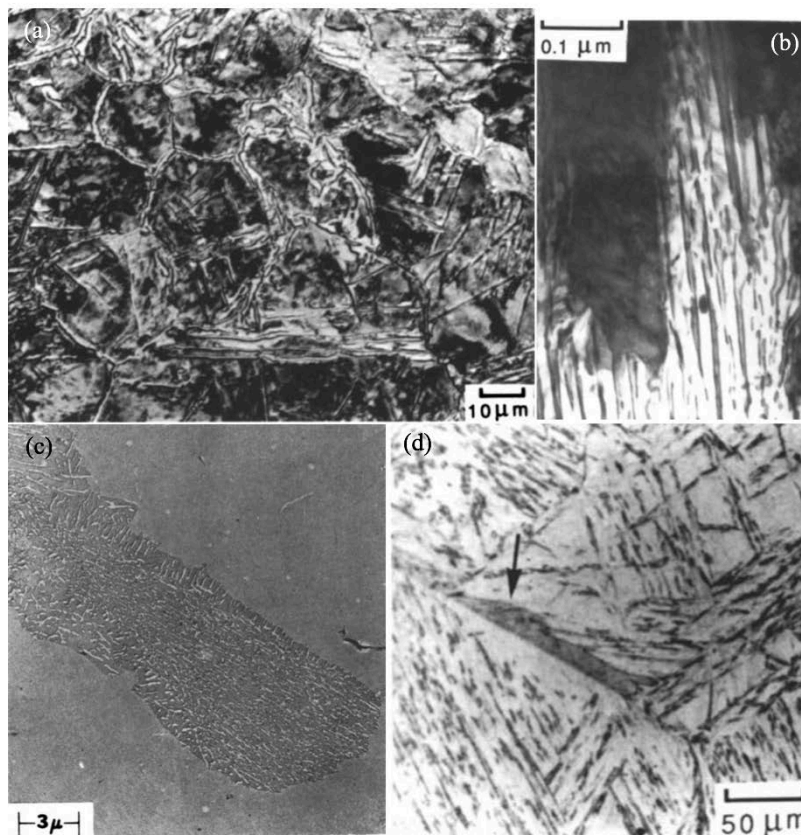


Figure 2.15: Microstructure of (a) Inverse bainite; (b) Pearlite bainite; (c) Columnar bainite and (d) Grain boundary lower bainite

2.2.2 The Influential Factors on the Bainite Transformation

In most low alloy steels, it is impossible to have a complete bainite transformation, because the bainite transformation region probably is partially overlapping with both the pearlite transformation region and the martensite formation region. That is, the M_s temperature could lay in the middle of the bainite transformation region, and if it does, then the martensite might form first before the completion of the bainite transformation. The reason for these possibilities is related to the chemical composition, austenitization temperature, transformation temperature, etc. In this section, a discussion will be made of some of the main factors that will influence the bainite transformation.

From equations 2.2-2.4, it already shows that the bainite transformation start temperature is highly affected by the chemical compositions, and, in addition, the transformation rate is also influenced by the chemical composition. Alloy alloying elements such as C, Ni and Mn (Figure 2.16 (a)) can increase the stability of supercooled austenite, thereby reducing the gap of free energy between bainite and austenite. This will retard the nucleation and growth rates, thus slowing down the transformation and shifting the transformation curve to the right. Moreover, during the bainite transformation, there is no diffusion for the substitutional alloying elements and only the carbon atoms can diffuse. Other elements such as Cr, Mo, V, and W (Figure 2.16 (b)) can easily form carbides to slow or stop the carbon from diffusing, and becoming barriers to the movement of the phase boundary. However, elements such as Al, Co, on the other hand, will accelerate the formation of bainite because those elements cannot form carbides and also decrease the stability of austenite as they are ferrite stabilizers.

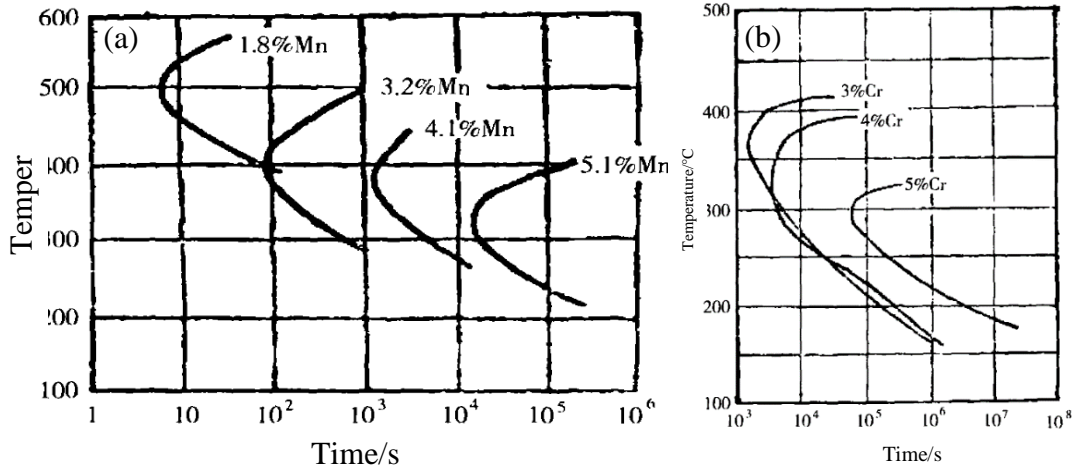


Figure 2.16: (a) Mn and (b) Cr influence on the transformation of bainite

Finer prior austenite grains will shift the transformation curve to the left side, because the finer structure would provide more nucleation sites for the bainite. This was confirmed by Barford and Owen [65] in their work showing that the rate of bainite transformation is increased by a decrease in the prior austenite grain size (PAGS). The coarser the austenite grains, the longer it takes to go through the incubation period and form certain amount of bainite. According to Lee et al [66], they found that the smaller the PAGS, the faster the average transformation rates of both upper and lower bainite, which shows a good agreement with previous results (Figure 2.17(a)).

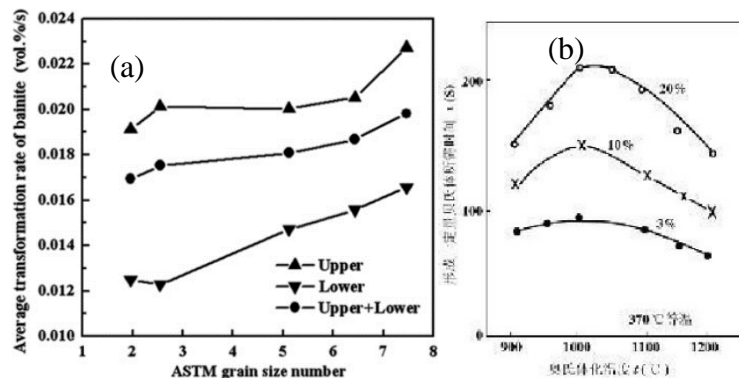


Figure 2.17: (a) Influence of PAGS and austenitization temperature on the transformation of bainite; (b) Influence of the austenitization temperature on the bainite transformation

Figure 2.17 (b) shows the influence of the austenitization temperature on the bainite transformation of 1.2 wt% C, 1.49 wt% Mn steel. It can be seen that to form a certain amount of bainite, with increasing austenitization temperature, the time first increases to a peak then falls. Because with higher austenitization temperature, more carbides will dissolve in the parent austenite, and with more carbon atoms diffusing will increase the rate of transformation. However, by increasing the temperature, the PAGS will coarsen, thereby lowering the carbon gradient in the austenite and retarding the transformation rate. Thus, the higher the austenitization temperature is, the sooner the peak value will appear.

Another factor is the transformation temperature, which according to Vesudevan et al ^[67], the relationship between the growth rate and transformation temperature is shown in the following equation:

$$\frac{dl}{dt} = B \cdot e^{-\frac{Q_L}{RT}} \quad (2.5)$$

where B is a constant which varies with the chemical composition, and R is the gas constant, T is the absolute temperature, Q_L is the activation energy of bainite growth which varies with the carbon concentration. As it shows, when the transformation temperature drops, the term $e^{-\frac{Q_L}{RT}}$ is smaller, and the growth rate decreases. And under the same transformation temperature, the higher the carbon concentration, the larger the Q_L and the slower the growth rate.

According to Freiwillig et al. ^[68], the plastic deformation can also have a large influence on the transformation of bainite, especially the deformation temperature of the austenite. With a higher deformation temperature, the deformed austenite will prolong the incubation period and slow down the transformation. At an intermediate deformation temperature range, not only will the bainitic ferrite get finer, but also more carbides will precipitate, which can improve the hardness and strength of the bainite without sacrificing the ductility and toughness. Once the deformation

occurs at a lower temperature, the incubation time will be shortened and transformation will get faster.

In addition to these, the cooling rate also plays an important role in the bainite transformation as shown in Figure 2.18^[69, 70]. The B_s is decreasing with increasing cooling rate. As shown in 2.19^[71], with a faster cooling rate, the time for the carbon to diffuse is limited, so carbon accumulated at the interphase between austenite and ferrite will create a steep gradient in the carbon concentration. This means that the carbide precipitation could occur in the vicinity of the interface. At lower cooling rate, however, the carbon concentration gradient extends over a greater distance into the austenite and remains at a low level. So the precipitation of carbides is not as likely. As a result, the B_s temperature decreases with the increasing cooling rate, and the lower B_s temperature will increase the driving force to permit the transformation.

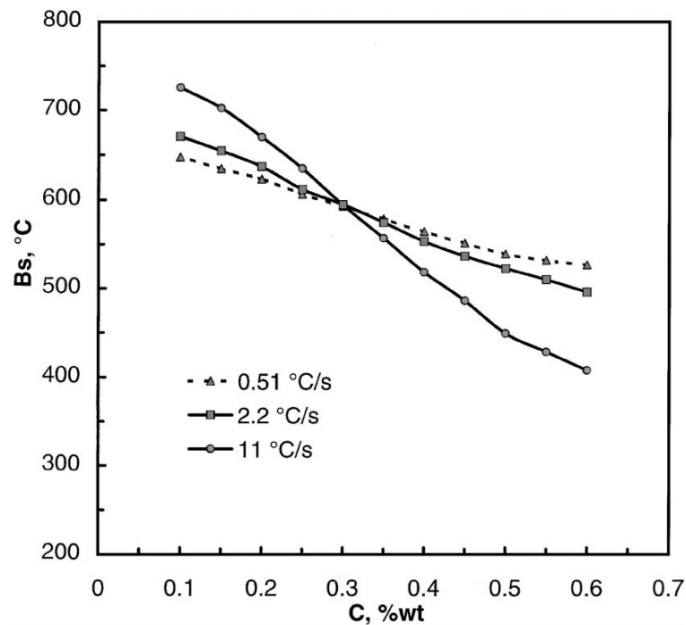


Figure 2.18: Influence of cooling rate on the transformation of bainite

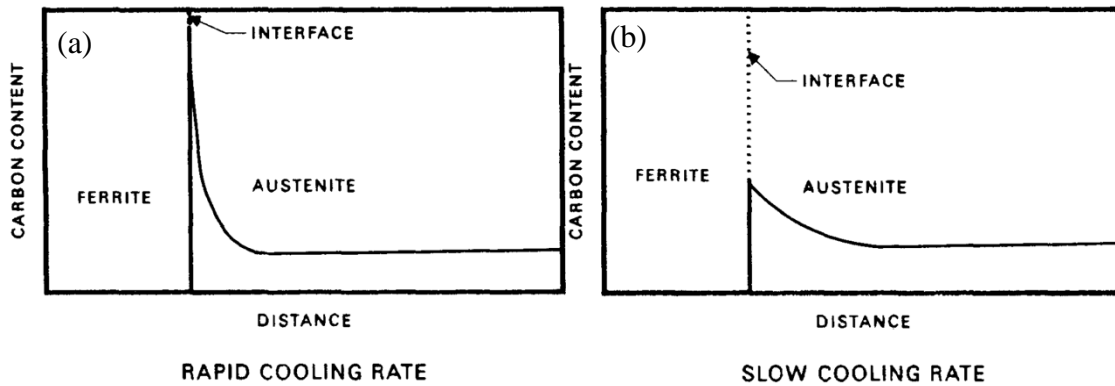


Figure 2.19: Schematic showing carbon concentration gradient at the interface of ferrite and austenite during (a) rapid cooling and (b) slow cooling

2.3 FORMATION OF MARTENSITE/AUSTENITE CONSTITUENT

During continuous cooling, most of the bainitic microstructures investigated in low carbon microalloyed steels were comprised of bainitic ferrite and/or granular bainite. A carbon-rich hard second phase originated from residual austenite and was located on the bainitic ferrite subunits. These will then fully transform to martensite and/or pearlite during cooling or remain as partially transformed retained austenite at ambient temperature, which is called martensite/austenite (M/A) constituent. These M/A islands are known to have an important effect on the mechanical properties of the steels. While work hardening and the tensile strength could be improved by MA, the toughness and HIC resistance will be deteriorated. Their amount, morphology and distribution all affect the materials in multiple ways ^[72-74].

2.3.1 The Formation Mechanism of M/A Constituent

In the bainite transformation process, there is no significant diffusion of the iron or other substitutional atoms, the formation of M/A constituents is mainly controlled by the diffusion of carbon atoms and the nucleation and growth of cementite. And the formation of M/A constituents is often a consequence of the transformation of granular bainite. During the diffusionless transformation of granular bainite, subunits form repeatedly and inherit the chemical composition from the austenite, the excess carbon will be rejected into the residual austenite, as the transformation proceeds, the carbon concentration in the austenite will keep rising. During the final cooling, when the carbon-rich phase is cooled to a temperature which is below the M_s temperature, it will partially transform to martensite and the rest will be retained as austenite, therefore forming M/A constituents.

2.3.2 The Influence Factors on the Formation of M/A Constituents

One of the most important factors to influence the formation of M/A constituents is the alloying elements. The amount of M/A in high carbon or mild carbon steels is higher than in the low carbon steels, and from Figure 2.20(a) ^[75], it can be seen that the amount of granular bainite is increasing with the carbon concentration. That is because with higher carbon within the steel, during the transformation, when newly formed ferrite will eject carbon into the residual austenite, the high carbon steel seems more likely to have more carbon enriched regions than the low carbon steel and form M/A afterwards. Other carbide elements like Mn, Cr and Mo can also increase the formation of M/A which can be seen from Figure 2.20(b) ^[61]. That is because those elements could decrease

the Bs temperature, increase the phase transformation rate, and with low diffusion rate of carbon, the size of M/A constituents will be decreased.

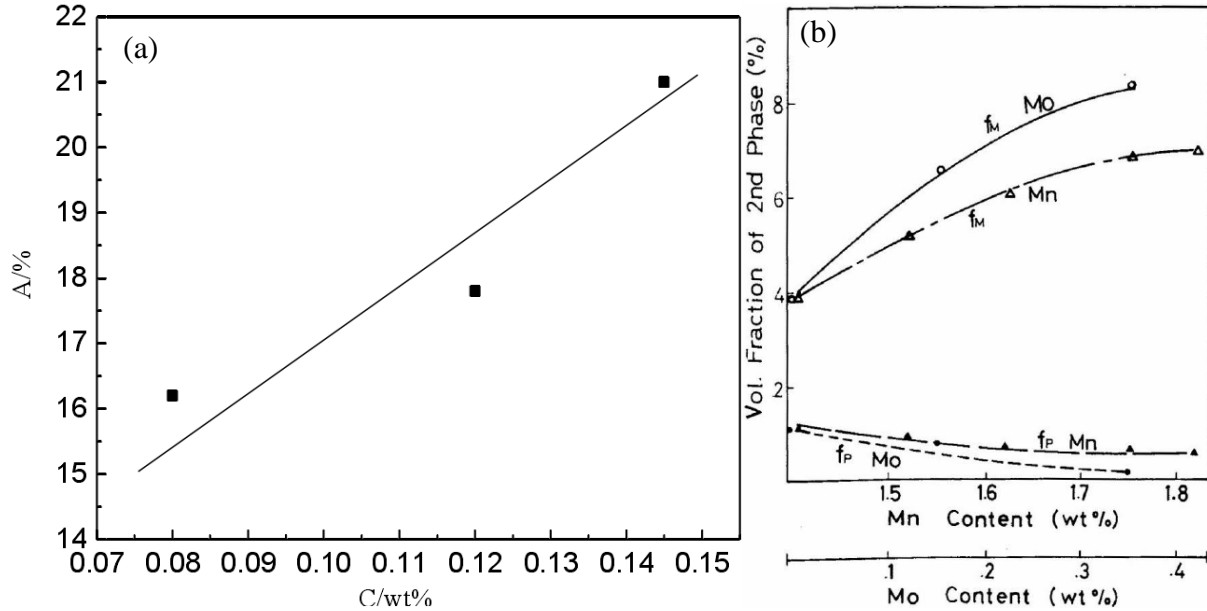


Figure 2.20: (a) Influence of carbon on the formation of M/A; (b) Influence of Mo and Mn on the formation of M/A

Another factor is the cooling rate, from Figure 2.19, it can be seen that during continuous cooling, there will be a carbon concentration region near the interface between the ferrite and parent austenite. When the transformation temperature is high, the cooling rate is low, the diffusion rate of carbon is high, and there is enough time for the carbon near the interface to diffuse into the austenite, so it is difficult for the carbon to accumulate on the interface. However, when the transformation temperature is low, but the cooling rate is high, neither the diffusion rate nor the time is enough for the carbon to diffuse, so there will be a thin carbon rich film built on the interface where cementite will precipitate. At intermediate transformation temperatures and cooling rates, a carbon rich region will form, and the carbon concentration is not high enough to precipitate the cementite but still enough to stabilize the austenite and form M/A.

And the cooling rate can also change the morphology of the M/A islands. As shown in Figure 2.21, with lower cooling rates (Figure 2.21(b)), the size of M/A constituents get bigger compared to the M/A under higher cooling rate (Figure 2.21(a)). This is due to the increase in the Bs which decreases the transformation rate, allowing the carbon to diffuse more easily to a long distance and the carbon enriched region inside the austenite to become larger.

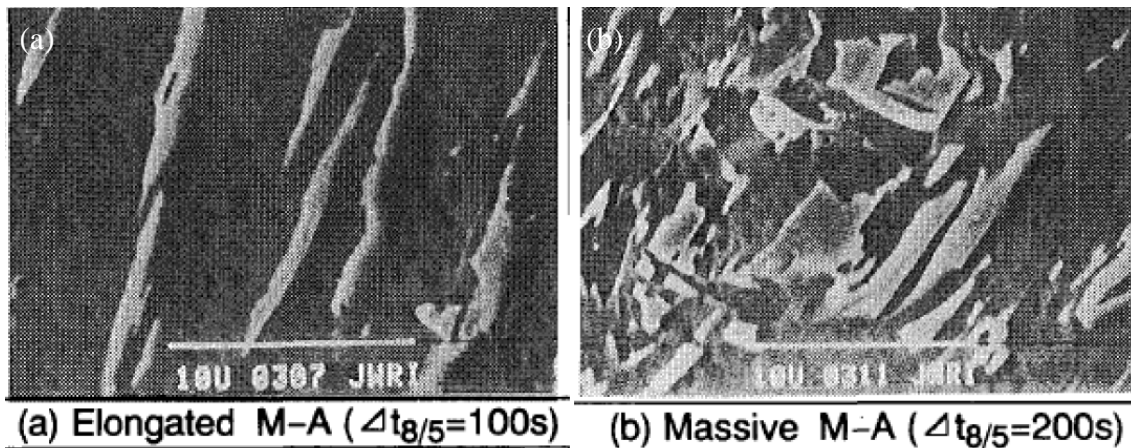


Figure 2.21: Morphologies of M/A constituents under different cooling rate

From aforementioned granular bainite transformation, the morphologies are highly dependent on the transformation temperature. From Figure 2.22, it can be seen that there are three temperature transformation regions (high, intermediate and low), each region will result in different product of bainite or M/A [62]. During the incubation period, there is carbon rich and lean regions inside the austenite phase, and the ferrite will nucleate from those lean carbon regions and grow by a diffusionless mechanism, while the carbon will diffuse into the residual austenite region from the interface. In order to keep the balance at the interface, the ferrite has to keep growing. In the high temperature region, the carbon that is rejected from the ferrite plates can diffuse in either the longitudinal or transverse directions, the carbon can easily escape from the narrow austenite regions in the middle of the ferrite plates, so there is no clear boundary between the ferrite plates.

Therefore, what is observed is that the M/A islands are distributed randomly over the bainitic ferrite. In the intermediate temperature region, because of the diffusion rate of carbon between the longitudinal and transverse direction is different, so the ferrite and M/A islands show a clear orientation dependence. In the low temperature range, the carbon atoms cannot escape from the region between the ferrite plates, and this high carbon austenite will be surrounded by the ferrite plates in the end. Therefore, all the ferrite and M/A constituents will be elongated in the high diffusivity direction.

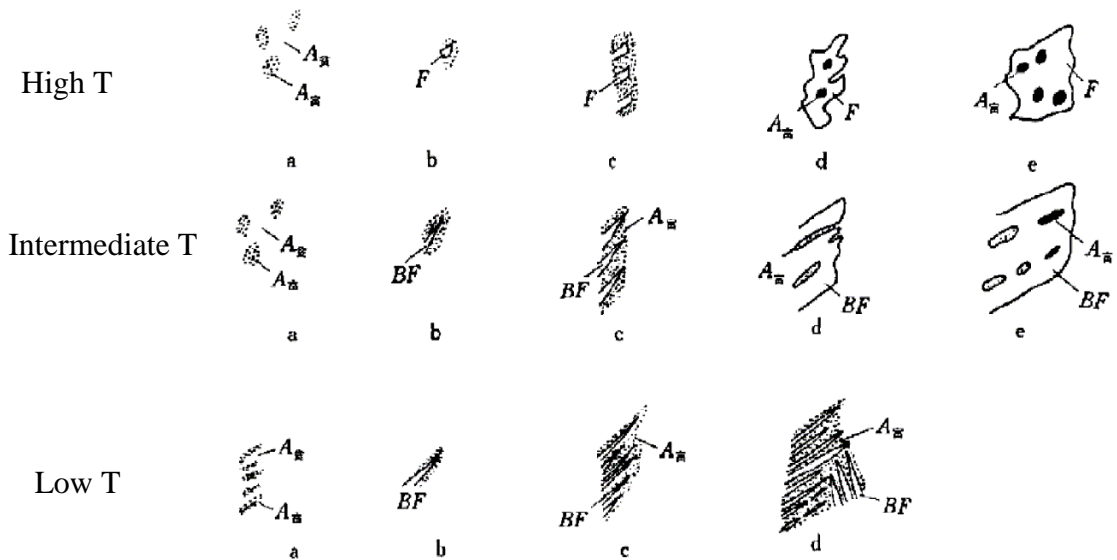


Figure 2.22: Schematic diagram of granular bainite resulted from ferrite

2.4 STRENGTHENING MECHANISM

The favorable combination of strength and ductility mainly comes from the imperfection that steels contain which are due to the presence of crystalline discontinuities or defects such as solute atoms, such as precipitates, grain boundaries, and dislocations. These imperfections will create strains and distortions that tend to impede the movement of dislocations, thus increase the strength

and decrease the ductility. A stringent control of entire thermomechanical processing including reheating, rolling and cooling which combines the controlled rolling and accelerated cooling with extra alloying additives can strengthen the high strength low alloy (HSLA) steels in multiple ways. The strengthening mechanism involved in the accelerated cooling is primarily a transformation strengthening due to the complex phase mixture of ferrite, bainite or martensite, introducing higher dislocation density. A grain refinement and precipitation hardening is a result of proper rolling strategy and subsequent controlled cooling or aging process afterwards. Several strengthening mechanisms will be discussed in this section.

2.4.1 Grain boundary strengthening

Grain boundary strengthening is one of the most efficient ways to improve the mechanical properties of a material, both the strength and toughness. This is especially true for steels. The yield strength of a polycrystalline material can be expressed by the Hall-Petch equation, as follows^[76-78]:

$$\sigma_y = \sigma_i + k_y d^{-\frac{1}{2}} \quad (2.6)$$

where σ_y = yield strength

σ_i = friction stress which opposes dislocation movement

k_y = a constant (often called the dislocation locking term)

d = ferrite grain size

Sometimes, σ_i can be separated into two terms, σ_{ST} and σ_T as demonstrated by Conrad^[79]. σ_{ST} is the structure sensitive term where dislocations can interact with dislocations, precipitates and solute atoms; and σ_T is a temperature sensitive term which is related to Peierls

stress. The Hall-Petch equation was found also to apply to other kinds of boundaries such as ferrite-cementite in pearlite, mechanical twins and martensite plates^[80].

The model for this equation was based on the theory that grain boundaries can act as barriers to the dislocation motion. The dislocation source within a grain can cause a pile-up of dislocations at the grain boundaries, and the stress at the tip of the pile-up of dislocations must exceed a critical shear stress τ_c in order for slip to pass through the grain boundaries.

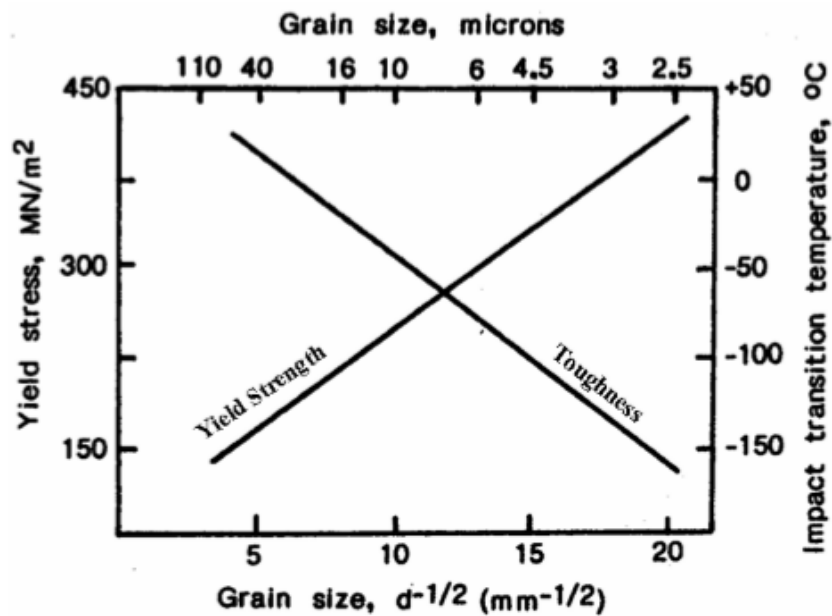


Figure 2.23: Effect of ferrite grain size on yield strength and impact toughness

Usually, an increase in the strength can lead to a decrease in the toughness, however, it has been known for decades that that the refinement of the ferrite grains will also produce an improvement in the toughness^[81]. This effect is shown in Figure 2.23. The equation linking toughness to the grain size is also given below:

$$\beta T = \ln \beta - \ln C - \ln d^{-\frac{1}{2}} \quad (2.7)$$

where β and C are constants, and T is the ductile to brittle transition temperature, d is the ferrite grain size. Thus, as mentioned before, as the ferrite grain size decrease, the DBTT decreases which means the toughness improves.

There are multiple ways to achieve grain size refinement. In the thermomechanical processing, the addition of elements such as titanium, aluminum, vanadium or niobium can form carbides or nitrides at elevated temperatures, acting to pin the movement of the grain boundaries. In addition, low temperature controlled rolling, which conditions the austenite for eventual ferrite nucleation, results in finer and deformed austenite grains to allow more nucleation sites for the ferrite to form.

2.4.2 Solid solution strengthening

The introduction of solute atoms into solid solution can produce stronger materials. As Figure 2.24 shows, there are two types of solid solutions depend on the relative size of the solute atoms compared to the solvent atoms. If the solute and solvent atoms have a similar size, the solute atoms will occupy the host lattice sites in the crystal structure of the solvent atoms which is called substitutional solid solution. The other type is called interstitial solid solution when the solute atoms are much smaller than the solvent atoms and can fit in the open space of the host solvent lattice, such as carbon, nitrogen, oxygen, hydrogen and boron. The alloying elements are added deliberately to cause distortion and distort the slip planes in the lattice and thus create strain in the vicinity to form barriers to the movement of dislocations.

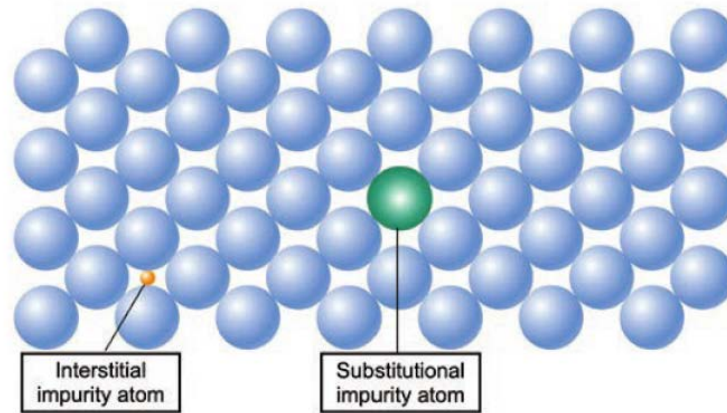


Figure 2.24 : Solid solution strengthening mechanism

The shear stress required to move dislocations in a material is as follow equation:

$$\Delta\tau = Gb\sqrt{c}\varepsilon^{\frac{3}{2}} \quad (2.8)$$

where c is the solute concentration, G is the shear modulus of the solute atoms and ε is the strain caused by the solute. It can be seen that with increasing solute concentration, the yield strength will increase. Figure 2.25 shows the effects of different substitutional alloying elements on the yield strength of ferrite grains, it can be seen that carbon and phosphorus are the most effective elements, but they have detrimental effect on the toughness or weldability. Overall, they have a modest strengthening effect^[82].

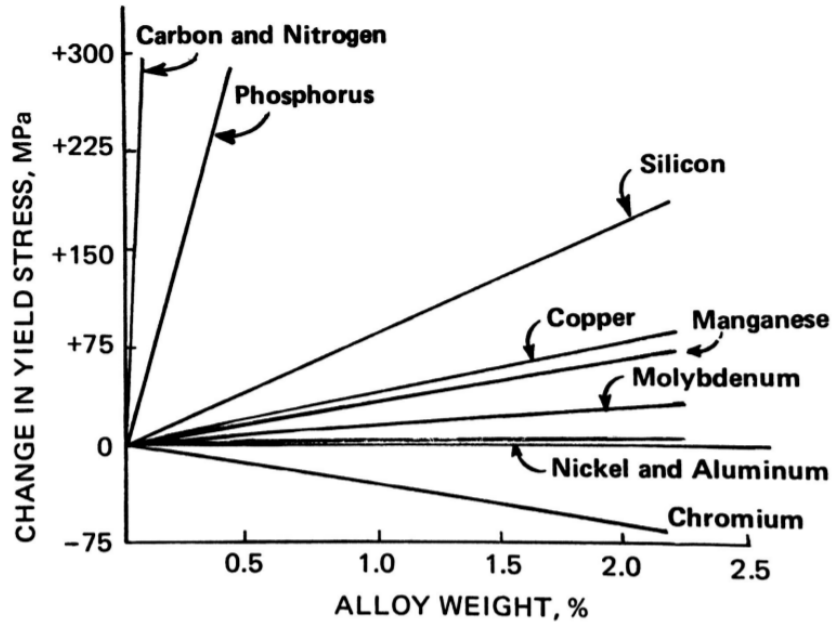


Figure 2.25: Solid solution strengthening of ferrite

Generally, the solid solution strengthening depends on the concentration of the solute atoms, shear modulus of the solute atoms, size of solute atoms and the symmetry of the solute stress field, because for non-symmetric stress fields, solutes can interact with both edge and screw dislocations which causes higher strength. Whereas in symmetric stress fields, where only volume can change, they can only interact with edge dislocations^[83]. Those dislocations will be pinned by the solute atmosphere, and their motion is severely restricted until the applied force is high enough which enable the dislocations to rip free and move through the lattice^[84].

2.4.3 Transformation strengthening

Depending on the chemical composition and thermomechanical processing, i.e. solution temperature, deformation temperature, cooling rate, finish cooling temperature, different types of microstructural products could be formed from the austenite. Both alloying elements and faster

cooling rates can depress the transformation from austenite to ferrite and result in the formation of bainite or martensite. Figure 2.26 shows the tensile strength range of ferrite plus pearlite, bainite and martensite^[85]. It can be seen the strength increases dramatically with the introduction of low temperature transformation products.

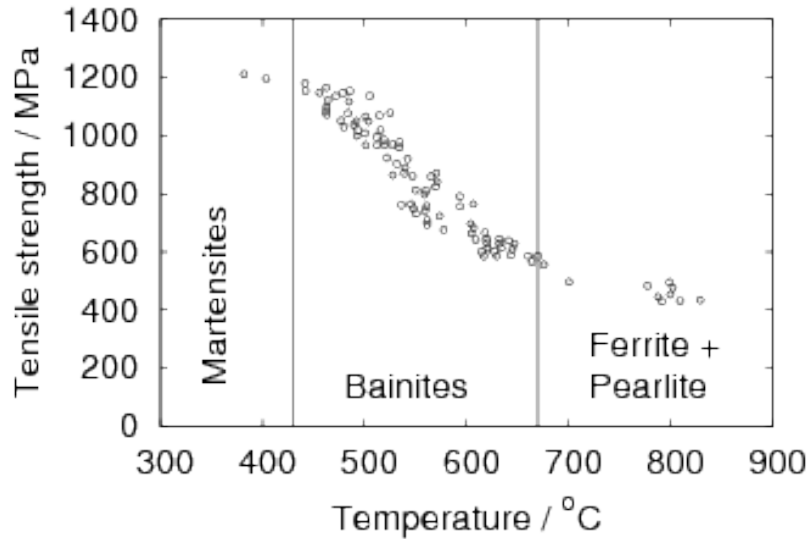


Figure 2.26: Strength variation with temperature of maximum transformation rate in steels with 0.1 wt% carbon after Pickering

The transformation of austenite to martensite or bainite are both based on the diffusionless shear-type or displacive-type mechanism, and the higher strength implies that there are many obstacles to impede the movement of dislocations in this structure. Kelly and Nutting^[86] found that conventional martensite has a plate-like structure with an internal parallel twin structure of about 0.1 μm thick within it. Another type of martensite has a block structure which contains a high density of dislocations of 10^9 to 10^{10} mm^{-2} . Bainite also has a structure containing a lot of barriers such as the boundaries from the subunits, packet and block walls^[45]. Since there are several forms of ferrite, with different transformation and strengthening mechanisms, the observed strength can vary among the different types of ferrite, from acicular ferrite, massive ferrite,

non-polygonal ferrite to polygonal ferrite, because of the different dislocation densities introduced into the matrix.

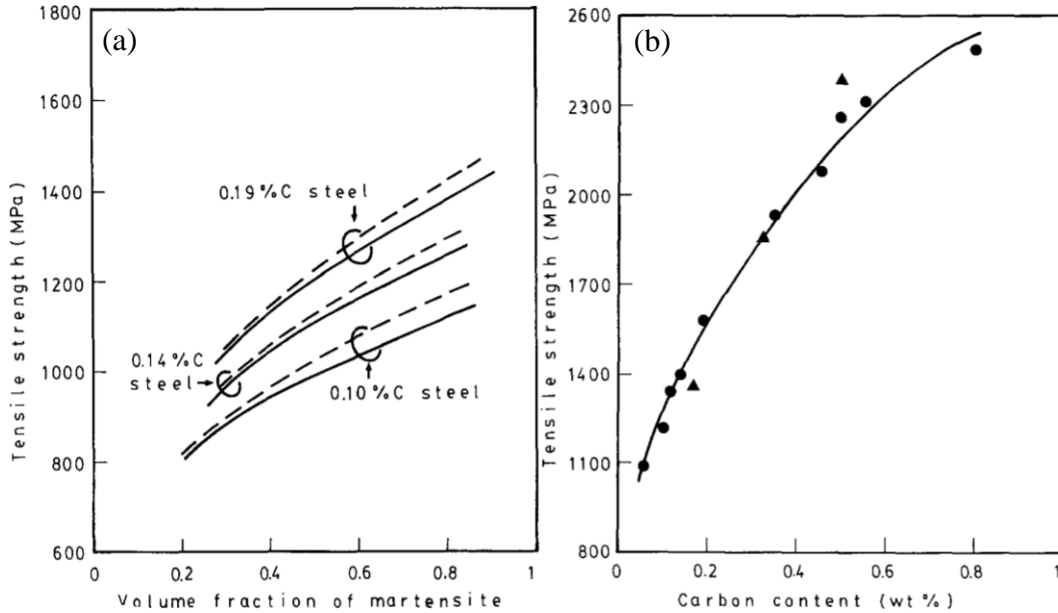


Figure 2.27: (a) Tensile strength of DP steel as a function of volume fraction of martensite with different carbon concentration; (b) Effect of carbon on the tensile strength of martensite

As shown in Figure 2.27, the strength of a dual phase steel depends on the strength of martensite phase, as well as the volume fraction of martensite^[87]. Even within the same microstructure, different carbon compositions also have an important influence strength on strength in the full martensite structure, as quenched from austenite. The strength of martensite is caused by dislocation-carbon interaction much like strain aging, with the dislocations coming from the displacive lattice transformation. The dislocation-carbon couples and their associated lattice strain, would restrict the motion of dislocations based on the solid solution strengthening method.

Through a thermomechanical processing, if the austenite at high temperature has been rolled heavily before any transformation occurs and then quenched to a temperature below M_s . A combination of low deformation temperature and high reduction amount could yield a steel with a

highest strength, because of the higher dislocation density in the martensite and precipitates formed within it, the dislocations would have much more difficulties to move.

2.4.4 Precipitation strengthening

When the solutes exceed the solubility limit of a matrix phase, nucleation and growth of second phase particles will occur. When a single-phase field (γ) rapidly cooled down after a solution treatment under the solvus line, it is possible to form a supersaturated phase (α) instead of a two phase matrix ($\alpha+\beta$) as would be expected under an equilibrium condition. The absence of the β phase is due to the lack of diffusion time during the fast cooling process. The supersaturated α phase will form precipitates of β particles within the α grains or on the grain boundaries if the material was followed by heat treatment at an elevated temperature (below the solvus line) which is called aging, and this process will allow sufficient time for the diffusion to place.

There are multiple factors can affect the effect of the precipitation strengthening results, i.e. the heat treatment parameters, the size and volume fraction of the precipitates. The onset of precipitation strongly depends on the aging temperature. When the aging temperature is close to the solvus line, the driving force is limited to push the proceeding of precipitation, however, when the aging temperature is too low, although the driving force becomes larger, the diffusion kinetics won't allow the second phase particles to grow fast. An optimal temperature for the rapid precipitation is to choose an intermediate aging temperature with a good combination of both nucleation and growth rates.

$$N = K \exp\left(\frac{-\Delta G^*}{kT}\right) \cdot \exp\left(\frac{-Q}{kT}\right) \quad (2.9)$$

where K is a constant, ΔG^* is the diffusion activation energy, Q is the activation energy, T is the absolute energy, k is the Boltzmann constant.

The developing process of the precipitation can mostly be described as taking place in three stages. The first one is called incubation period, clusters of solute atoms form and second phase particles nucleate and begin to grow either homogeneously within the grains or heterogeneously along the grain boundaries sites. In the second stage which is called nucleation period, particles nucleation continues along with the growth of existing precipitates, and these processes continue until the equilibrium volume fraction of the second phase has been reached. In the final stage, those existing particles coarsen, with larger particles growing at the expense of the smaller ones, in order to reduce the total amount of interfacial area between the two phases.

As Figure 2.28 shows^[88], as the precipitation proceeds, the hardness or the strength of the material increases at first, then it will reach a maximum value, then the material softens as the process continues. The strength contribution from precipitation is a result of combination of volume fraction, distribution, and nature of the precipitates, during incubation and nucleation phase, as more and more precipitates appear, and their size is still small enough to exert the pinning effect to the movement of dislocations which can strengthen the material, as the process enters into the third phase, the small precipitates will aggregate to form larger particles which no longer act as barriers to the dislocations and that is called over aging. Figure 2.28 also shows the aging process under different temperatures, it can be noticed that under higher temperature, the strength can reach to its peak value sooner, whereas, with less undercooling values, the material gets less saturated which lowers the peak value.

The changing of strength vs. temperature is associated with the interaction between the particles and dislocation depends on whether the dislocations are able to cut through a particle^[89] or forced to loop around it^[90]. When a particle is small and with coherent interphase with the matrix, the misfit strain is limited. A dislocation can cut through a precipitate without raising the

overall energy too much since the interfacial energy of coherent precipitates is small. And the strength is proportional to the radius or size of the particle. If the misfit strain is large, or the particles are too hard or incoherent with the matrix, the dislocations cannot cut through the precipitates, but rather loop around individual particles. And the stress needed for the looping is controlled by spacing between particles or bypass them by cross slip of screw dislocations or climb of edge. The stress needed for the looping is controlled by spacing between particles, and as the aging proceeds, for a given volume fraction of precipitates, the spacing decreases as the particles grow coarser.

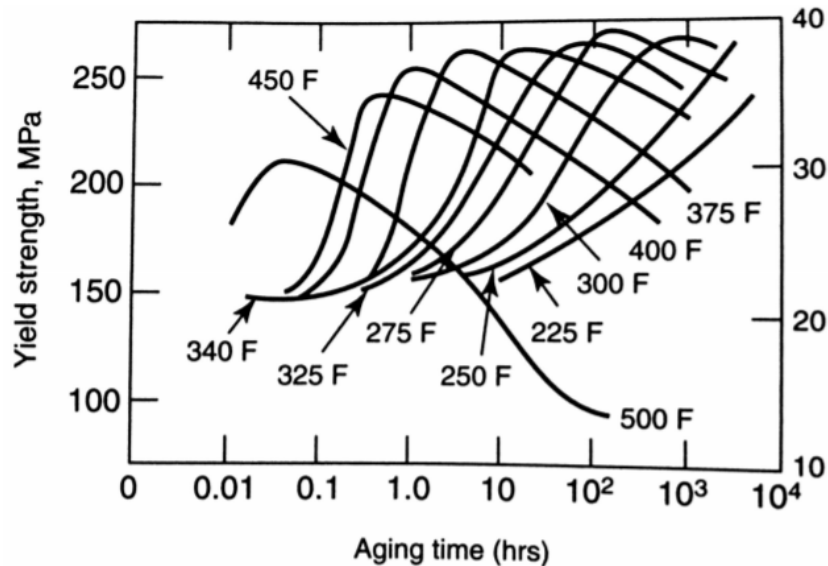


Figure 2.28: Effect of aging time on the yield strength for precipitation in FCC systems such as aluminum alloys

Since the strengthening particles in ferrite are microalloyed carbides or nitrides, they are ordered intermetallic compounds with very high Peierls Stress. Also, since they have complex crystal structures (B1, NaCl), they cannot be coherent with the ferrite matrix. These two facts mean that these particles cannot be sheared by dislocations, but rather strengthen by the Orowan-Ashby bypass mechanism^[91]. Therefore, the highest particle strengthening will occur

when there is a large volume fraction of very small particles. This strengthening is often expressed as Gb/λ , where G is the shear modulus of the ferrite, b is the Burger's vector for ferrite and λ is the interparticle spacing on the slip plane^[80].

2.5 DUCTILE FRACTURE MECHANISM

Fracture is the separation, or fragmentation, of a solid body into two or more parts under the action of stress^[80], where the whole process is made up of crack initiation and crack propagation. It can be classified into two types with respect to the characteristic of strain to fracture mode^[92], brittle fracture and ductile fracture. Ductile fracture was usually accompanied by the occurrence of an appreciable amount of plastic deformation, while brittle fracture was a result of a rapid crack propagation, without any gross deformation presented. The fracture mode from ductile to brittle is changeable due to the temperature, strain rate and stress condition.

Ductile fracture is the most common fracture mode of failure in metals at room or higher temperatures. The damage mode involves the nucleation of voids at non-metallic inclusions, followed by a phase of damage growth and coalescence driven by plastic deformation^[93-95]. Figure 2.29 shows the stages of ductile fracture during tensile test. It can be seen the voids appeared during necking and aggregate to form micro-cracks, as the deformation proceeds, those micro-cracks can link to each other to become a major crack and keeps propagating until the final failure.

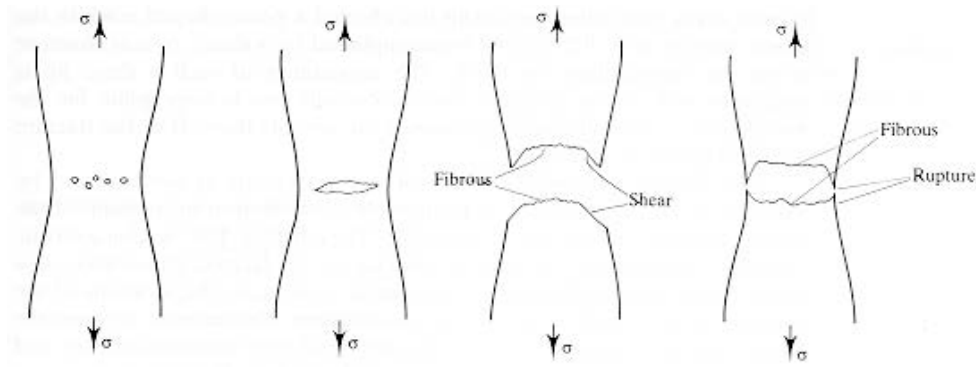


Figure 2.29: The stages in the ductile fracture of a tensile test specimen

The main method of void nucleation is the decohesion of the interface between matrix and the inclusions (non-metallic inclusion) or the cracking of the second phase particles (cementite)^[96]. The former can occur at small strain, while the later one is a stress dependent phenomenon. The voids could be the source of ductile fracture which are nucleated heterogeneously at sites where compatibility of deformation is difficult. The preferred sites for voids formation are inclusions, second phase particles, or fine oxide particles, located either within the grains or along the grain boundaries^[97-103]. The nucleation of voids is a discontinuous process made of succession of discrete nucleation events. They first nucleate on the largest inclusions, which may have the largest internal or interfacial defects, and the existence of different types of second phase particles or inclusions could also accelerate the process, due to the different resistance to void nucleation and different sizes. This inhomogeneity in particle distribution can cause local stress concentrations and is certainly an important reason for heterogeneous nucleation. And the location of fracture in the through thickness of plate was found to be non-random, reflecting inclusion distribution patterns in the original ingot.

Once the voids were formed, they would grow up with the help of the strain intensification which occurs in a manner analogous to stress intensification near the notches or voids (Figure

2.30^[104]), and it is controlled by the frontal radius of curvature of the void according to Henry and Plateau^[93].

$$d\varepsilon = db/b(1 + ka^2/b^2) \quad (2.10)$$

then integration of this equation provides a description of the development of the void with strain.

$$\varepsilon = \varepsilon_0 + \ln[(b^2 + ka^2)/(L^2 + ka^2)]/2 \quad (2.11)$$

where ε is the strain and ε_0 is the strain at which void nucleation occurs, a and b are major and minor length of the ellipse of the void, k is the strain intensification factor, L is the initial length of the void, i.e., b_0 , in this case of particle decohesion (Figure 2.30), and k is the strain-intensification factor, R is the frontal radius of curvature, b^2/a .

The crack growth in ductile fracture is essentially by a process of void coalescence. There are two modes of void coalescence. One is produced by the internal necking mode of coalescence where the ligament between two voids shrinks with a shape typical of a necking process ^[105]. Another mode consists in shear localization between large primary voids which is frequently observed in high strength low strain hardening materials ^[106]. Coalescence occurs by elongation of the voids and elongation of the bridges of material between the voids. This leads to the formation of a fracture surface consisting of elongated dimples as if it had formed from holes which were separated by thin walls until it fractures. Limited literature has been found to describe the critical distribution of voids required for void coalescence. However, a critical ratio of hole size to hole spacing has been mentioned ^[93]. A modified model of ductile fracture from Henry and Plateau for hole spacing, in which the resultant equation implies a critical-volume fraction of holes ^[96]. The factors that encourage the early development of the critical-volume fraction of holes are those which reduce fracture strain, including a high volume fraction of inclusions and an unfavorable shape which would promote strain intensification.

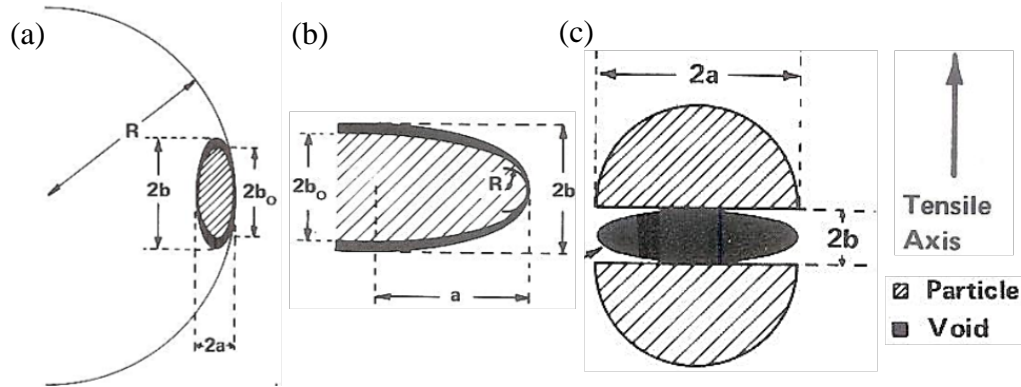


Figure 2.30: Theoretical models for void growth (a) Decoherence (Prolate Spheroid); (b) Decoherence (Oblate Spheroid); (c) Particle Cracking

2.6 TOUGHNESS MECHANISM

Toughness is measurement of resistance to fracture in a unit of energy. It is a combination of both strength and ductility of a material. Neither a very high strength nor superior ductile material can absorb large energy during the fracture. From Figure 2.31, it shows that medium carbon steel can absorb much more energy than both high and low carbon steels. For a smooth tensile bar, the energy that is absorbed before fracture can be loosely estimated from the area under the stress-strain curve:

$$\text{Energy/volume} = \int_0^{\epsilon_f} \sigma d\epsilon \quad (2.12)$$

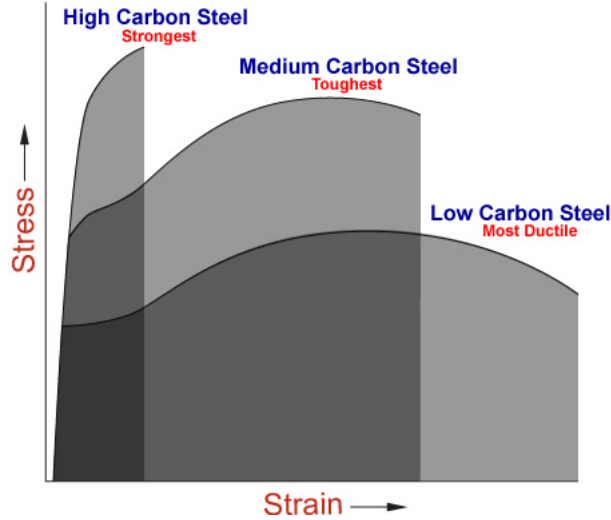


Figure 2.31: Energy absorbed in a tensile test with different steels

There are multiple ways to improve the toughness of a material. To avoid brittle cleavage fracture, a good method is through microstructure refinement, from Hall-Petch equation, we know that the grain boundary mechanism could bring an improvement in both strength, toughness (avoiding cleavage) and ductility. One explanation for that during fracture, a microcrack can be stopped by an effective barrier more often in a finer microstructure. As a result, the crack has to form again in order to continue the process, which would consume more energy. The relationship between the toughness (brittle fracture resistance) and grain size can be shown below according to Cottrell and Petch^[78, 84]:

$$\sigma_f = \frac{4G\gamma_m}{k_y} d^{-\frac{1}{2}} \pi r^2 \quad (2.13)$$

where σ_f is the fracture stress, G is the shear modulus, $\frac{4G\gamma_m}{k_y}$ is the plastic work done around a crack as it moves through the crystal, k_y is the dislocation locking term from Hall-Petch relation and d is the grain size.

In order to resist ductile fracture, another way is to improve the cleanliness of the steel, like reducing the amount of oxygen and sulfur inside the steel, because the formation of oxides and

sulfides will lower the resistance to ductile fracture or ductile toughness in the steel^[107-109]. Even during the thermomechanical processing, the inclusions can be deformed along the rolling direction, generating a considerable anisotropy in ductile fracture properties and result in very poor transverse fracture toughness. Besides that, minimizing the volume fraction of second phase particles and inclusions inside the material will also increase the ductile fracture toughness. From previous part, it is known that the fine particles could be tangled with dislocations, make it difficult for them to move, and act as a strengthening factor. However, in fact, some particles with a low thermostability could end up with a coarse size and provide no strengthening increment. Instead, those regions will have a high stress concentration during the deformation and provides sites for the cracks to initiate^[110, 111].

Various types of methods can be used to determine the toughness of a material. The most common one of them is the called Charpy V-notch impact test. A standard size of the test specimen has a square cross section of 10 x10mm and contains a 45° V notch, 2mm deep with a 0.24mm root radius. During the test, the specimen is fixed to the instrument in a horizontal position and loaded behind the notch by the impact of a swing pendulum. And the energy consumed during the fracture is recorded.

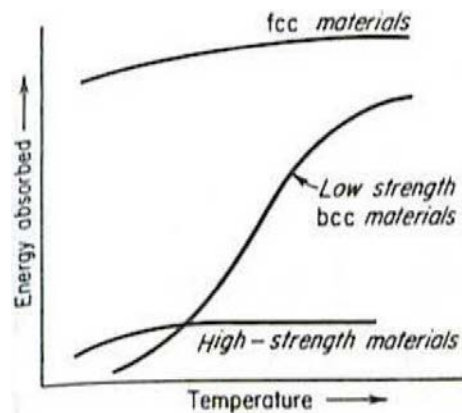


Figure 2.32: Charpy V-notch result of different materials at different temperature

From Figure 2.32, it shows that for the low strength bcc material the toughness highly depends on the temperature. At low temperature, the fracture occurs by brittle cleavage while at high temperature, the fracture occurs in ductile rupture. And there exist a temperature range where the transition of the fracture mechanism changes called ductile to brittle transition temperature (DBTT). Any fracture that happens above the DBTT is a ductile fracture, and with lower DBTT, the greater the fracture toughness of the material. This transition temperature can be affected by the chemical composition of the steels, the microstructure and the grain size. Low DBTT indicate superior behavior. Since ferrite grain refinement results in lower DBTT, many research programs are conducted on how to achieve this refinement^[112, 113]. As good austenite conditioning during the hot rolling of austenite leads to high values of S_v and fine ferrite grain sizes, controlled rolling and controlled cooling are important in achieving cleavage resistant steels for critical structures^[19, 21].

3.0 STATEMENT OF OBJECTIVE

The automotive industry is pursuing steels with good combinations of strength, ductility and toughness in order to achieve more weight reduction while still satisfying all the safety requirements. The hot band steels for this application has been changing from common HSLA steels (ferrite/pearlite), to DP steels (martensite/ferrite) and TRIP steels (ferrite/martensite/retained austenite) over the past decades to obtain higher strength without sacrificing the ductility too much. However, the formability of the multi-phase steels is inadequate, which becomes an obstacle for wider applications in the industry.

The main purpose of this study is to develop a hot band steel which consists of a single phase and uniform ferrite matrix with precipitation strengthening. This approach is very different from the usual, where the DP or TRIP steels have multi-phase matrix microstructures consisting of mixtures of ferrite, bainite, martensite and retained austenite. The approach taken here takes advantage of the excellent ductility of the soft ferrite matrix which is strengthened by the microalloyed precipitates formed within it. Some similar research work has been done by JFE and TATA steel companies to produce steel grades with a single phase ferritic microstructure and precipitated with (Mo, Ti)C. These steel showed tensile strength up to about 1000MPa, but the elongation and hole expansion values were good. However, in this current work, the goal is to design steels and processing that can reach tensile strengths over 1200MPa and yield strengths over 1000MPa, and still have good ductility, toughness and hole expansion ratio values. Three

different finish rolling temperatures (870°C, 810°C and 750°C) were selected in order to have the best conditioned austenite phase, because a well-conditioned austenite will result in a finer room temperature microstructures which would provide better mechanical properties. Moreover, three different coiling temperatures (610°C, 530°C, 450°C) were chosen to find the optimum coiling temperature to form precipitates with the highest volume fraction and minimum particle size, and also to investigate the effect of phase transformation to the final mechanical properties. The specific objectives of this study are as follows:

1. Investigate the role of thermomechanical processing parameters like finish rolling temperature and coiling temperature on the formation of ferrite or bainite microstructure and the precipitation behavior during phase transformation and coil cooling.
2. Test the mechanical properties of the hot band in different type of methods, including hardness test, tensile test, Charpy V-notch test and hole expansion test. Explore the relationship between the mechanical properties and the microstructures, i.e. matrix phase, inclusions, precipitates.
3. The scientific hypothesis leading this research is that high levels of precipitating elements such as Ti and V will permit the precipitation hardening increment to be high enough in hot rolled coils that the property goals can be met with a single phase ferrite matrix.

4.0 MATERIALS AND EXPERIMENTAL PROCEDURE

4.1 MELTING, HOT ROLLING (THERMO-MECHANICAL) AND COOLING PROCESSING

The chemical composition of the steel investigated in this study is listed in Table 1. It had a 0.14 wt% C, 0.35 wt% Mo, 0.163 wt% Ti and 0.294 wt% V, those microalloying elements were extremely high compared to normal microalloyed high strength low alloy (HSLA) steels, where the total (Nb+Ti+V) rarely exceeds 0.2 wt%. The ingots were produced as lab heats and being hot rolled to 22mm thick plates for hot rolling experiments.

Table 4.1: Chemical composition of the steel (wt%)

| C | Si | Mn | P | S | S.Al | Mo | Ti | Nb | V | N |
|-------|-------|-------|-------|--------|-------|-------|-------|-------|-------|--------|
| 0.140 | 0.293 | 1.370 | 0.011 | 0.0034 | 0.049 | 0.350 | 0.163 | 0.002 | 0.294 | 0.0060 |

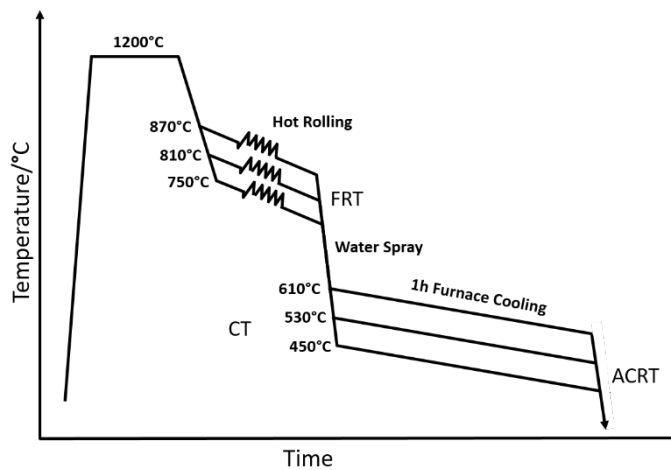


Figure 4.1: Thermo-mechanical processing

As Figure 4.1 shows, after a homogenization treatment at 1200°C to get complete austenitization, the steel was rough rolled and then finish rolled at temperatures (FDT) of 870°C, 810°C, 750°C to a 3mm plate, then rapidly cooled down to the coiling temperatures of 610°C, 530°C and 450°C, followed by 1 hour furnace cooling and finally air cooling to room temperature. Steels were then prepared for metallography and mechanical testing through standard metallurgical processing including cutting, mounting, grinding and polishing for different purposes. Those steels in the different metallurgical conditions will be denoted as in the Table 4.2.

Table 4.2: Processing parameters of the steels

| ID | PG11 | PG12 | PG13 | PG21 | PG22 | PG23 | PG31 | PG32 | PG33 |
|-----|-------|-------|-------|-------|-------|-------|-------|-------|-------|
| FDT | 870°C | 870°C | 870°C | 810°C | 810°C | 810°C | 750°C | 750°C | 750°C |
| CT | 610°C | 530°C | 450°C | 610°C | 530°C | 450°C | 610°C | 530°C | 450°C |

4.2 MECHANICAL TESTING

Different types of mechanical testing methods were applied to evaluate the mechanical properties of the materials. All the samples were machined from the hot bands provided by POSCO.

4.2.1 Micro-hardness

Hardness of a material can show the resistance of a sample to plastic deformation ^[80], and its value can correspond to the ultimate tensile strength, thus, it could be a convenient way to estimate the strength of a material (TS=3.25VHN). In this study, the Vicker's criterion is used to evaluate the hardness. According to ASTM E92-82 ^[114], the Vickers hardness number (VHN) is

defined as the load divided by the surface area of the indentation, and it is determined from the following equation:

$$\text{VHN} = \pi r^2 \frac{F}{A} = \frac{2F}{d^2} \sin \frac{136^\circ}{2} \approx \frac{1.8544F}{d^2} \quad (4.1)$$

where d is the average diagonal length of the impression left by the indenter, F is in kgf^2 and d is in mm.

In this study, the Vicker's hardness number was obtained with Intron hardness test machine with a test load of 300gf and 10s dwell time.

4.2.2 Tensile test

Tensile testing is a basic material test in which a sample is subjected to an increased elongation until failure, while the changing load is being simultaneously recorded. The important mechanical properties such as ultimate tensile strength, yield strength, uniform elongation and total elongation can be directly measured via a tensile test. From these measurements, the following properties can also be determined: Young's modulus, Poisson's ratio and strain-hardening exponent.

The tensile test was conducted at room temperature at a strain rate of 1.1×10^{-3} per second with an Intron Microforce Testing System (MTS). The sub-sized specimens were machined out from the hot band with a gauge length of 1 in, width of 0.25in and the thickness of the original material according to ASTM E8^[115] along the rolling direction.

4.2.3 Charpy V-notch test

According to ASTM E2248^[116], the Charpy V-notch impact test is a standardized high strain-rate test which can determine the amount of energy absorbed by a material during fracture. The

absorbed energy is used to evaluate a given material's notch toughness and to study the temperature-dependent ductile-brittle transition.

The specimens were machined with a cross section of 10×2.5mm and a length of 25mm along the transverse direction. The test was conducted at -40°C.

4.2.4 Hole expansion test

Hole expansion test is used to evaluate the stretch flange formability of steels sheets, and is expressed as the hole expansion ratio (HER). The HER value of a sheet is usually obtained by expanding initially punched 10mm diameter holes using a cylindrical or conical punch at a constant speed, the schematic of this test is shown in Figure 4.2. The hole is located in the center of a 100mm by 100mm steel sheet with a diameter of 10mm. The hole is prepared by a high speed punch in an off campus facility. The test was conducted by using a conical punch at a speed of 0.3mm/s. The test continued until a through thickness crack was observed on the inner diameter of the hole. The HER test sequence was studied using a camera attached to the HER test rig. Run from surface to surface, the test was considered completed, and the final hole diameter measured.

The hole expansion ratio (HER) is defined by the following equation:

$$\text{HER} = \frac{D_f - D_0}{D_0} \times 100\% \quad (4.2)$$

where D_f is the final inner hole diameter and D_0 is the original hole diameter.

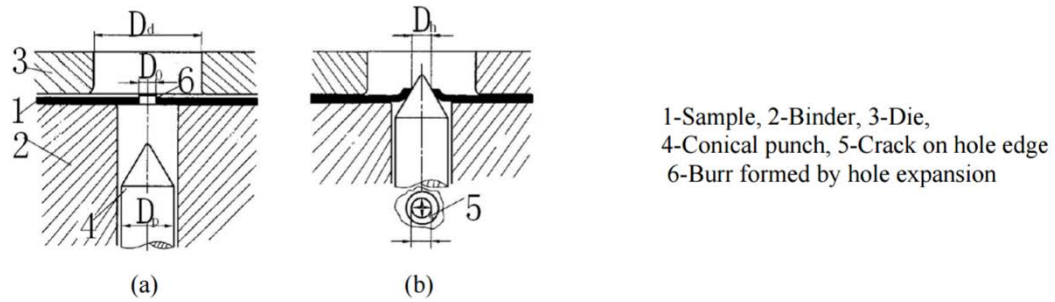


Figure 4.2: Schematic of hole expansion test

4.3 MICROSTRUCTURE ANALYSIS

Multiple types of characterization techniques were applied to analyze the microstructure of the various conditions of the steel. The specimens were ground through a series different grit of silicon carbide abrasive papers and then being polished with 0.5um alumina powder in a Vibromet 2 Vibratory Polisher machine for several hours to remove nearly all the defects on the surface. Specimens were characterized by optical microscopy (OM) and scanning electron microscopy (SEM) with or without being etched for different purposes. Electron backscattered diffraction (EBSD) was conducted at working distance of 16-18mm and 20KeV. Different step sizes were used at different magnifications. Transmission electron microscopy samples were prepared from a 0.05mm thick, 3mm diameter disk which were further thinned by electro-polishing for characterization of nanometer-sized precipitates and detailed microstructures, assisted with the use of energy-dispersive spectrometer (EDAX).

4.3.1 Optical microscopy

Optical microscopy (OM) was used to analyze the microstructures with magnification up to 2000 with Nikon FX-35WA and 5000 with Keyence Microscope. OM can help to identify different microstructures based on the etching of boundaries or different colors of phases. Different etchants can be used to reveal different phases or structures. For example, 2% Nital was the most common etchant used to reveal the grain boundaries. Ferrite will show in white grains and carbide show in dark. Alkaline sodium picrate solution was used to reveal the prior austenite grain boundaries and martensite austenite (M/A) constituents. And the phase fraction calculation and grain size measurement are all based on the OM images processed through Image J software afterwards.

4.3.2 Scanning electron microscopy

Philips XL-30 and ZEISS Sigma500 VP field emission scanning electron microscopy were used to analyze microstructures at a higher magnification up to 100,000. More detailed morphological and crystallographic information of microstructures and defect structure can be obtained compared to the optical microscopy in order to distinguish different phases and other details such as precipitates or dislocation densities. Specimens used in the SEM should be mounted in conducting powder and/or attached to conducting tapes to increase conductivity in order to get better quality of images. Smaller phases like bainite or M/A islands or even some precipitates can be better observed through SEM. EDS attached to SEM can help to perform an element identification analysis.

4.3.3 Electron backscattered diffraction

Electron Backscatter Diffraction (EBSD) was used in this study, as it allows the measurement of local crystallographic orientations in reasonably perfectly polished specimens, as any deformation due to mechanical grinding or polishing has to be avoided since it directly influences the pattern quality. EBSD was conducted on FEI Apreo SEM. The TEAM OIM data collector software was used for the collection of all the EBSD data and the TSL OIM software was used for general analysis. The specimen is tilted at 70° from a horizontal stage to allow the CCD camera to collect the Kikuchi patterns which are formed when a stationary electron beam interacts with a crystalline lattice in the SEM^[117]. The EBSD data are collected by moving the electron beam to points on a regular grid of interest. The data provides a wide range of post-processing possibilities, e.g. related grains, grain boundaries, misorientations and texture.

The EBSD data was acquired with a step size of 0.1 to 0.4 μm depending on the grain size or magnification at a hexagonal grid mode.

4.3.4 Transmission electron microscopy

In order to obtain more detailed information of the microstructure of the materials, i.e. dislocation, precipitates, martensite-austenite constituent, TEM FEI Tecnai G2 was used in this study.

Thin foils were prepared for the TEM observations. They were cut from the hot band from selected locations by a Buehler diamond disk cut off machine and then ground to about 80 μm in the thickness, the thin sheets were then punched into 3mm diameter disks. The disks were then electrochemically polished at room temperature by using a Struers Tunepol Jet polisher. The electrolyte solution used for the polishing is a mixture of 90% ethanol and 10% perchloric acid and

the polisher was operating at 8V and 70-90mA. The samples should be cleaned with ethanol before the TEM examination.

Carbon extraction replicas were prepared for observation of precipitates in the TEM. The thin film deposition was made from a Denton DV-502 Bell Jar Vacuum Evaporator. Then the film was etched in the 10% Nital to dissolve the matrix underneath, and the film was peeled off from the matrix by dipping the sample into distilled water or ethanol. The film then was placed on a copper grid for the observation in TEM.

5.0 RESULT

5.1 MICROSTRUCTURES OF THE HOT BAND

After full processing, the hot bands were sectioned, mounted, ground and polished through standard metallurgical preparation steps. The observation area was on the surface containing the rolling and normal directions. The microstructures obtained at different finish rolling temperatures and coiling temperatures were first analyzed by optical microscopy. Figures 5.1 to 5.3 show the optical microstructures of all the hot bands after being etched by a 2% Nital solution.

Steels with the same coiling temperature seem to have similar microstructures, the finish rolling temperature did not have an obvious influence on that, while the microstructure between each coiling temperature were quite different. At the highest coiling temperature of 610°C, the microstructures shown in Figures 5.1(a), 5.2(a) and 5.3(a) are characterized by acicular and equiaxed ferrite grains. As for the other conditions with lower coiling temperatures of 530°C and 450°C, the microstructures were more complexed, the shape of ferrite grains becomes more irregular, in addition, second phase microstructures besides the ferrite were observed.

In order to get a better identification of the microstructures, SEM micrographs of the steels conditions at different finish rolling and coiling temperatures are shown in Figures 5.4-5.6. From them, more detailed information and a much clearer morphological analysis of the microstructure were obtained. Figures 5.4(a) and (b), 5.5(a) and (b) and 5.6(a) and (b) show the microstructures

of steels with the 610°C coiling temperature but with different finish rolling temperatures. It can be seen that the microstructure is mixed with mostly polygonal ferrite or equiaxed quasi-polygonal ferrite grains, and some acicular ferrite grains as marked in the figures. The grain size looks uniform. As the coiling temperature drops down to 530°C, which shown in Figures 5.4(c) and (d), 5.5(c) and (d), 5.6(c) and (d), it can be noticed that there exist some regions with very coarse quasi-polygonal ferrite grains with a major length along the rolling direction. Moreover, those second phase regions observed through OM can be identified as martensite/austenite (M/A) constituents in the SEM. Those M/A islands dispersed within the ferrite grains or on the grain boundaries are typical of what is called granular bainite. A different etchant was applied in the following part for a better observation of the M/A islands. With further cooling to the coiling temperature of 450°C, the overall microstructure is similar to those of 530°C, except the quasi-polygonal ferrite grains regions were coarser, and upper bainite also appears, which can be seen from Figures 5.4 (f), 5.5(f) and 5.6(f).

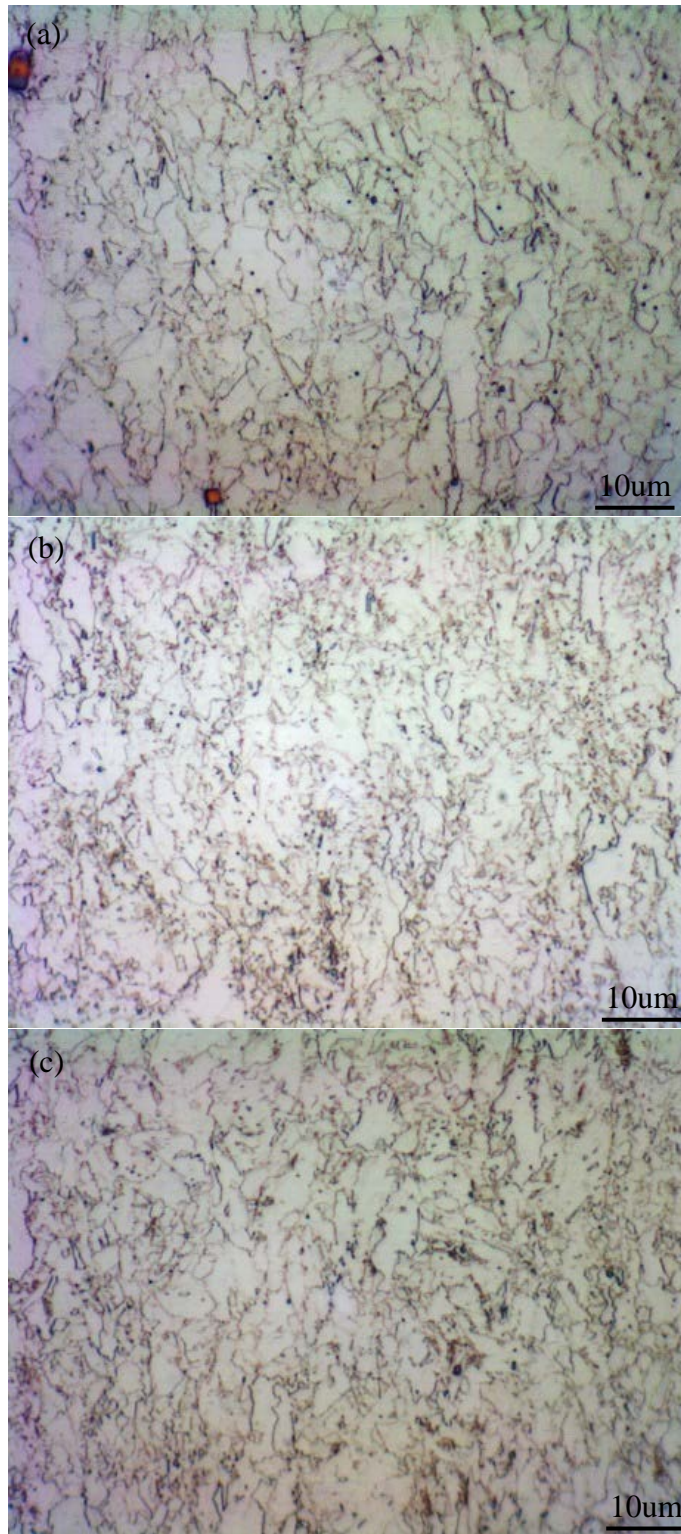


Figure 5.1: Optical microstructure of steels at finish rolling temperature of 870°C with coiling temperatures of (a) 610°C; (b) 530°C; (c) 450°C

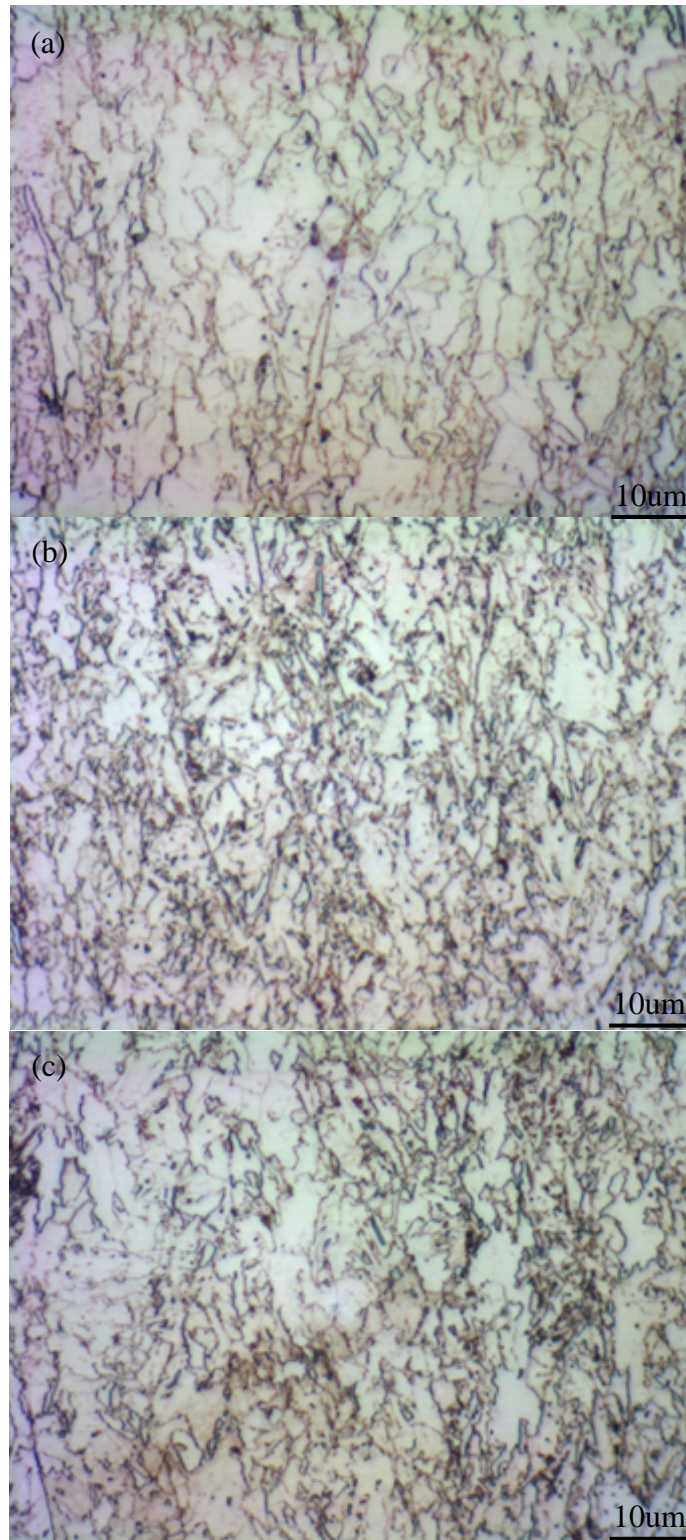


Figure 5.2: Optical microstructure of steels at finish rolling temperature of 810°C with coiling temperatures of (a) 610°C; (b) 530°C; (c) 450°C

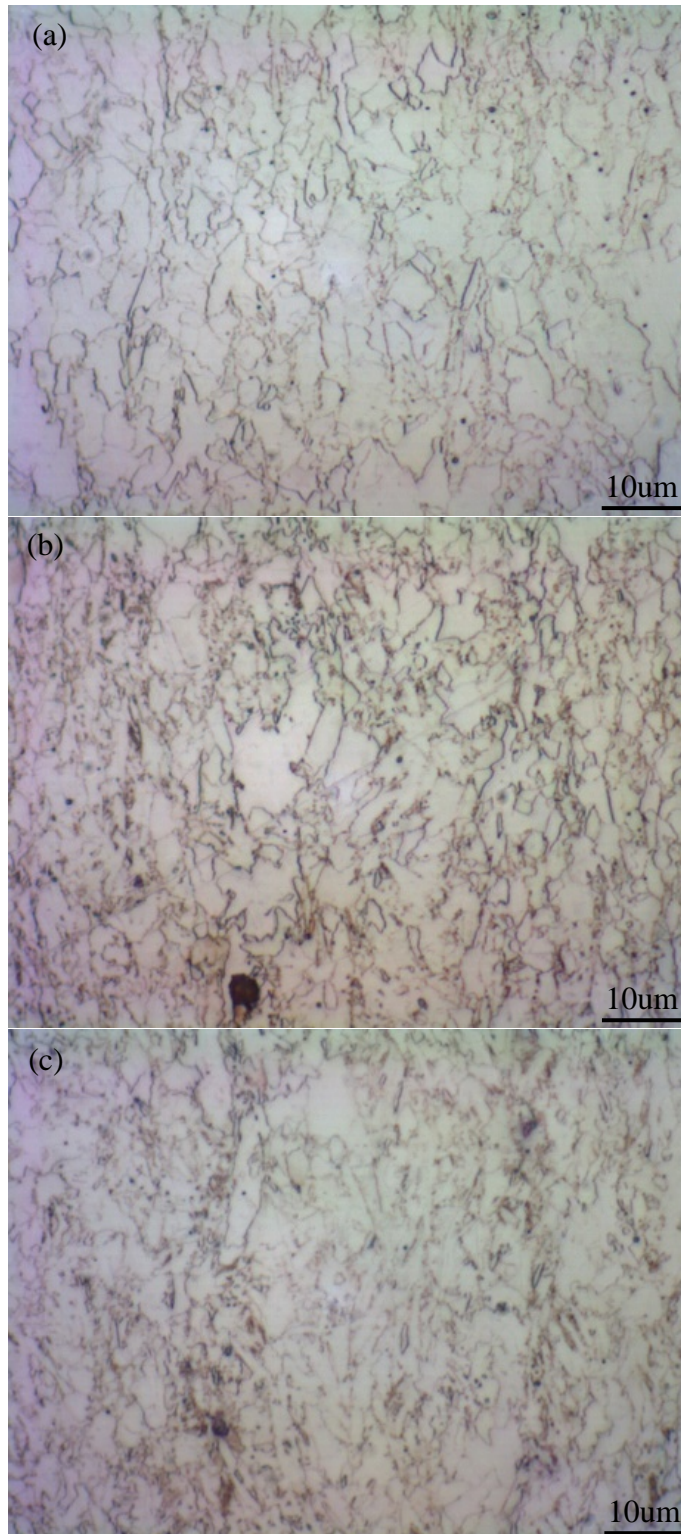


Figure 5.3: Optical microstructure of steels at finish rolling temperature of 750°C with coiling temperatures of (a) 610°C; (b) 530°C; (c) 450°C

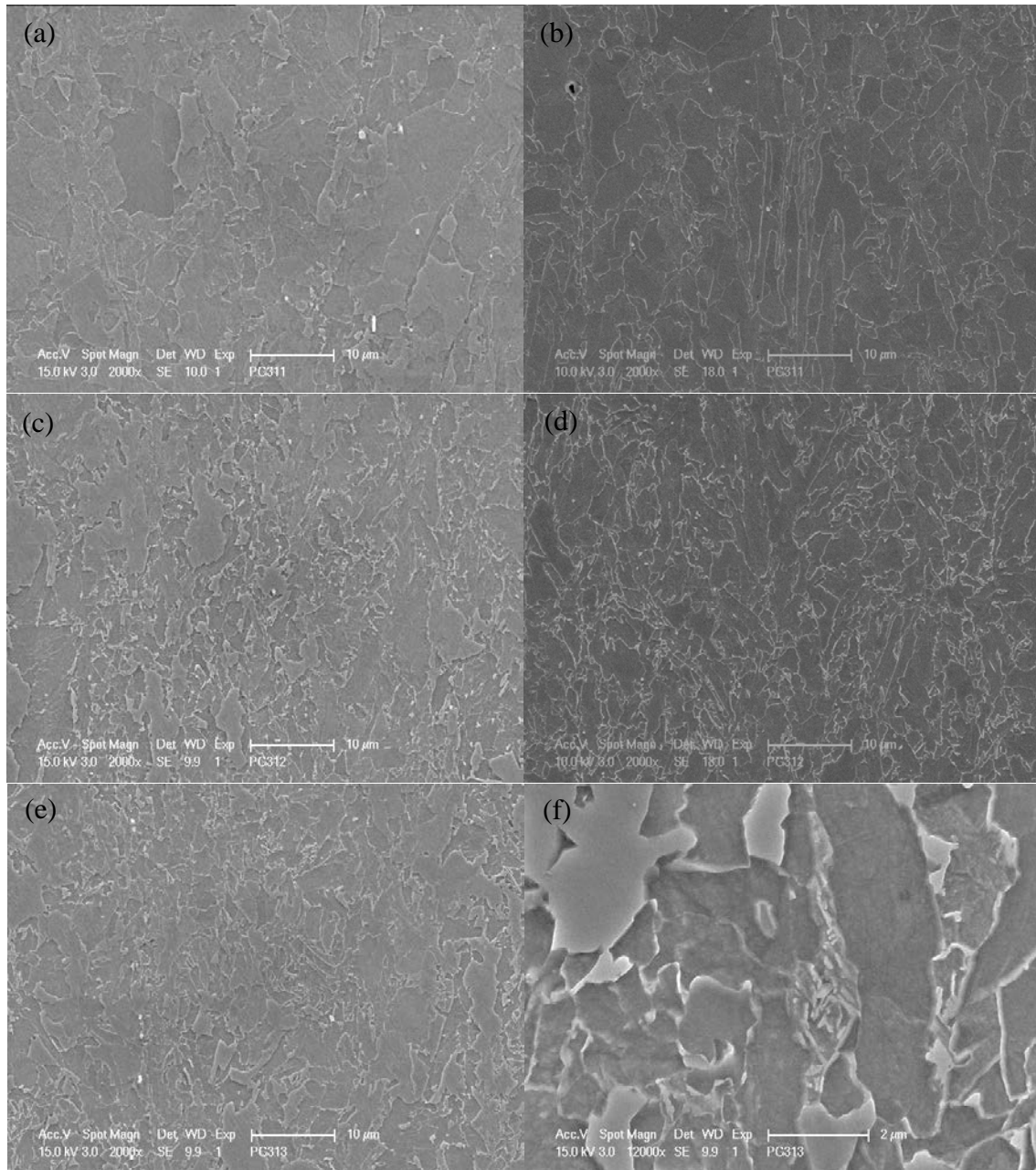


Figure 5.4: Scanning electron microstructure of steels at finish rolling temperature of 870°C with cooling temperatures of (a) and (b) 610°C; (c) and (d) 530°C; (e) and (f) 450°C

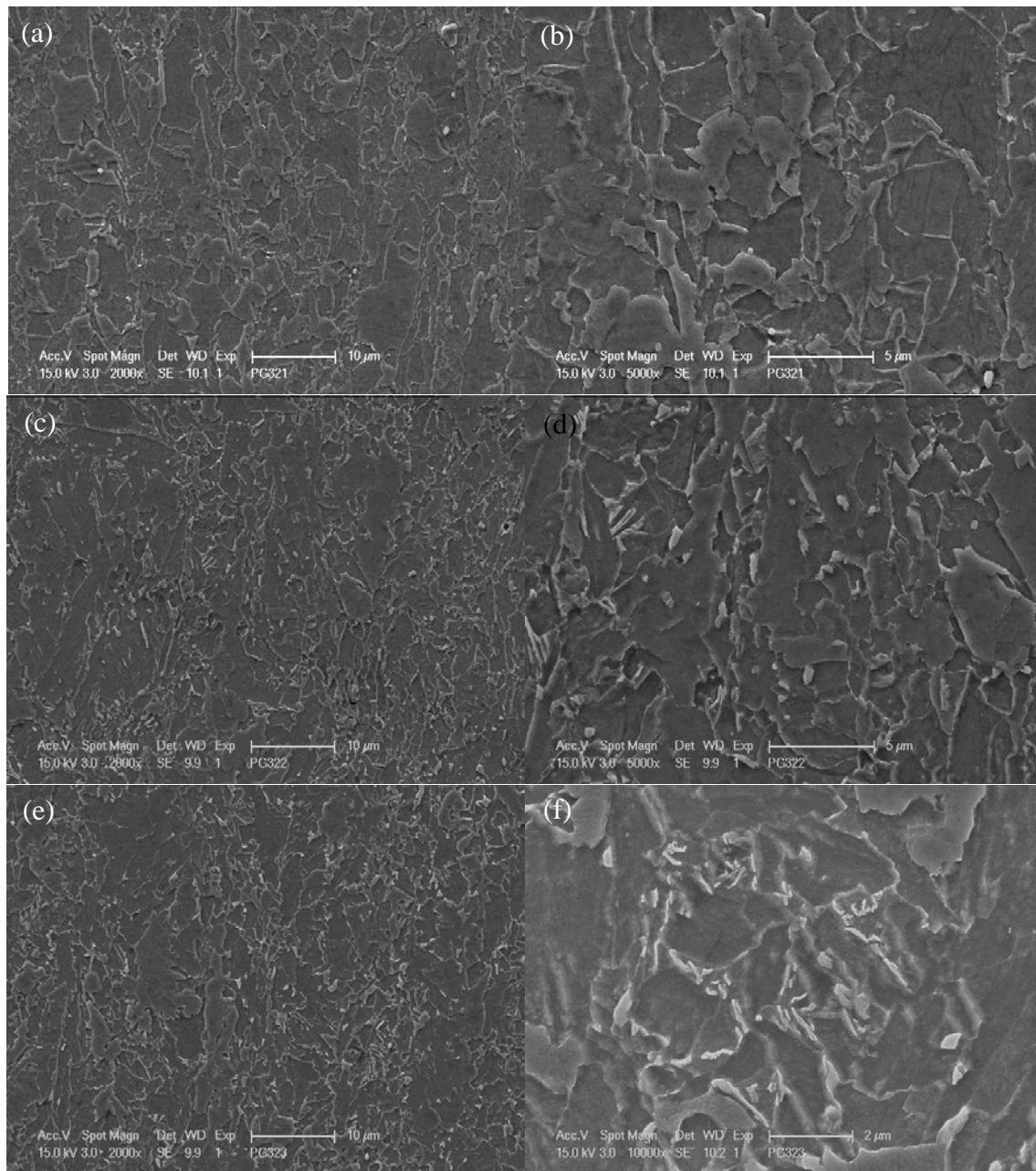


Figure 5.5: Scanning electron microstructure of steels at finish rolling temperature of 810°C with cooling temperatures of (a) and (b) 610°C; (c) and (d) 530°C; (e) and (f) 450°C

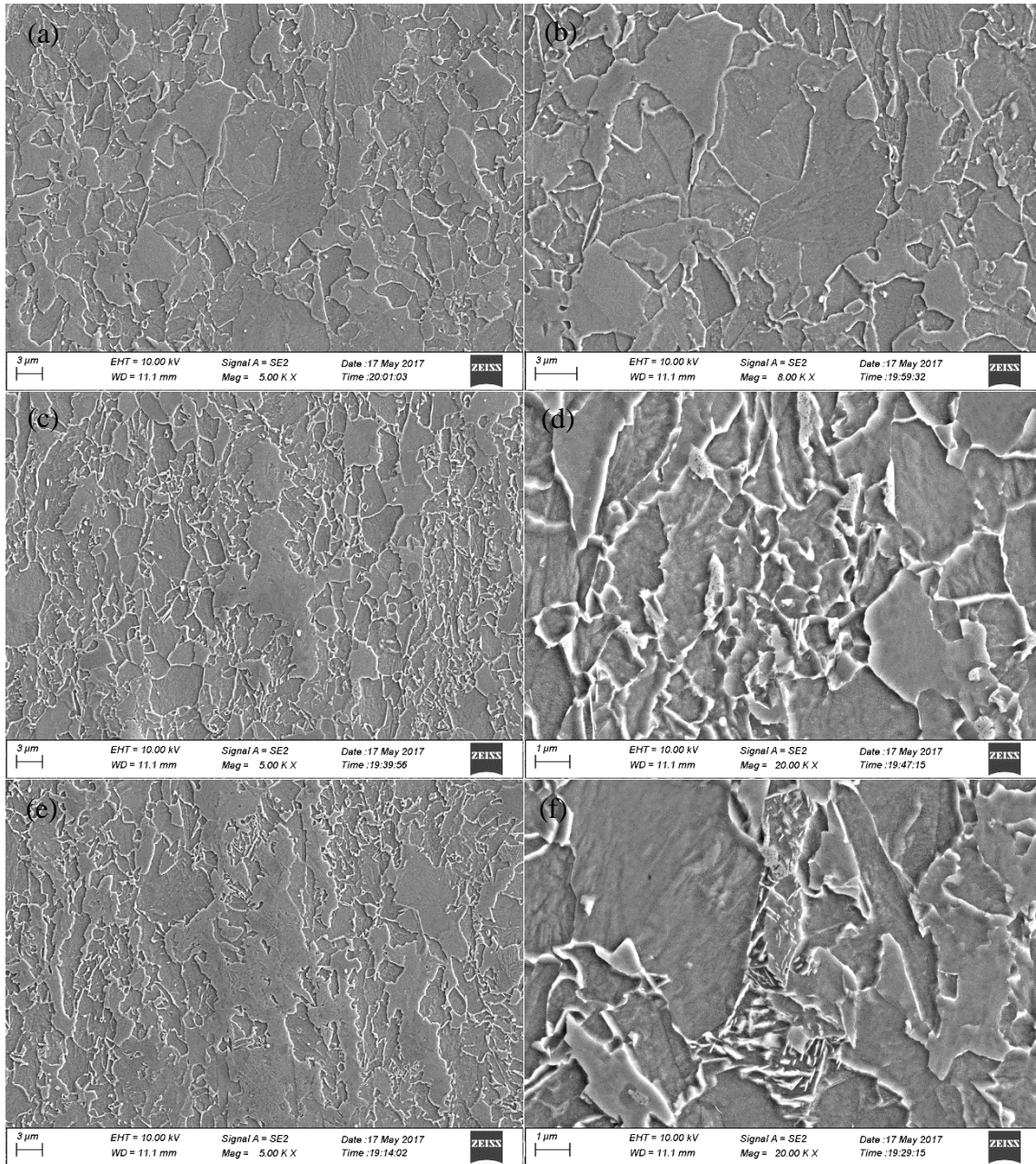


Figure 5.6: Scanning electron microstructure of steels at finish rolling temperature of 750°C with cooling temperatures of (a) and (b) 610°C; (c) and (d) 530°C; (e) and (f) 450°C

The observation of M/A was carried out by using a special electrolytic etching method. According to Ikawa and Bonnevie^[118, 119], the etching was conducted in alkaline sodium picrate solution at 6V for 2 to 4 minutes. Thus, the ferritic matrix will remain unetched, while the carbides,

will be preferentially etched and appear dark soon as shown in Figures 5.7(a), (c) and (e) to 5.9(a), (c) and (e). It can be seen that with light etching, despite the relatively low finish rolling temperature, none the specimens coiled at 610°C showed many carbides in the matrix, only the prior austenite grains start to show up in the background. However, as the coiling temperature dropped to 530°C and 450°C, large amounts of carbides can be seen. The result of the difference in coiling temperatures is that the specimens with the higher coiling temperature of 530°C show fine and uniformly distributed carbides while the steels with lower coiling temperature of 450°C exhibit a little coarser and segregated carbides which can also be seen from the optical micrographs also after 2% Nital etching. The morphology of carbides also varies with different coiling temperatures as shown in Figure 5.10. As Figure 5.10(a) shows, only a few can be found decorating the ferrite grain boundaries at the coiling temperature of 530°C. When the coiling temperature drops to 450°C, from the Figure 5.10(b), carbides with a lamellar structure show up inside the ferrite grains. At the highest coiling temperature (610°C), carbides can barely be seen, Once the steels were etched properly in the alkaline sodium picrate solution, it provided a good enough contrast to tell the difference in color between different phases. The white particles represent the M/A islands. It can be seen that in the 610°C coiled steels, no obvious M/A islands can be found, only the prior austenite grain boundaries get etched deeper. While for steels with coiling temperature of 530°C, some M/A islands can be seen which are distributed randomly throughout the specimens at a very small size, and the carbides found in the optical microscopy etching become much darker. When the coiling temperature becomes 450°C, more M/A islands can be found, and the particles become relatively coarser. A statistical results of the volume fraction and maximum size of M/A islands were listed in Table 5.1. The definition of the

maximum size is an average size of the largest 10% of M/A islands in the microstructures shown in Figures 5.7 to 5.9.

Figure 5.11 shows the SEM micrographs of martensite/austenite (M/A) constituents in the steels with different coiling temperatures at higher magnifications. For steels with a coiling temperature of 610°C, just a few M/A particles can be seen on the grain boundaries. As the coiling temperatures get lower, as described in the last paragraph, more and coarser M/A islands can be observed which suggests that the isothermal holding or slow cooling (simulation of coiling) has been insufficient to achieve the complete of transformation of the resultant phases.

Overall, the difference in the finish rolling temperature did not have an obvious influence on the microstructures. However, the variation in coiling temperature changes the microstructure obviously. As the coiling temperature decreases from 610°C to 450°C, a shift is observed from high coiling temperature phases such as polygonal ferrite or more equiaxed quasi-polygonal ferrite grains to lower coiling temperature phases, such as coarser quasi-polygonal ferrite, granular bainite and upper bainite. Carbides become segregated, more and coarser M/A islands can be found.

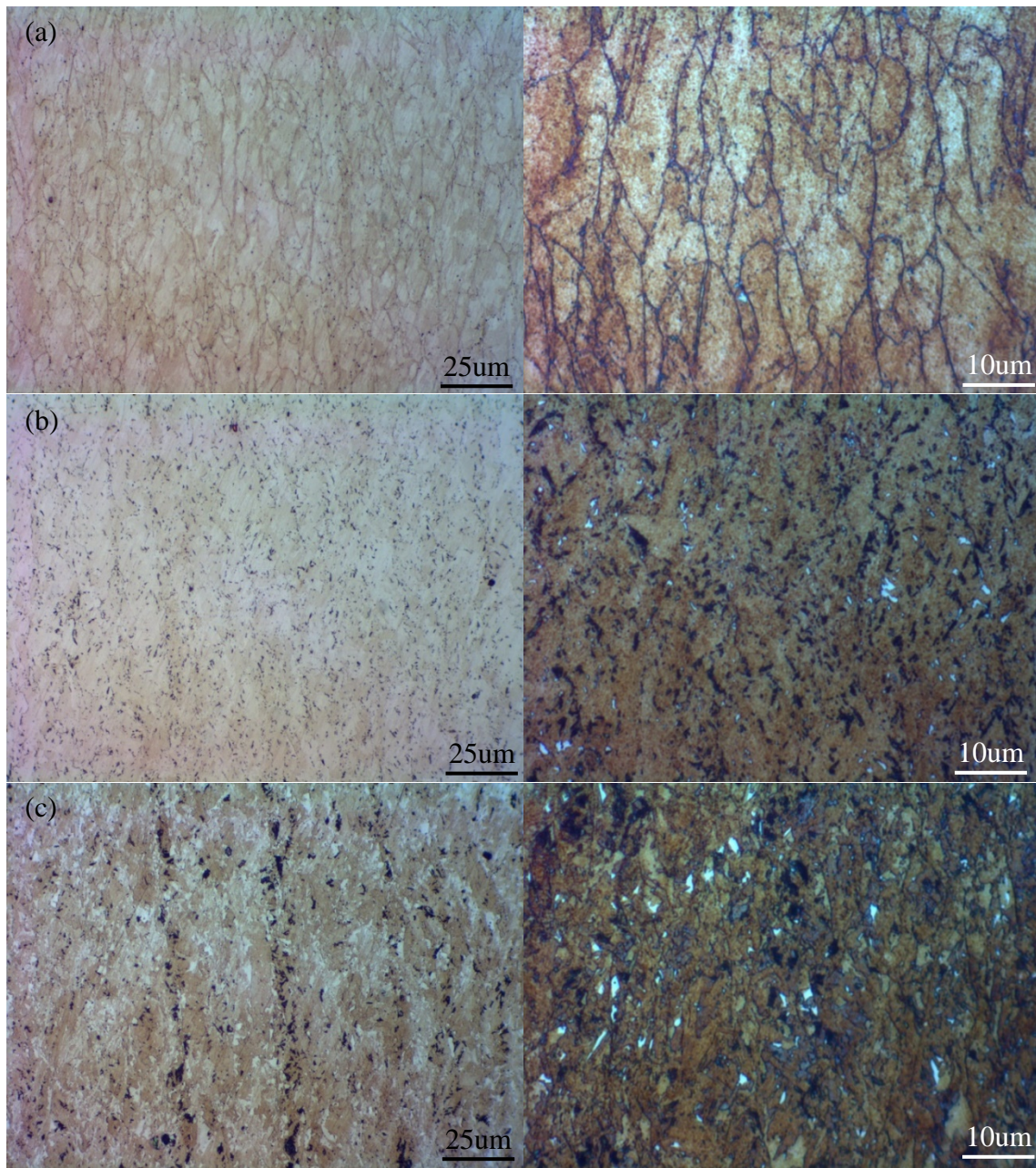


Figure 5.7: Optical microstructure of steels at finish rolling temperature of 870°C with coiling temperatures of (a) 610°C; (b) 530°C; (c) 450°C

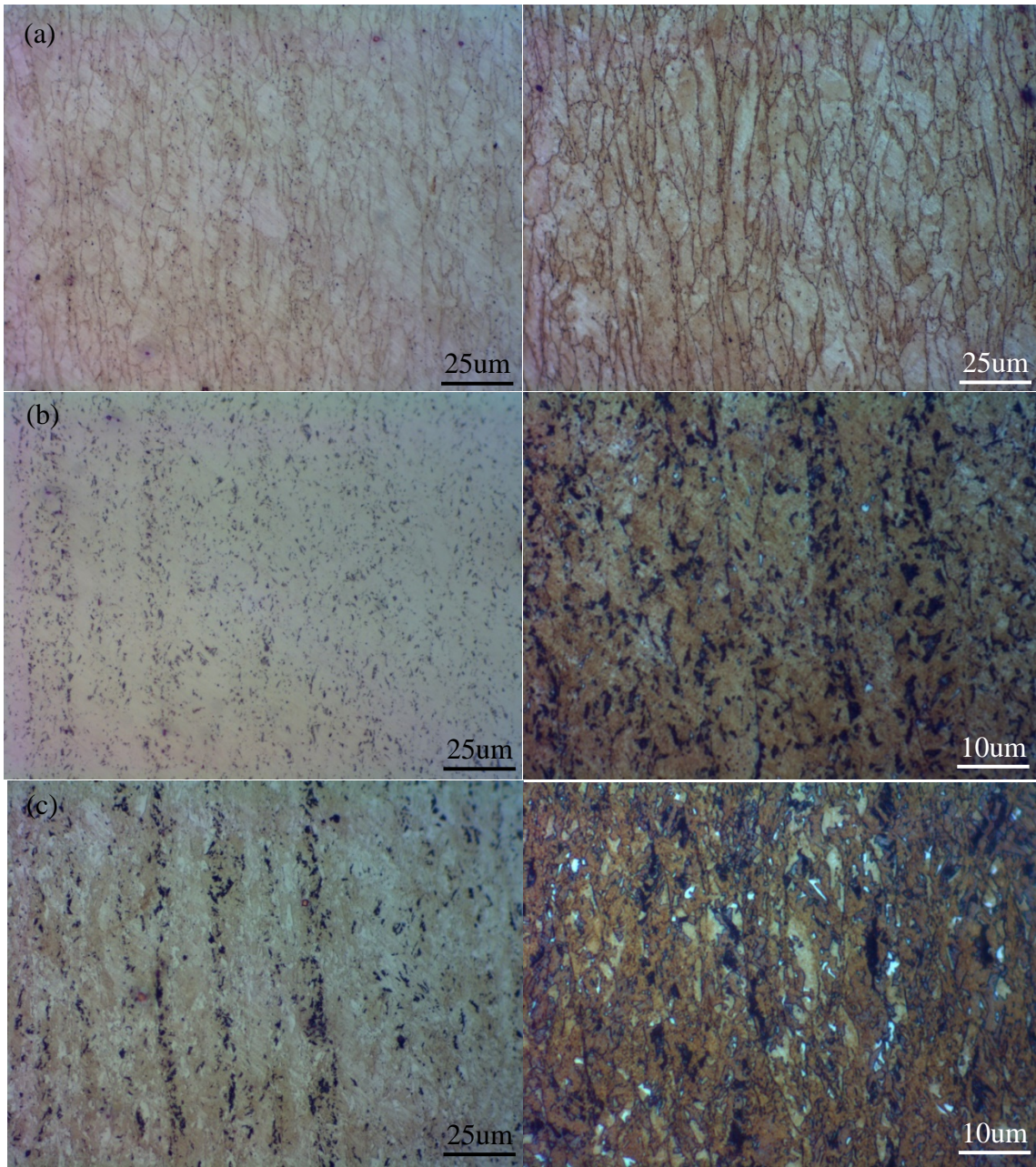


Figure 5.8: Optical Microstructure of steels at finish rolling temperature of 810°C with coiling temperatures of (a) 610°C; (b) 530°C; (c) 450°C

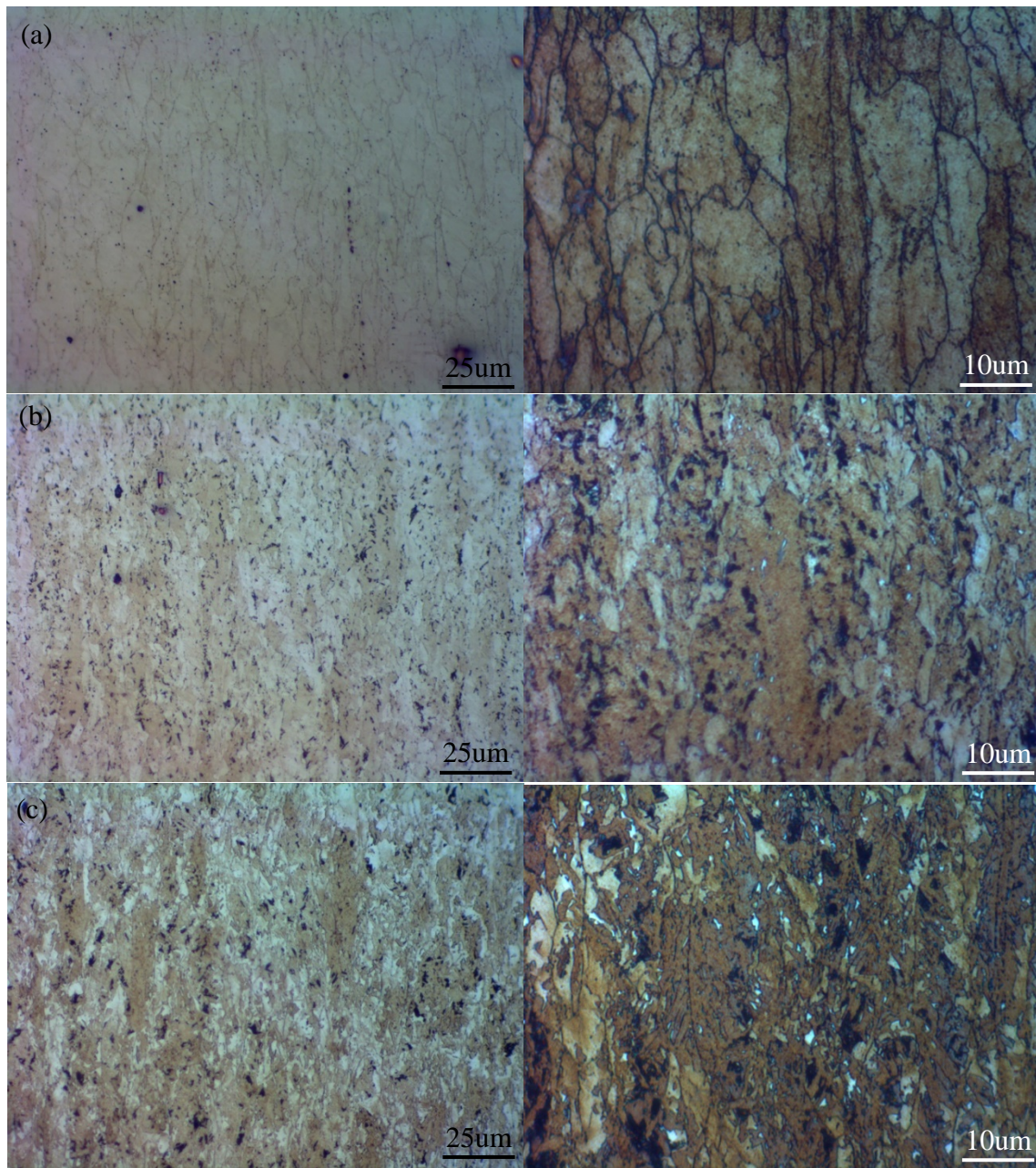


Figure 5.9: Optical Microstructure of steels at finish rolling temperature of 750°C with coiling temperatures of (a) 610°C; (b) 530°C; (c) 450°C

Table 5.1: Volume fraction and average size of M/A constituents

| ID | PG11 | PG12 | PG13 | PG21 | PG22 | PG23 | PG31 | PG32 | PG33 |
|------------------|------|-------|--------|------|--------|--------|------|--------|--------|
| f _v | 0 | 1.1% | 1.9% | 0 | 0.4% | 1.3% | 0 | 0.4% | 1.8% |
| d _{max} | N/A | 1.2um | 1.6 um | N/A | 0.9 um | 1.4 um | N/A | 0.9 um | 1.5 um |

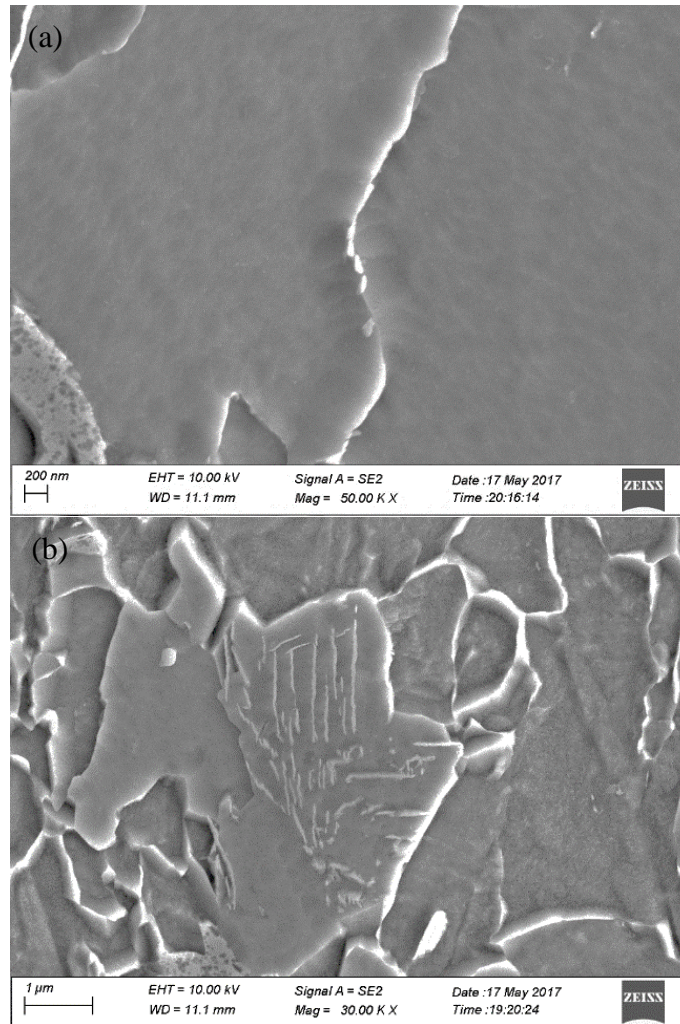


Figure 5.10: Morphology of carbide of steels with coiling temperature of (a) 530°C; (b) 450°C

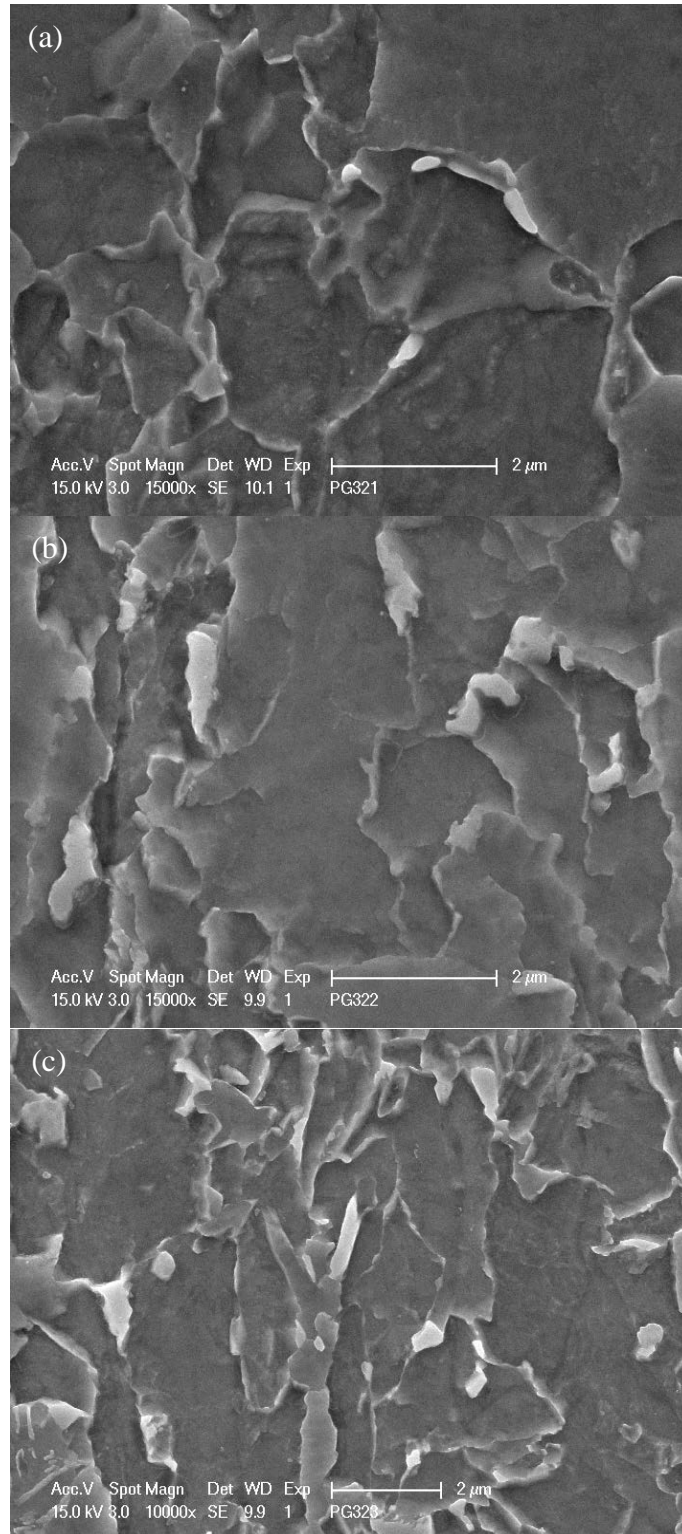


Figure 5.11: Observation of M/A in the steels with cooling temperature of (a) 610°C; (b) 530°C; (c) 450°C

During the metallurgical observation, many inclusions can be observed. As Figure 5.12 shows, in the bright field OM, inclusions appear throughout the specimens, at these magnifications, two sizes of inclusions can be noticed. In order to get more accurate information about the inclusions, SEM observation was applied, and the results are shown in Figure 5.13 and 5.14. It can be seen that second phase particles can be easily found within the grains, with a size ranging from several microns to about several hundreds of nanometers. With the assistance of EDAX, those smaller particles can be identified as (Ti, Mo, V)C, at a size of about 300nm and with a spherical shape, while the bigger ones are TiN at a size of several microns with the typical cuboidal shape.

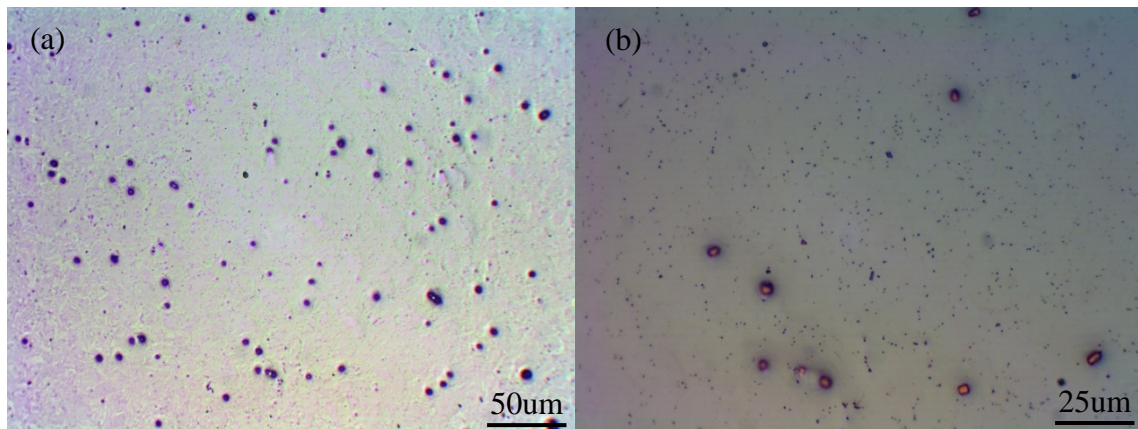


Figure 5.12: Observation of inclusions on the surface of an as polished specimen

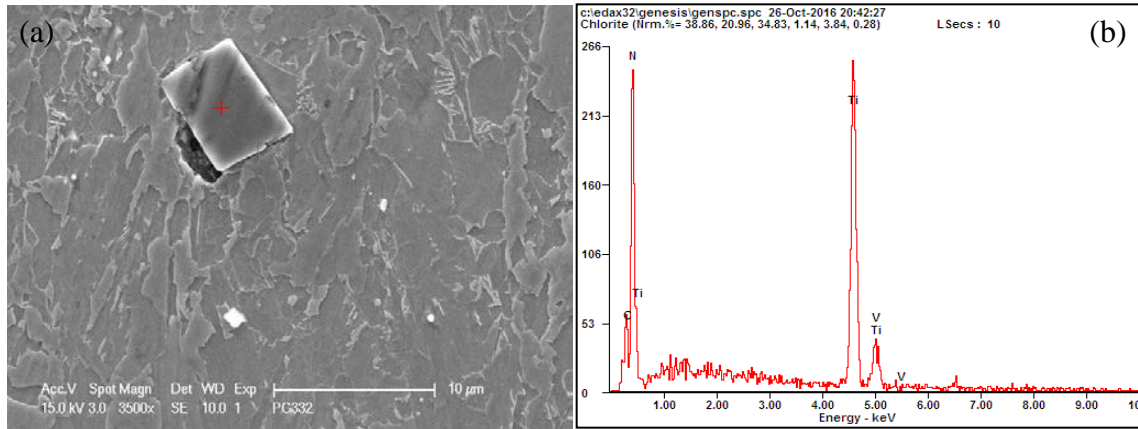


Figure 5.13: SEM/EDAX results of coarse inclusions

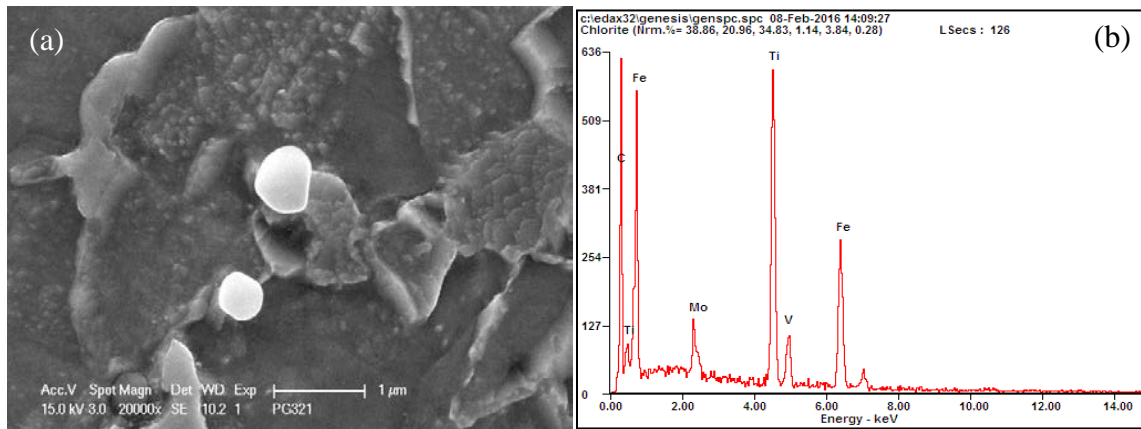


Figure 5.14: SEM/EDAX results of fine inclusions

From previous results, it is known that the microstructure varies between conditions with different coiling temperatures, which might cause different characteristics in the grain boundaries distribution. In this study, EBSD was applied to investigate the distribution in misorientations of grain boundaries. Figure 5.15 is the grain boundary characterization distribution (GBCD) of all the steels conditions from EBSD. From those figures, blue represents the random high angle grain boundaries (HAGB), black represents the low angle grain boundaries (LAGB), and red represents the special grain boundaries (CSL) from $\Sigma 3$ to 29, because CSL boundaries lower than 3 were regarded as LAGB, and random HAGB were when CSL boundaries were higher than $\Sigma 29$. It

seems that the finish rolling temperature also did not have obvious influence on the GBCD, the accumulation bars look similar between each finish rolling temperature. All the steels with a coiling temperature of 610°C exhibited grain boundaries consisting of 65% HAGB, 10% CSL and 25% LAGB, while the steels with a coiling temperature of 530°C had grain boundaries comprised of 38% HAGB, 8% CSL and 54% LAGB. With a coiling temperature of 450°C, the specimens had a similar grain boundaries distribution, with perhaps a little higher percentage in the LAGB and lower percentage in the HAGB. However, the percentage of CSL grain boundaries is the same as found in the intermediate finish rolling temperature. From here, it is obvious that it is the coiling temperature that influences the grain boundaries distribution. The lower coiling temperatures bring about more LAGB, the CSL grain boundaries fraction stays constant. The reason and effects of the GBCD will be discussed later in the discussion part.

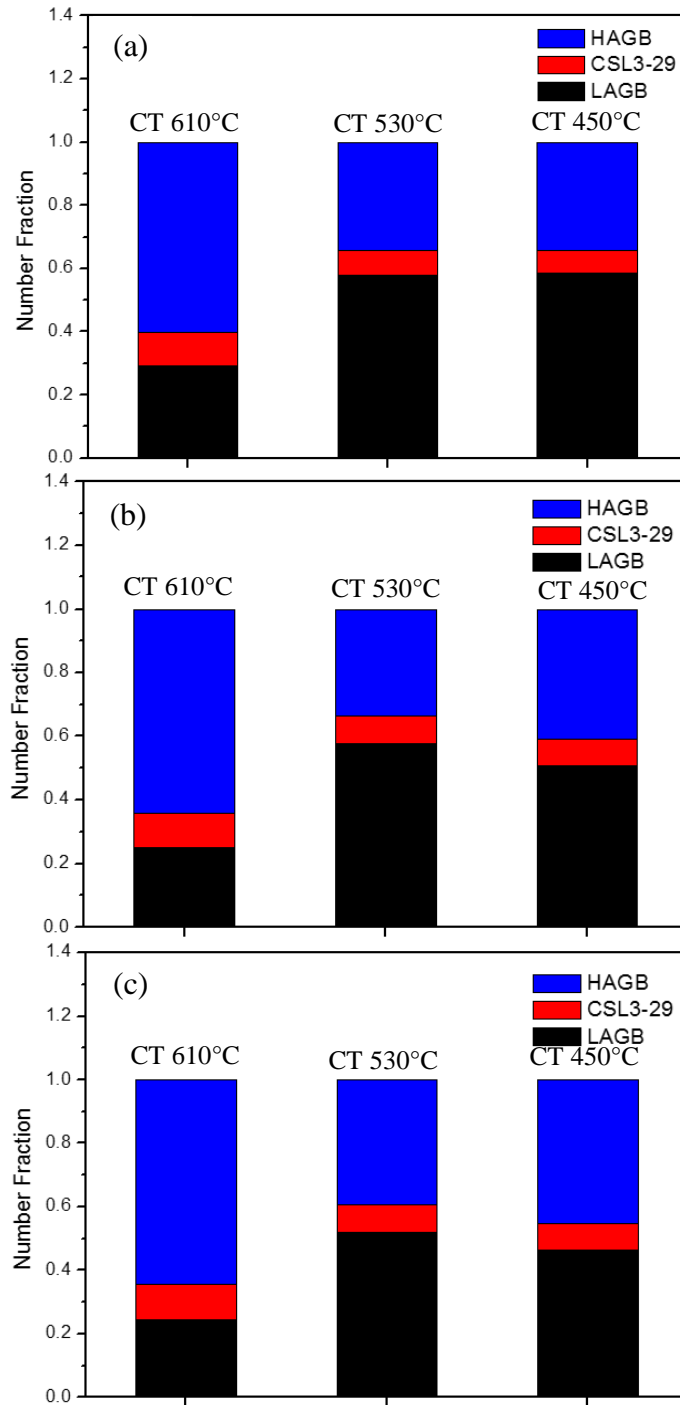


Figure 5.15: GBCD of steels with finish rolling temperature of (a) 870°C; (b) 810°C; (c) 750°C

5.2 MECHANICAL PROPERTIES OF THE HOT BANDS

5.2.1 Hardness test

After the examination of the microstructure of the hot bands, multiple mechanical tests were applied to evaluate the properties of the various steel conditions. Vicker's hardness was employed to test the universal hardness of the specimens with a load of 300gf and a 10s dwell time, and the results are listed in the Table 5.1.

Table 5.2: Vicker's hardness of steel conditions, VHN(300gf)

| ID | PG11 | PG12 | PG13 | PG21 | PG22 | PG23 | PG31 | PG32 | PG33 |
|------------|-------|------|-------|-------|------|-------|-------|-------|-------|
| VHN(300gf) | 422.5 | 307 | 360.4 | 414.5 | 300 | 349.1 | 426.4 | 317.8 | 349.3 |

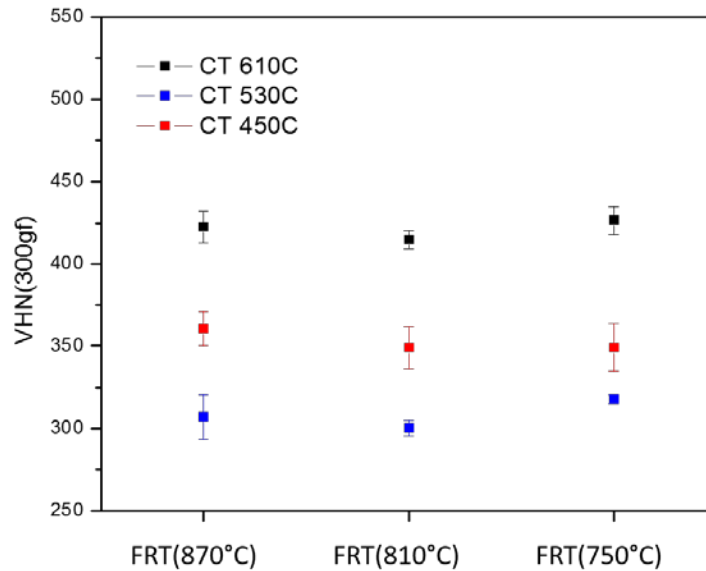


Figure 5.16: Vicker's hardness number of steel condition

As Figure 5.16 shows, specimens with a coiling temperature of 610°C have VHN around 425, and steels with a coiling temperature of 530°C have VHN around 350, and for steels with a

coiling temperature of 450°C, the VHN is around 300. The difference is quite obvious that the hardness of the steels reaches maximum value at coiling temperature of 610°C, and drops to its minimum value at coiling temperature of 530°C, while at the coiling temperature of 450°C, the hardness of the specimens has an intermediate value. This is a quite unusual behavior, as the strength or hardness normally increases with lower coiling temperatures^[21].

5.2.2 Tensile test

Tensile tests were conducted at room temperature with a sub-size specimen whose length is parallel to the rolling direction. The results are listed in Table 5.2. From this table, it can be seen that the tensile strength of the hot band steels ranges from 939 MPa to 1225 MPa, while the yield strength ranges from 811 MPa to 1166 MPa. The total elongation values of the hot band steels are relatively constant, range from 17% to 20%, it seems that the steels with higher strength did not sacrifice their ductility. This is a very important point. The yield ratio of the steels was also listed in this table. It seems that the yield ratio value is quite high for the hot bands, ranging from 0.86 to 0.95. This is a good indication that simple polygonal ferrite is not the predominant phase present in any of the conditions, especially the ones with 610°C coiling temperature, where polygonal ferrite would be most likely expected. The engineering stress-strain curves are shown in Figure 5.17. It can be seen that all the steels with each finish rolling temperature have a similar tensile behavior, with its group of coiling temperatures.

Table 5.3: Tensile properties of the steels

| ID | Off.YS (MPa) | UTS (MPa) | UEL (%) | TEL (%) | Yield Ratio |
|------|--------------|-----------|---------|---------|-------------|
| PG11 | 1166 | 1225 | 9.9 | 19.2 | 0.95 |
| PG12 | 811 | 939 | 8.8 | 17.1 | 0.86 |
| PG13 | 923 | 1062 | 9.7 | 19.7 | 0.87 |
| PG21 | 1135 | 1194 | 10.4 | 19.6 | 0.95 |
| PG22 | 834 | 949 | 8.4 | 18.0 | 0.88 |
| PG23 | 937 | 1066 | 9.7 | 18.5 | 0.88 |
| PG31 | 1095 | 1165 | 10.4 | 20.6 | 0.94 |
| PG32 | 886 | 997 | 10.2 | 19.8 | 0.89 |
| PG33 | 974 | 1091 | 10.0 | 19.2 | 0.89 |

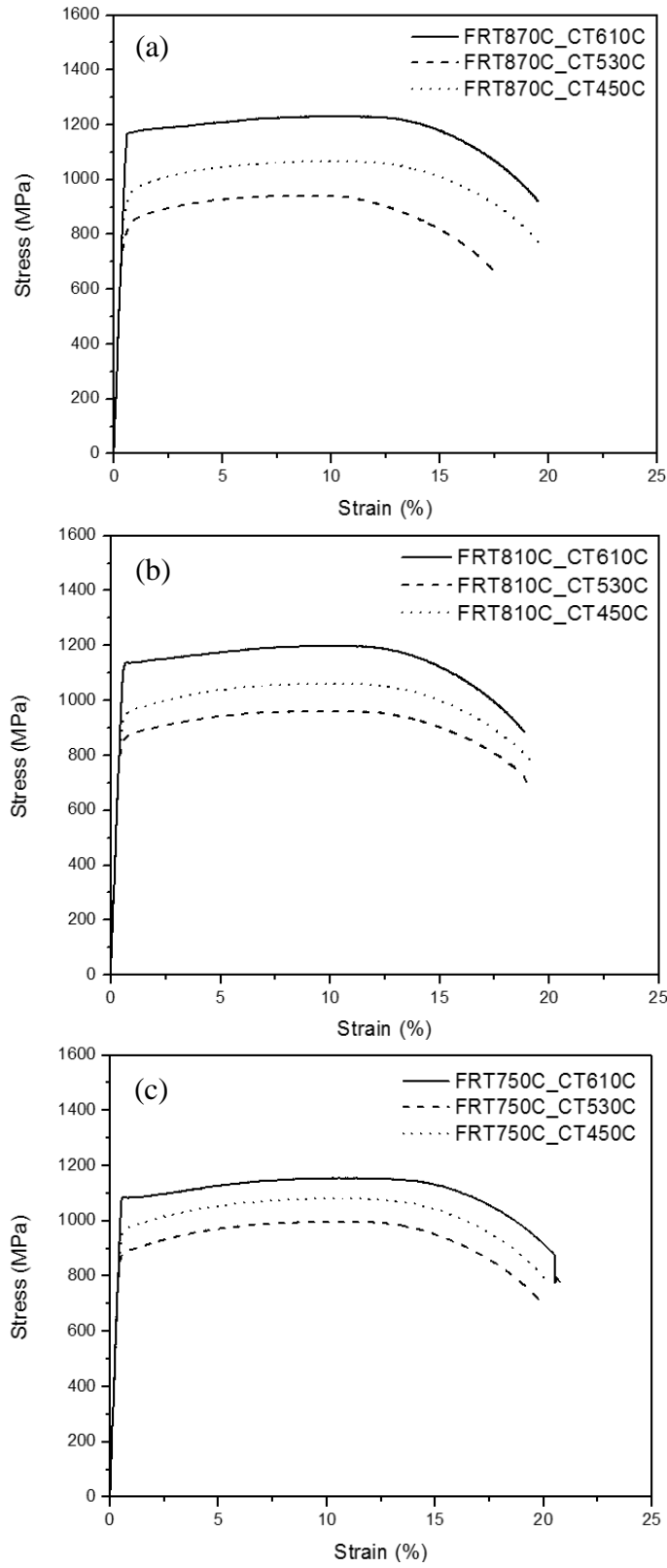


Figure 5.17: Engineering strain-stress curve of steels (a) 870°C; (b) 810°C; (c) 750°C

Figure 5.18 is a plot of tensile strength and yield strength from Table 5.2. It can be seen that steels with a coiling temperature of 610°C have the highest strength, then followed by the steels with a coiling temperature of 450°C, whose tensile strength were above 1000MPa, the steels with a coiling temperature of 530°C have the lowest strength which were below 1000MPa. The yield strength of the steels follows the same tendency as the tensile strength. One interesting thing to notice is the gap between the tensile strength and the yield strength in Figure 5.18 or the yield ratio value listed in Table 5.2 above. The yield ratio of the steels with a coiling temperature of 610°C has a very constant and high value which is about 0.95 and for the steels which have lower coiling temperatures, the value decreases to a lower value from 0.86 to 0.89. The high yield ratio value is generally associated with a low working hardening behavior, as a result of high dislocation densities going into the test. This feature is dependent on the processing parameter and the microstructures of the steels, such as the grain size, dislocation density, volume fraction of carbides and solute atoms, and the relationship between them will be discussed in detail later.

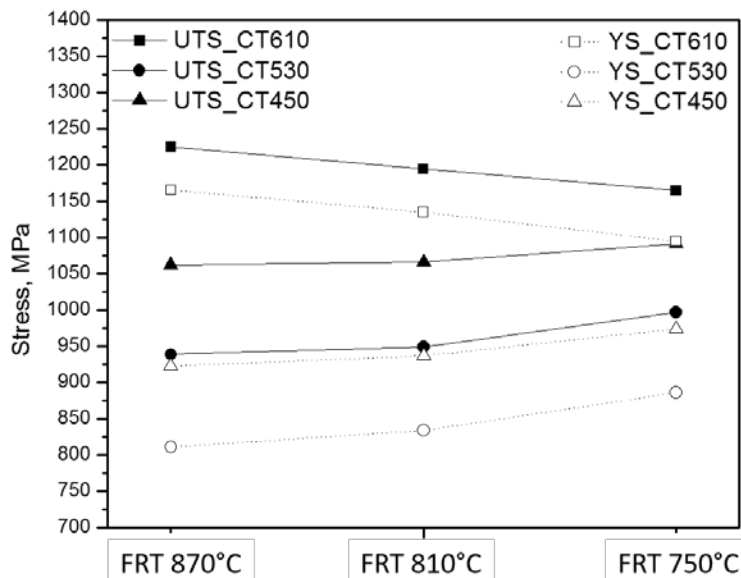


Figure 5.18: Tensile strength of the hot band steels

5.2.3 Charpy V-notch impact test

The Charpy V-notch impact test was conducted at -40°C to evaluate the low temperature toughness of the steels. According to the ASTM, the size of the sub-sized specimens used in this test is $2 \times 10 \times 55\text{mm}$ instead of a standard size of $10 \times 10 \times 55\text{mm}$ with the length along the transverse direction. The results of the Charpy V-notch impact are listed in Table 5.3. The first row is the results read directly from the instrument after the test was done, and the second row is the converted results to the standard full size according to ASTM A370, Table 9^[120].

Table 5.4: Absorbed energy of the Charpy V-notch impact test, J

| ID | PG11 | PG12 | PG13 | PG21 | PG22 | PG23 | PG31 | PG32 | PG33 |
|-----------|------|------|------|------|------|------|------|------|------|
| Tested | 4 | 12 | 7 | 4 | 14 | 11 | 4 | 12 | 7 |
| Full size | 18 | 48 | 27 | 18 | 60 | 41 | 18 | 48 | 27 |

Figure 5.19 shows the results of the absorbed energy at -40°C after full size conversion. Similar to the hardness and tensile properties, the whole results can be divided into three groups with respect to the coiling temperatures. It can be seen that the steels with coiling temperature of 610°C have the worst toughness at -40°C , the energy absorbed at the temperature is 18J during the impact. The steels with a coiling temperature of 530°C have the best results, absorbing around 50J during the impact. And steels with lowest coiling temperature of 450°C have an intermediate toughness, the energy absorbed is ranging from 27J to 41J. Interestingly, excepting the steels with the highest coiling temperature, the steels with lower coiling temperatures seem to absorb the most energy during impact with intermediate finish rolling temperature of 810°C . From Figure 5.20, it can be seen that this result complies with the findings that the toughness usually decreases as the strength increases.

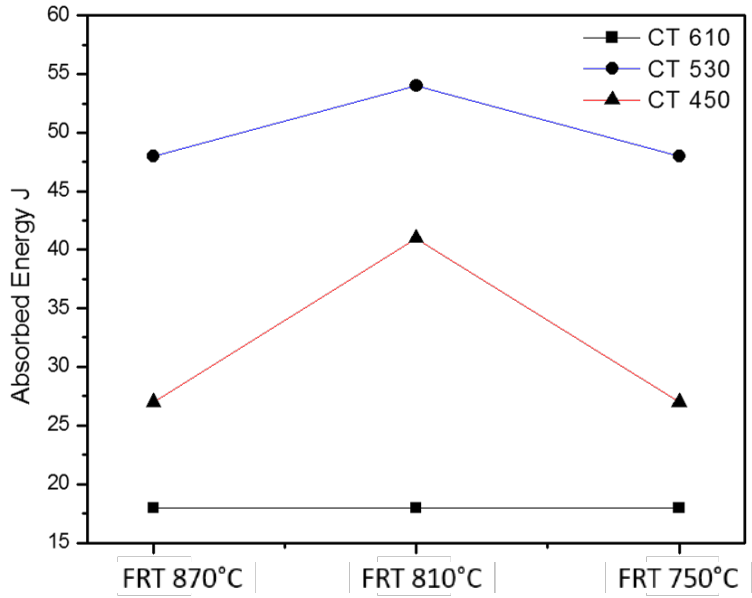


Figure 5.19: Absorbed energy of Charpy impact test result

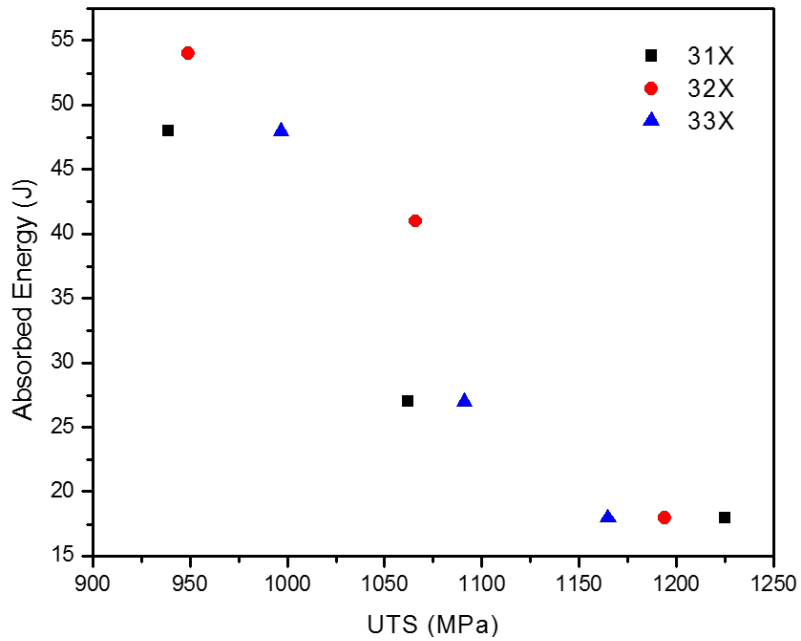


Figure 5.20: Relationship between absorbed energy and tensile strength

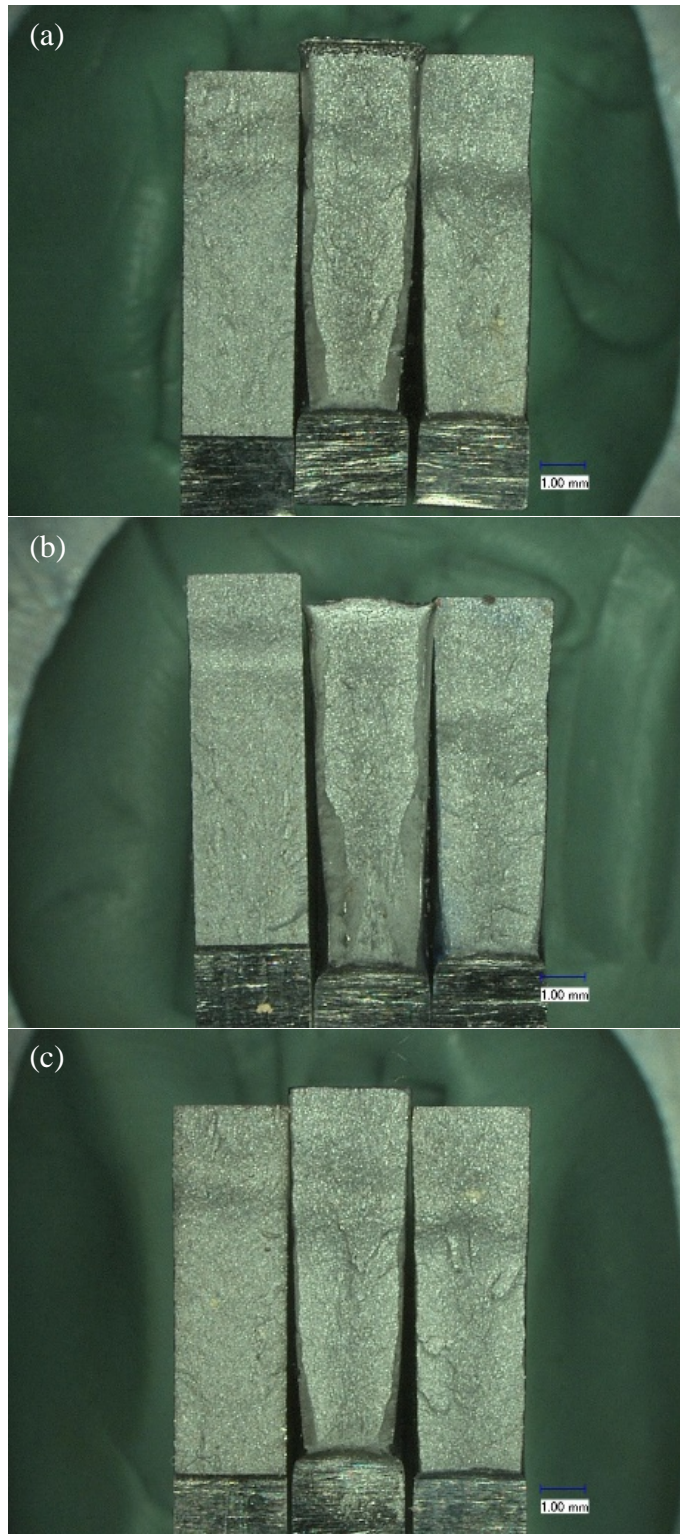


Figure 5.21: Optical micrograph of Charpy V-notch specimens fracture surface with finish rolling temperature of (a) 870°C; (b) 810°C; (c) 750°C. The coiling temperature decreases from left to right

Figure 5.21 is the optical micrograph of the fracture surface of the specimens after the impact test. It can be seen that the fraction of the shear area varies among these specimens, and the results of the shear area percentage are listed in Table 5.4. In the Figures 5.21(a), (b) and (c), the coiling temperature decreases from left to right. From the figure, it can be seen that steels with a coiling temperature of 610°C show a mostly flat fracture surface, indicating almost 0 percentage of shear area. For specimens with a coiling temperature of 530°C, a large amount of ductile fracture area appears, and accordingly, in Table 5.4, those steels have a higher shear area percentage. Moreover, steels with a coiling temperature of 450°C have a little tilted area on both sides edge of the tested specimens, showing a very low percentage of shear area.

Table 5.5: Shear Area Percentage of Fracture Surface

| ID | PG11 | PG12 | PG13 | PG21 | PG22 | PG23 | PG31 | PG32 | PG33 |
|---------------|------|------|------|------|------|------|------|------|------|
| Percentage, % | 1 | 30 | 5 | 0 | 32 | 7 | 0 | 14 | 5 |

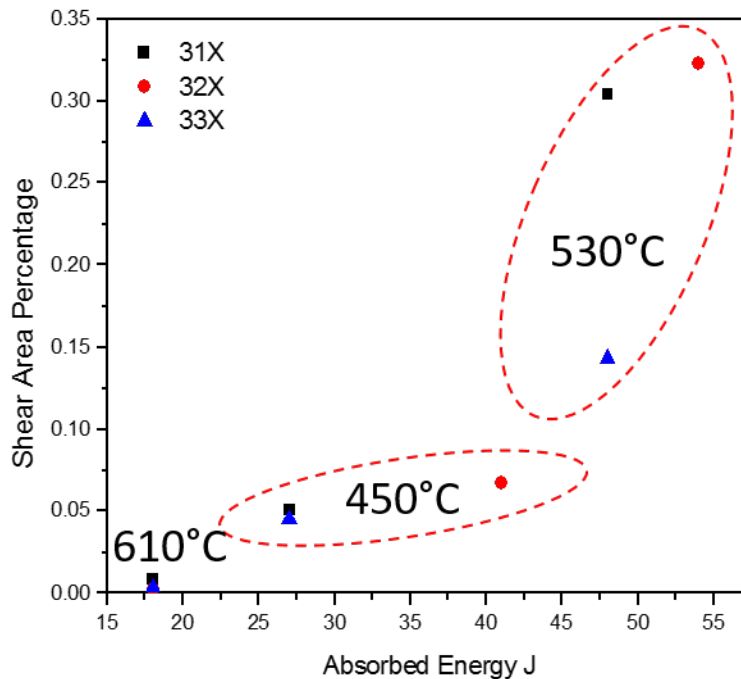


Figure 5.22: Relationship between the shear area percentage and absorbed energy

From Table 5.3 and Table 5.4, it can be seen that the absorbed energy and shear area change together. And the relationship between them is plotted in Figure 5.22. It can be seen that during the impact, steels absorbing more energy ended up with a fracture surface consists of higher fraction of shear area.

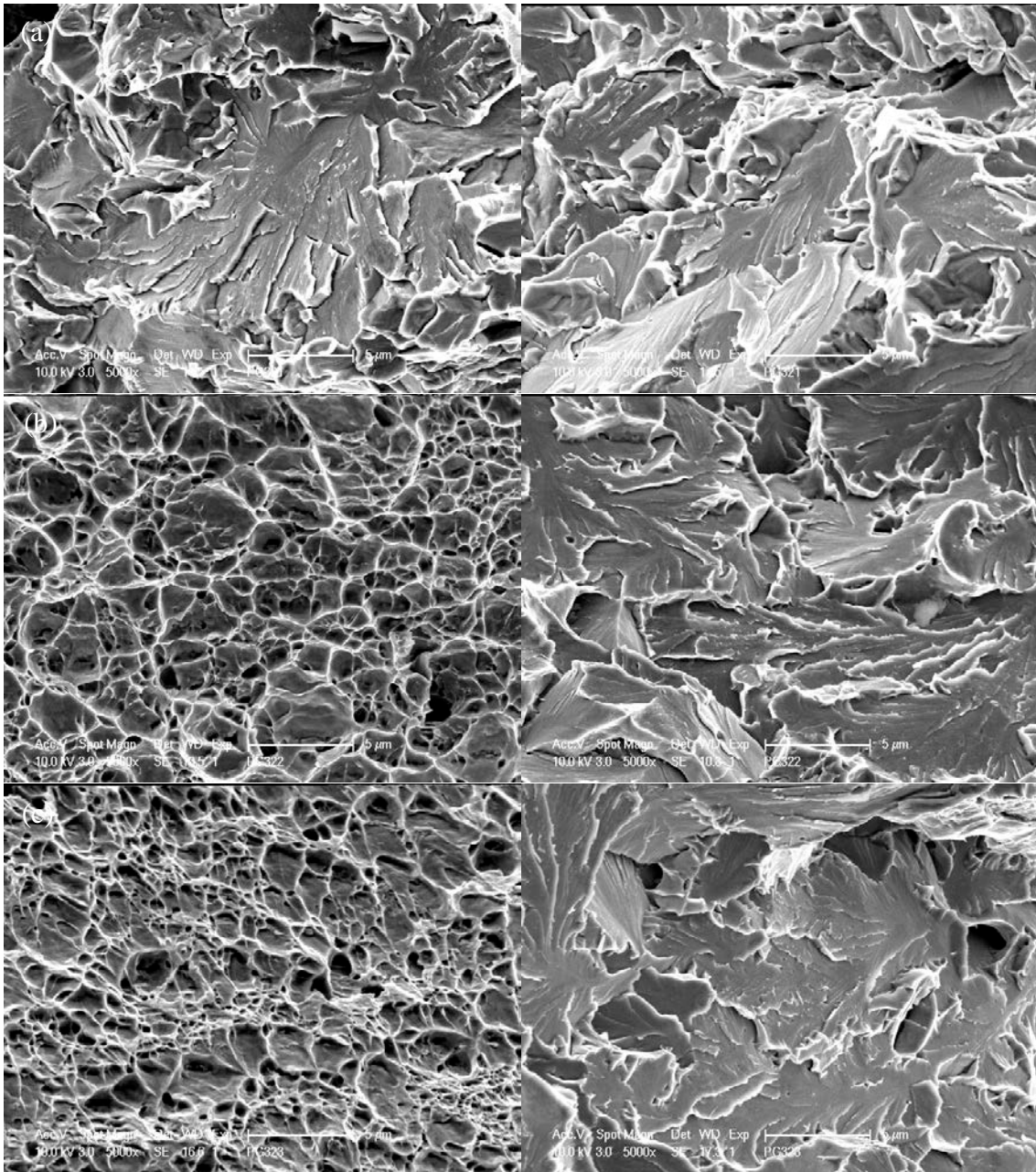


Figure 5.23: SEM micrographs of fracture surface of steels with a coiling temperature of (a) 610°C; (b) 530°C; (c) 450°C

Figure 5.23 shows the SEM micrographs of the impacted test fracture surface at higher magnification. It can confirm the results from the optical observation that the steels with a coiling temperature of 610°C have mostly full brittle fracture surface which were comprised only of cleavage facets, while the fracture surface of steels with lower coiling temperatures consisted of both dimples and cleavages areas, which indicate a mixed surface of ductile and brittle fracture modes. Moreover, from Figure 5.24, it can be seen that on these cleavages facets, large TiN particles can be found with a size that can reach to 5 microns. These large, hard particles can raise stress concentration in the vicinity of this area, and can nucleate cleavage cracking^[121]. Therefore, during the impact test, those areas can be teared apart more easily.

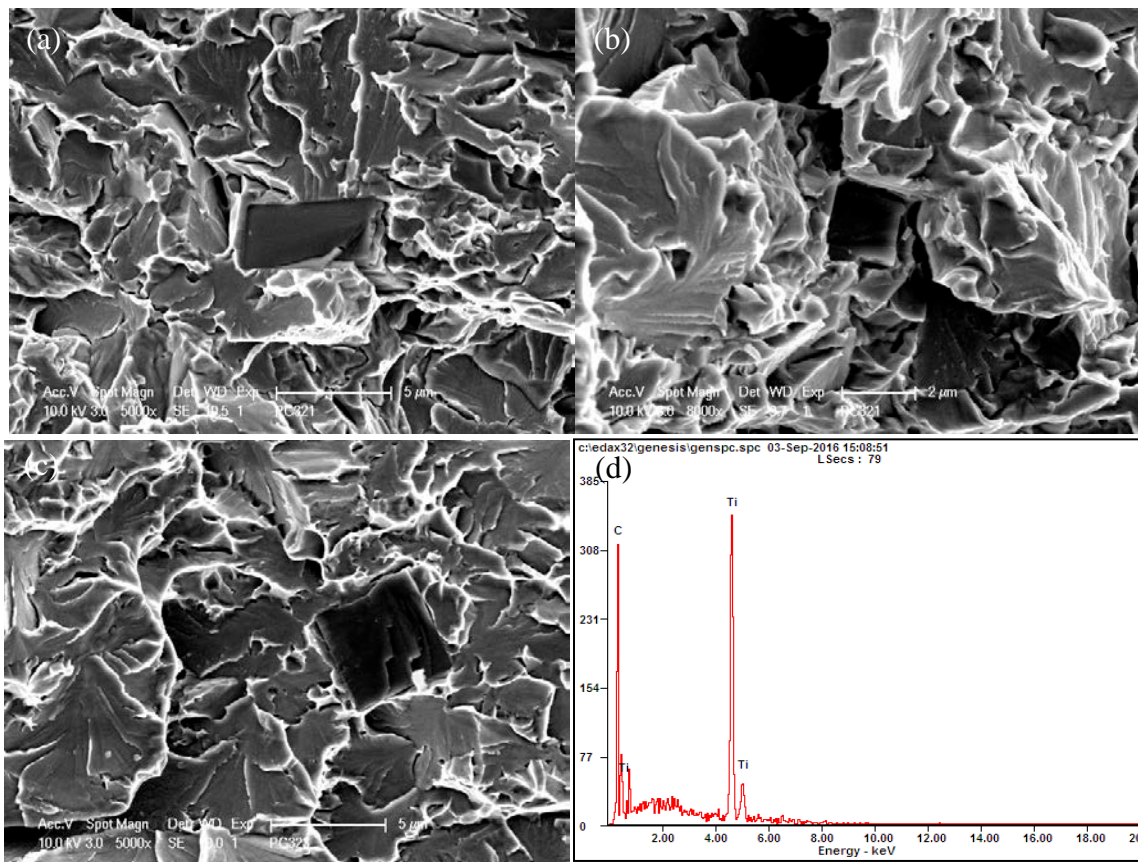


Figure 5.24: Observation of TiN on the fracture surface of Charpy specimens

5.2.4 Hole Expansion Test

The hole expansion test was conducted at room temperature with a punch speed at 0.3mm/s. The results, expressed as hole expansion ratio (HER %) are listed in Table 5.5.

Table 5.6: Hole expansion ratio of the hot band steels

| ID | PG11 | PG12 | PG13 | PG21 | PG22 | PG23 | PG31 | PG32 | PG33 |
|--------|------|------|------|------|------|------|------|------|------|
| HER, % | 0 | 30 | 5 | 0 | 32 | 7 | 0 | 14 | 5 |

From this table, it can be noticed that the HER value has a similar trend as the toughness values from the Charpy impact test. The conditions with the same coiling temperature show similar hole expanding features. During the test, all the hole expansion specimens with a coiling temperature of 610°C did not show the usual through thickness cracking, which defines the end of the test. In this case, the hole did not expand much, but rather the entire sheet cracked. Actually, the test was stopped once a severe crack was formed on the surface of the tested piece. For the steels with lower coiling temperatures, the test was manually stopped once a through thickness crack was observed through a microscope installed above the specimen. From this table, it can be seen that the punched holes of the steels with a coiling temperature of 530°C have a better hole expanding performance than the punched holes from steels with a coiling temperature of 450°C.

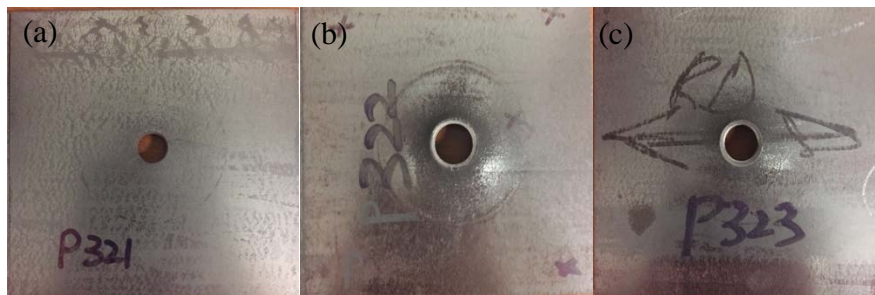


Figure 5.25:Optical micrograph of hole expansion specimens with a coiling temperature of (a) 610°C; (b) 530°C; (c)

450°C



Figure 5.26: Higher magnification of the crack on the surface of steel with a coiling temperature of 610°C. Note the long surface crack with little hole expansion.

Figure 5.25 shows the pictures of specimens with variations in coiling temperatures at one finish rolling temperature of 810°C after the hole expansion test. Obviously, it shows huge differences in the diameter of the punched holes after the test. One noticeable thing is the steels with a coiling temperature of 610°C shown in Figure 5.25(a) and Figure 5.26, are the two cracks that originated from the edge of the punched hole during the test, which means the steels shattered after the cone die was pushing upward from the bottom of the steel plate when reached a force that the plate could not accommodate. Furthermore, the punched hole did not expand at all before this cracking occurred. Other specimens with the same coiling temperature all had the same result. The cause will be discussed in detail in the discussion part.

6.0 DISCUSSION

6.1 THE EFFECTS OF THERMOMECHANICAL PROCESSING PARAMETERS ON THE MICROSTRUCTURE

6.1.1 The effect of the finish rolling temperature on the microstructure

In general, the rolling in the austenite recrystallization region will bring about fine and recrystallized austenite grains^[122], while rolling in the non-recrystallized region will introduce pancaked grains, more grain boundary area per unit volume, a high density of dislocations and substructures in the austenite^[123]. During the continuous cooling to the coiling temperatures, the deformed austenite grains will transform in to one or more different forms of ferrite grains, and the retained austenite region will be further enriched with carbon which is rejected from the ferrite phase and become stabilized^[61]. This carbon enriched austenite will, depending on cooling conditions, transform to martensite and/or retained austenite (M/A) in the final cooling^[124, 125]. Numerous studies have shown that the finish rolling temperature can have an important influence on the ferrite grain refinement, precipitation and dislocation substructures^[126]. In this study, all the steel conditions have the similar roughing and finishing reduction process, the only difference is the finish rolling temperature. Figure 6.1 shows the prior austenite grain boundaries of steels at different finish rolling temperatures. After measuring the prior austenite grain size (PAGS), the

steel with a finish rolling temperature of 870°C has 16.2µm PAGS, the steel with a finish rolling temperature of 810°C has 16.4µm PAGS and the steel with a finish rolling temperature of 750°C has a PAGS of 13.2µm. The prior austenite grains from two higher finish rolling temperatures have very similar grain size while being finish rolled at 750°C, the PAGS is a little smaller. Overall, those prior austenite grain were very small and similar in size.

It can be noticed that all the prior austenite grains remained elongated, which means the finish rolling temperature is below the recrystallization temperature. From Figure 2.3, it can be observed that the addition of certain alloying elements, e.g. the microalloying elements Nb, V and Ti, can strongly increase the recrystallization stop temperature. This is especially true in this steel, with a very high concentration of Ti and V. Take V for instance, because V has a higher solubility in austenite, it can be easily dissolve in the solid solution during soaking prior to the hot rolling, the strain induced precipitates can form during the temperature range of hot rolling and retard the process of recrystallization. Those deformed austenitic grains will have a high interfacial area per unit volume (S_v), and those grain boundary and deformation band areas will become the nucleation sites used for the ferritic transformation. In other words, a higher S_v will result in a smaller ferritic grain structure [127-137].

The basic equation for calculating the S_v was derived by Saltykov^[138] and then developed by Smith and Guttman^[139] as a function of the interception point per unit length (P_L), an alternative method is to count the number of intercepts of particles per unit length (N_L), and their relationship is written as:

$$S_v=2P_L=2N_L \text{ (mm}^2\text{/mm}^3\text{)} \quad (6.1)$$

This method is valid for interconnected grains, i.e. prior austenite grain boundaries. However, in the hot rolled steels, especially with deformed microstructures, the orientation

preference should be taken into account when calculating the Sv value. In this study, the Sv of the elongated grains was measured using the following equation^[140]:

$$Sv(GB) = 0.429(N_L)_{\parallel} + 1.571(N_L)_{\perp} \quad (6.2)$$

where $(N_L)_{\parallel}$ and $(N_L)_{\perp}$ are the intercept numbers per unit length along the rolling direction and thickness direction, respectively. And N_L is calculated by:

$$N_L = \frac{N_i}{L/M} \quad (6.3)$$

where N_i is the number of intercepts counted on the field, L is the total test line length and M is the magnification. Figure 6.2 shows an example of counting the interceptions and calculate the Sv in an interest area with contiguous equiaxed grains^[141].

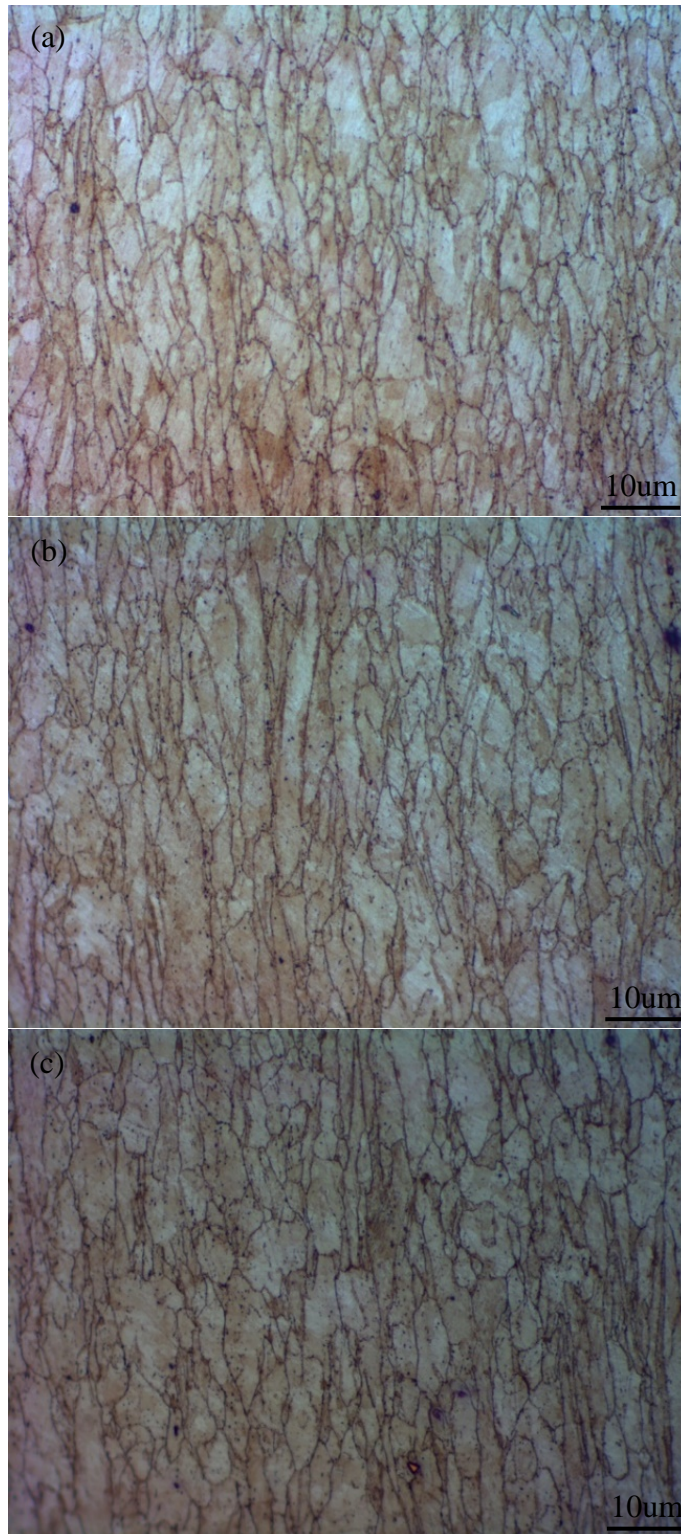


Figure 6.1: Optical microstructure of prior austenite grains with a finish rolling temperature of (a) 870°C; (b) 810°C;
(c) 750°C

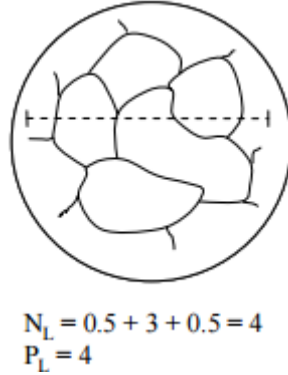


Figure 6.2: Techniques for measuring the SV value in interconnected and discontinuous systems

After counting the intercept number of the prior austenite grains from Figure 6.1, and applying Eq.6.2, the result is shown in Table 6.1. It can be seen that the Sv for steels with a finish rolling temperature of 870°C is 296mm⁻¹, the Sv for steels with a finish rolling temperature of 810°C is 303mm⁻¹ and Sv for steels with a finish rolling temperature of 750°C is 301mm⁻¹. From the calculation, it appears that the Sv did not vary much with different finish rolling temperature, but the Sv values indicate a well-conditioned austenite grains. However, from the interception point number of both directions, it can be noticed that as the finish rolling temperature decreases, the value of (N_L)_{||} decreases, while (N_L)_⊥ increases, which means the prior austenite grains become more elongated, indicating that probably more strain was introduced to the matrix as a result.

Table 6.1: Austenitic GB interfacial area per unit volume (Sv), mm⁻¹

| FRT | 870 | 810 | 750 |
|------------------|-----|-----|-----|
| N _L | 45 | 43 | 37 |
| N _{L⊥} | 176 | 181 | 182 |
| Sv | 296 | 303 | 301 |

It is well known that the prior austenite grain boundaries can be effectively pinned by the small particles formed during solidification and hot rolling. From Figure 6.3^[142], it can be seen that

alloying elements have different effects on the austenite grain size control, especially for Ti. The addition of Ti element can keep the prior austenite grains from coarsening because of the low solubility and good thermal stability of TiN. During hot rolling, Ti first precipitates as nitrides (TiN) and then by carbides (TiC). The effect of hot rolling or TMP parameters on the formation of TiN or TiC will be discussed later.

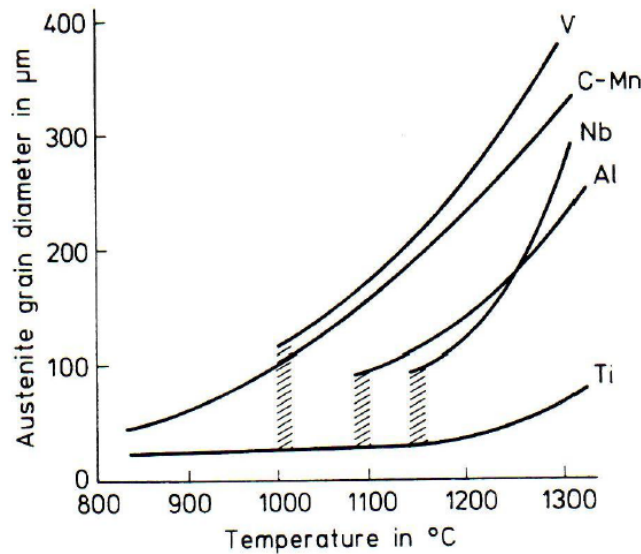


Figure 6.3: The general effect of microalloying additions on the grain coarsening temperature of austenite in C-Mn steels containing a volume fraction of 0.0005 of alloy carbide or nitride

Table 6.2 shows the average grain size from EBSD results. It can be seen that all the steels have very small grains, which is probably due to the nucleation of ferrite grains on the non-recrystallized austenite grains. And the grain size was not so different. Figure 6.4 shows the effect of finish rolling temperature on the grain size area fraction. In general, lower finish rolling temperature will have finer microstructure [125, 143, 144], but in this work, it did not show this relationship. However, the steels with a finish rolling temperature of 810°C always have a higher fraction of fine grains than steels with other finish rolling temperatures.

Table 6.2: Grain Size from EBSD, μm

| CT, °C \ FRT, °C | 870 | 810 | 730 |
|------------------|------|------|------|
| 610 | 2.38 | 2.28 | 2.59 |
| 530 | 2.66 | 2.30 | 2.80 |
| 450 | 2.61 | 2.19 | 2.39 |

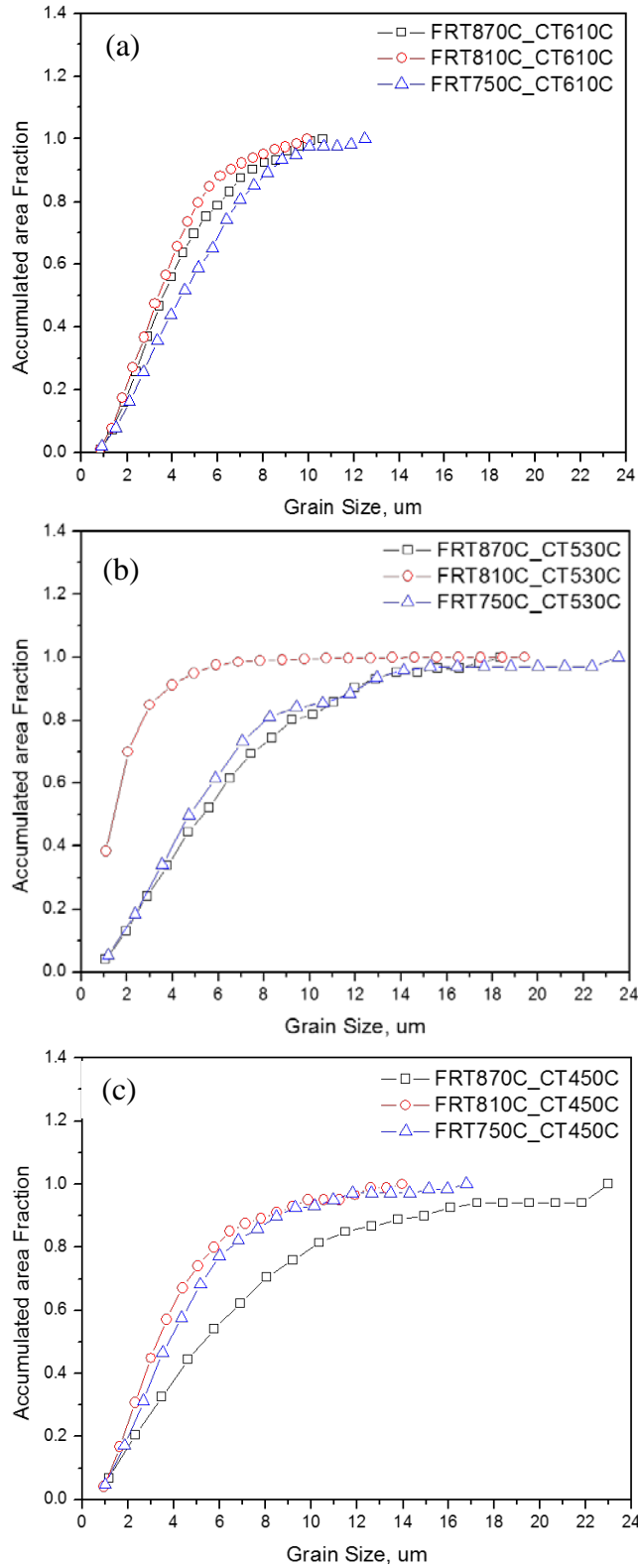


Figure 6.4: Accumulated grain area fraction curve of steels at coiling temperature of (a) 610°C; (b) 530°C; (c) 450°C

6.1.2 The effect of the coiling temperature on the formation of bainite and ferrite

From previous OM and SEM results, it seems that the coiling temperature has a huge influence on the microstructure, which is result from the phase transformation during continuous cooling. At the coiling temperature of 610°C, the matrix is ferrite, and at coiling temperature of 530°C and 450°C, granular bainite and upper bainite start to form. Based on that, it can be seen that the Bs temperature is somewhere between 610°C and 530°C. From Eq.2.4 above:

$$B_s (\text{°C}) = 656 - 57.7C - 75Si - 35Mn - 15.3Ni - 34Cr - 41.2Mo \quad (2.4)$$

it can be calculated that the Bs of this steel chemistry is about 564°C which is just between the two higher coiling temperatures of 610°C and 530°C. Figure 6.5 is the continuous cooling transformation (CCT) diagram run by JMatPro software of this given chemical composition. It shows that the bainite start transformation temperature (Bs) is 607.4°C and martensite start transformation temperature (Ms) is 435.4°C. The result is higher than what was calculated from Eq.2.4, but it is still in the assumed range of Bs temperature. Therefore, any phase transformation that occurred above Bs can resulted in a ferritic microstructure and transformation made under Bs can lead to the formation of a bainitic microstructure. Also, the formation of ferrite can cause the decrease of bainite transformation start temperature. Therefore, the Bs temperature is between the coiling temperature of 610°C and 530°C.

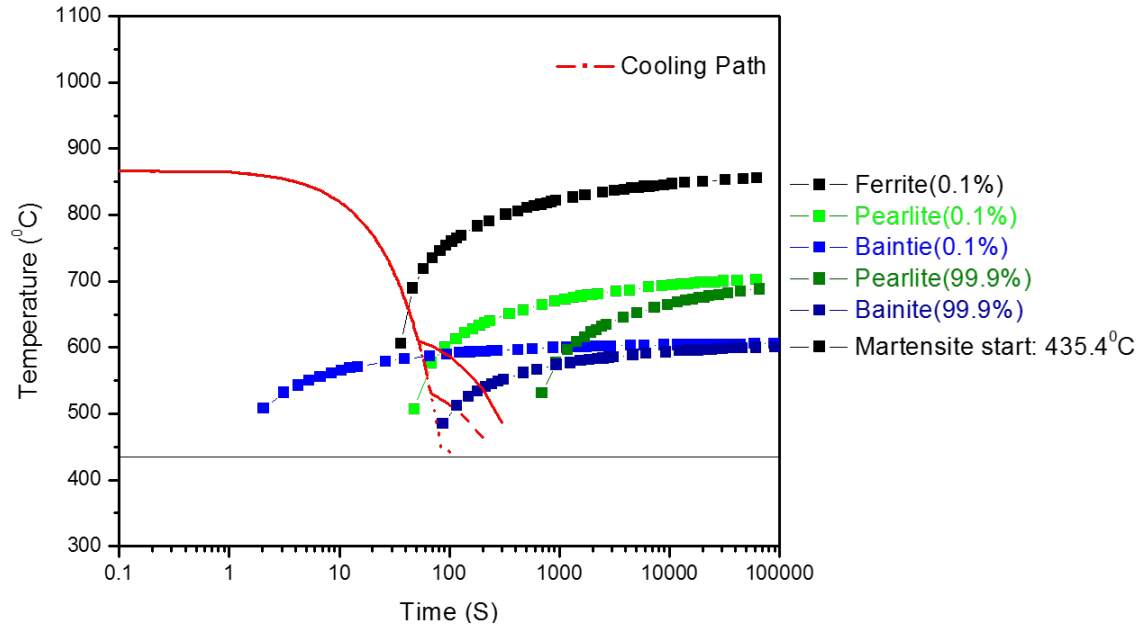


Figure 6.5: Continuous cooling transformation diagram

From Figures 5.1 to 5.3, it is already known that at the coiling temperature of 610°C, the microstructure is polygonal or equiaxed quasi-polygonal ferrite and acicular ferritic grains, and as the coiling temperature goes down to 530°C, coarser quasi-polygonal ferrite and granular bainite could be found. Upper bainitic grains show up at the coiling temperature of 450°C. From B_s temperatures obtained above, either it is 564°C or 607.4°C, and the coiling temperature of 610°C did not cross the B_s line, thus it is expected to have a ferritic microstructure, and during the slow cooling of the simulated coiling process, low temperature ferrite could form. During the lower temperatures of coiling simulation, the temperatures were below the B_s line, bainitic transformation can occur. Moreover, due to the carbides elements (Mo, Ti and V) within the steel, the pearlite transformation could be suppressed. From the coiling temperature of 530°C, which is just below the bainite transformation start temperature, during the slow cooling, ferrite forms by a shear or displacive mode while carbon atoms keep diffusing, once the residual austenite was surrounded by ferrite grains and in the final cooling, those regions can form M/A constituents, thus

resulted in granular bainite. As the coiling temperature dropped down to 450°C , besides the regions which formed granular bainite, some ferrite grains formed in lean carbon regions or near austenite grain boundaries, and cementite can form at the boundaries of ferrite laths, which can be characterized as upper bainite.

From the morphology of ferrite, it can be noticed that besides the appearance of granular bainite and upper bainite, the rest of ferrite grains also show different types. One is the polygonal ferrite which is a fully recovered and recrystallized ferrite formed at high temperature, the other is the quasi-polygonal ferrite or massive ferrite with irregular shape, forms and grows crossing the prior austenite grain boundaries^[145]. The temperature to form quasi-polygonal ferrite is between the polygonal ferrite and bainite^[145-147], and the prefer nucleation sites are the PAGB^[148]. Usually, the austenite and the quasi-polygonal ferrite shares the same chemical composition, the transformation can be accomplished by short range diffusion across the diffusion interface and the partition of the interstitial or substitutional atoms at the interface that can cause the irregular growth of the quasi-polygonal ferrite^[149-151]. Therefore, as the coiling temperature decreases, the quasi-polygonal ferrite becomes more and elongated.

Figures 6.6 to 6.8 are the Image Quality (IQ) Map and Inverse Pole Figure (IPF) Map of all the steels. The black line is the high angle grain boundary ($>15^\circ$) on the identified grains. As the quality of the map is highly related to the lattice defects and surface topology, a reconstructed IQ map will show detailed information about the microstructure such as grain boundary, defect density and different phases. The lighter area shows regions with less distortion and the darker area represents regions with higher distortion. Thus, the grain boundaries on the IQ map are depicted with darker color than in the matrix. And overall, from the IQ maps, the matrix seems to have single phased microstructure.

The Inverse Pole Figure (IPF) describes the position of the specimens coordinate system with reference to the crystal coordinate system. The orientation triangle shown in the IPF indicates the orientation of grains represented by different colors, for instance, the blue means [111] crystal direction, green means [101] crystal direction and crystal red means [001] direction. Grains with no orientation gradient exhibit uniform color while grains with orientation gradient shows color gradient.

It can be seen that from either the IQ map or IPF map, the microstructure of the steels from each coiling temperature look similar. What is noticeable is that the steels from the highest coiling temperature of 610°C are quite different from the steels with lower coiling temperatures. Steels with the highest coiling temperature show uniform and random distribution of grain orientation. And from the shape of the grains depicted by HAGB, it confirms with the results from Nital etched OM or SEM micrographs that the grains in the coiling temperature of 610°C have equiaxed shape. However, for the steels with lower coiling temperatures of 530°C and 450°C, there exists a few coarser elongated grains or coarser blocks with a specific crystallographic orientation along the rolling direction. These are quasi-polygonal ferrite grow from the prior austenite grain boundaries.

Figure 6.9 is the grain boundary misorientation map of the steels. From them, a similar trend can be observed that the steels with a coiling temperature of 610°C have higher fraction of HAGB and lower fraction of LAGB than the steels with lower coiling temperatures, which is the same as GBCD figures. This can be related to the different microstructure they have. For steels with a coiling temperature of 610°C, the dominant phase is the ferrite, and those ferrite grains were separated by HAGB. While for the steels with lower coiling temperatures, the existence of bainite grains can be the cause of the introduction of the LAGB, because the complicated microstructure can bring more sub-structure to the matrix. And the higher percentage of the LAGB can have a big

influence on the mechanical properties. The low angle misorientation units can be related to the strength, while the high angle misorientation units are related to the toughness control. According to Carl^[152-154], boundaries with misorientation between 15° and 45° are associated with ferrite due to the diffusion controlled transformation. Whereas, the misorientations less than 15° or around 60° are the reflection of the displacive formation mechanism of lower temperature transformation product, such as bainite or quasi-polygonal ferrite grain boundaries, which is a good explanation of the appearance of second peak around 60° on the map of the steels with lower coiling temperatures.

Figure 6.10 shows the Kernel Average Misorientation (KAM) maps of all the steel. This result was obtained in the 1st nearest neighbour kernel with a maximum angle of 15°. The color bar on the right corner of Figure 6.10(i) shows the misorientation angle represented by the color, from blue to red, indicating the misorientation angle ranging from 0° to 15°. KAM was proved to be a good tool used to illustrate and investigate the subgrain structure of materials. It clearly shows the difference of subgrain structure in those steels. It shows that the steels with lower coiling temperatures have much higher percentage of the subgrain structure than the steels with a coiling temperature of 610°C. This relationship did not change with different finish rolling temperatures.

Figure 6.11(a) shows a KAM map zoomed in from the red circled area of KAM map from Figure 6.10. It shows the high KAM green substructures with low KAM blue matrix on the background, and the black lines are the HAGBs. On this map, there has three arrows drawn across the grain boundary or subgrain boundary. And the misorientation from point to point on the arrows length is shown in Figure 6.11(b).

From the green arrow curve, it can be seen that when a part of the arrow is in the matrix, the misorientation is quite low, once the line encounters the HAGB, there appears a high peak in the

curve which reaches to about 55° and that is expected to be observed when there is an interaction with a high angle grain boundary, and after the arrow passes the HAGB and enters into another grain matrix, the misorientation value drops again. However, when a arrow encounters the subgrain boundaries, such as black and red arrows, a misorientation peak comes again, but with a value less than 15°. From the figure, depends on the color code of KAM, it seems that the misorientation of the subgrains from black arrow is higher than that from the red arrow, and that is what is observed from the misorientation curve on the right side. The black curve has a peak value of about 14° and the red curve has a peak value of about 6°.

Figure 6.12(a) is an IPF of steels with finish rolling temperature of 750°C and coiling temperature of 530°C, the area with red rectangle is shown in Figure 6.12(b). This coarse grain is a quasi-polygonal ferrite, and from the KAM figure shown in 6.12(c), it is obvious that the quasi-polygonal ferrite has a large amount of substructure within it. From a previous part, it is known that the lower coiling temperatures can result in higher amount of quasi-polygonal ferrite. Therefore, the higher percentage of LAGB from steels with lower coiling temperatures is due to the introduction of the subgrain structures from the bainite or quasi-polygonal ferrite.

According to Kubin and Mortensen^[155], the dislocation density can be determined by using the Kernel Average Misorientation (KAM) from EBSD. The relationship is shown as follows:

$$\rho = \frac{2KAM}{bu} \quad (6.4)$$

where b is the burger's vector and u is the length related to the Kernel. For this purpose, KAM with maximum misorientation 2° and second nearest neighbour is applied to calculate the value. The boundaries with a misorientation angle below 2° are believed to contribute to the dislocation strengthening and those with a misorientation angle larger than 2° are effective to the grain

refinement. According to ISASTI et.al.^[156], an approach has been developed to convert the KAM data from the conventional EBSD result to the data acquired from high resolution EBSD. The conversion equation is shown as follows:

$$\text{HRKAM}(\text{°}) = 1.1 \text{ ConvKAM} - 0.13(\text{°}) \quad (6.5)$$

One group of steels with 810°C finish rolling temperature was chosen to investigate the relationship between the coiling temperature and the dislocation density by using EBSD data. The result of KAM from conventional EBSD data was acquired at higher magnification in order to get a more accurate reading. In this experiment, a hexagonal grid and a step size of 0.1µm was applied, and the raw data converted to high resolution EBSD data are shown in Table 6.3, and the related KAM map is shown in Figure 6.13.

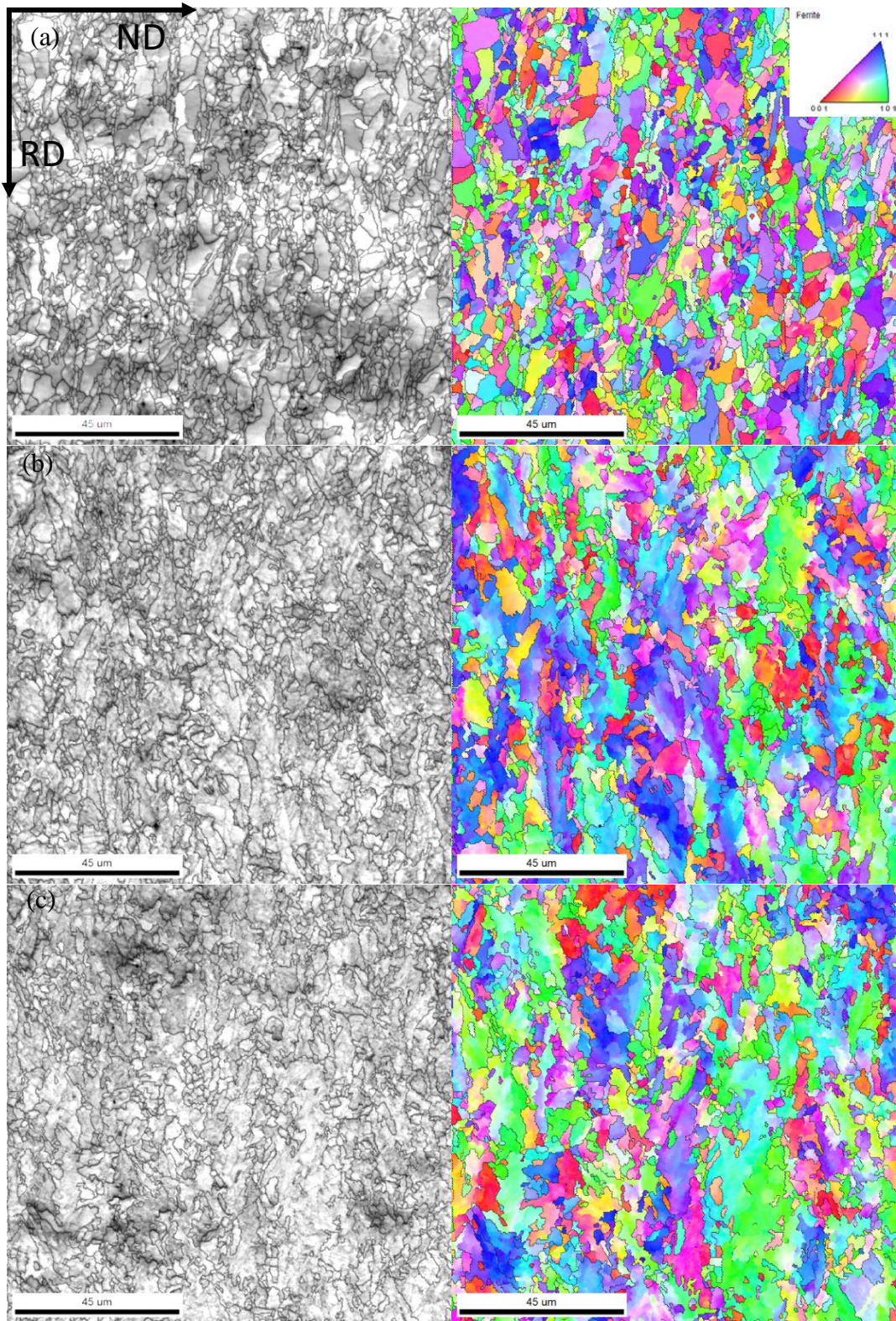


Figure 6.6: Image quality map and inverse pole figures of the steels with a finish rolling temperature of 870°C at a coiling temperature of (a) 610°C; (b) 530°C; (c) 450°C

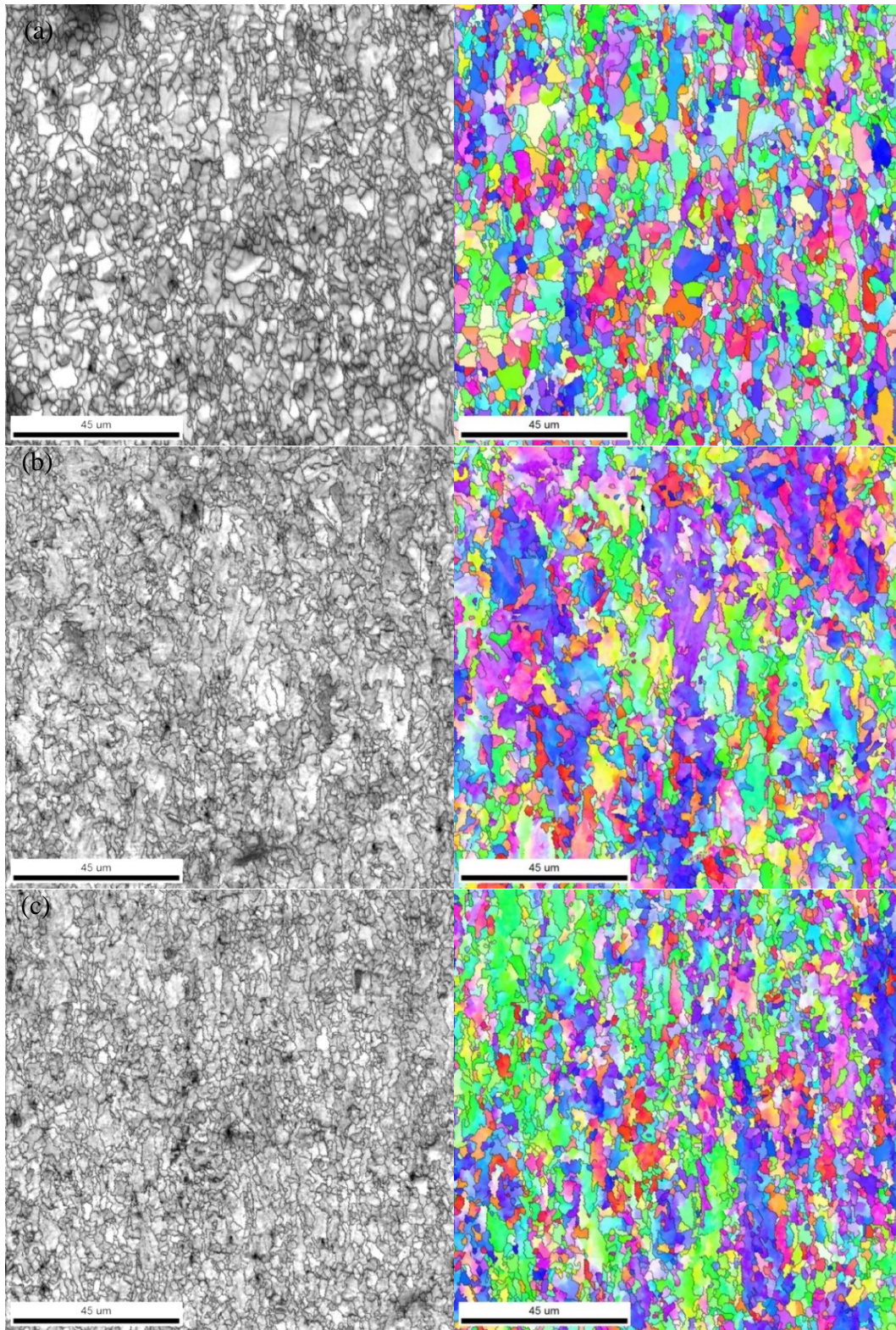


Figure 6.7: Image quality map and inverse pole figures of the steels with a finish rolling temperature of 810°C at a coiling temperature of (a) 610°C; (b) 530°C; (C) 450°C

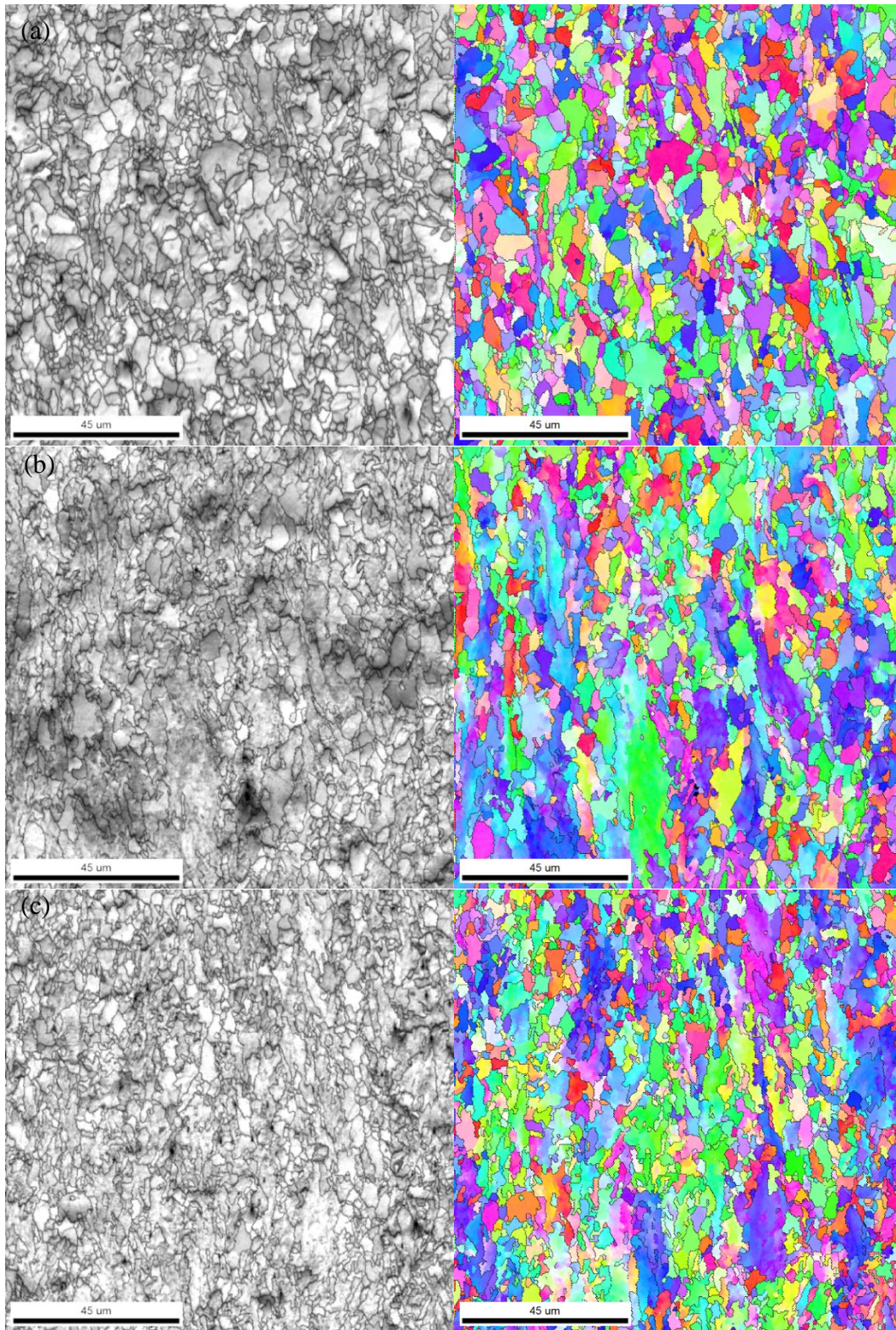


Figure 6.8: Image quality map and inverse pole figures of the steels with a finish rolling temperature of 750°C at a coiling temperature of (a) 610°C; (b) 530°C; (c) 450°C

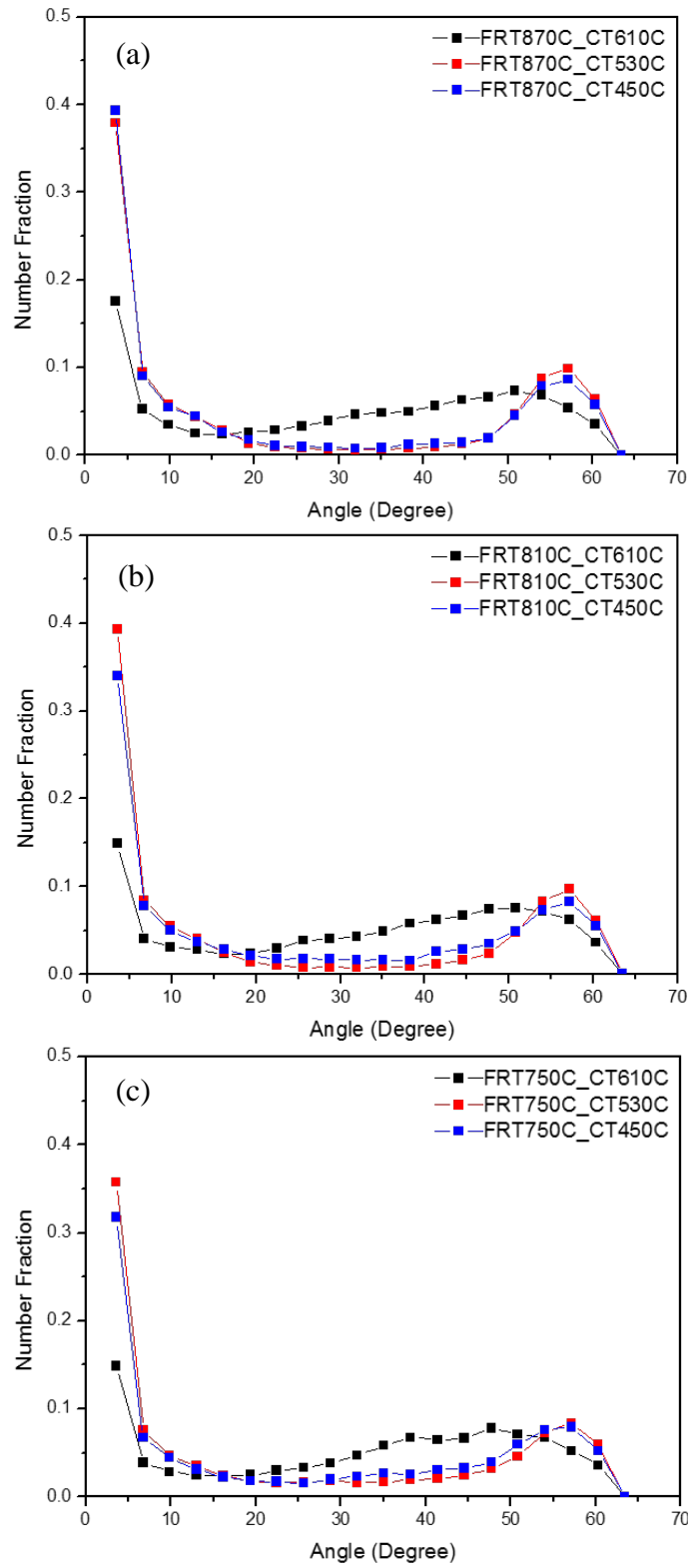


Figure 6.9: Misorientation angle of steels with finish rolling temperature of (a) 870°C; (b) 810°C; (c) 750°C

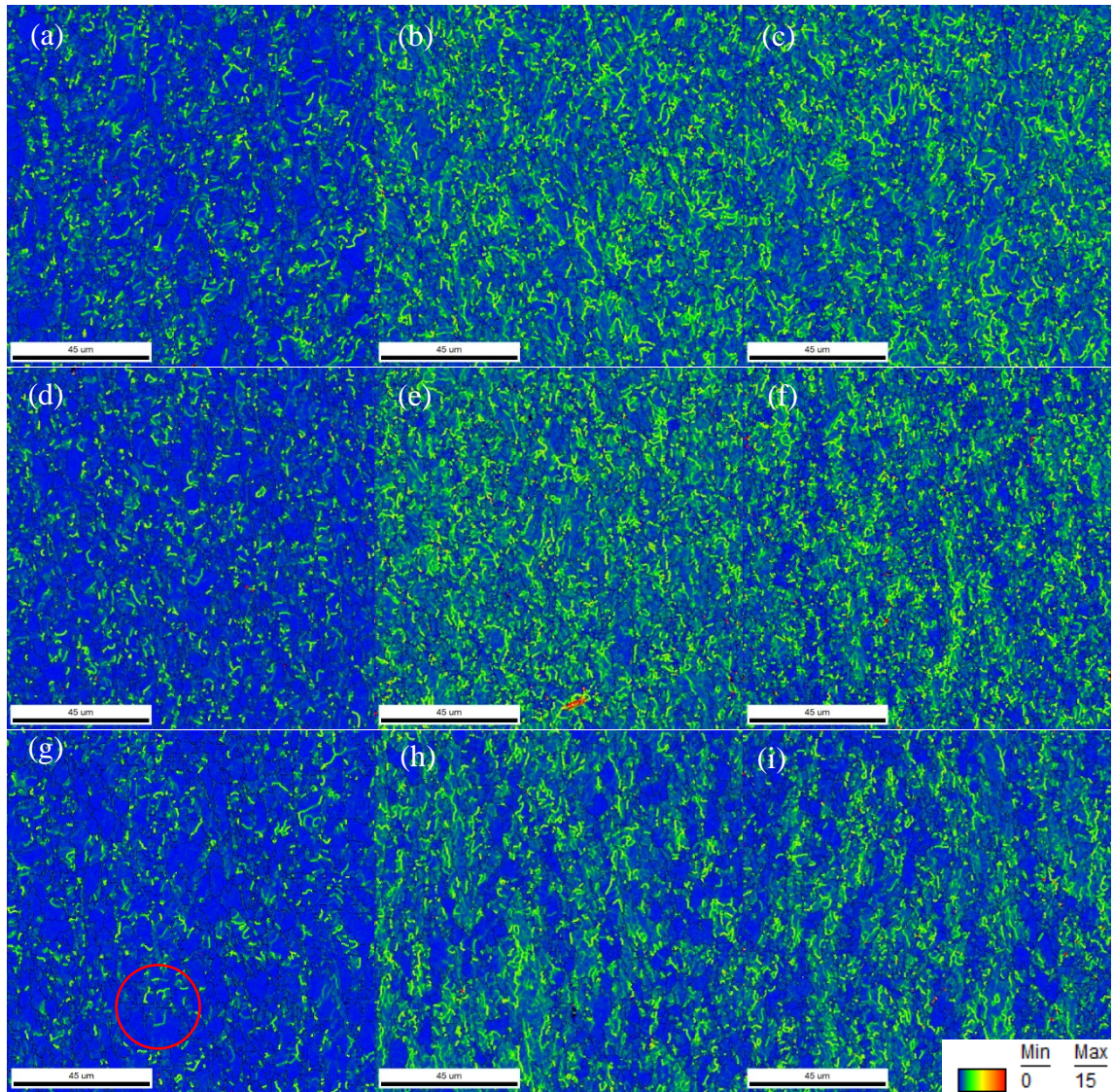


Figure 6.10: Kernel average misorientation map of steels with (a) finish rolling temperature 870°C, coiling temperature 610°C; (b) finish rolling temperature 870°C, coiling temperature 530°C; (c) finish rolling temperature 870°C, coiling temperature 450°C; (d) finish rolling temperature 810°C, coiling temperature 610°C; (e) finish rolling temperature 810°C, coiling temperature 530°C; (f) finish rolling temperature 810°C, coiling temperature 450°C; (g) finish rolling temperature 750°C, coiling temperature 610°C; (h) finish rolling temperature 750°C, coiling temperature 530°C; (i) finish rolling temperature 750°C, coiling temperature 450°C

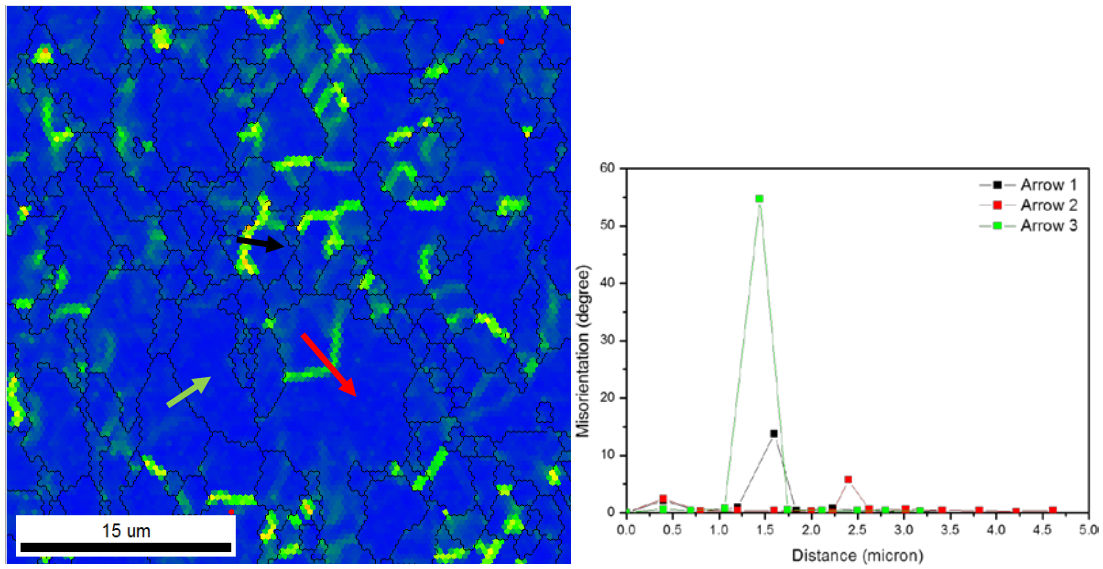


Figure 6.11: KAM map of point to point misorientation

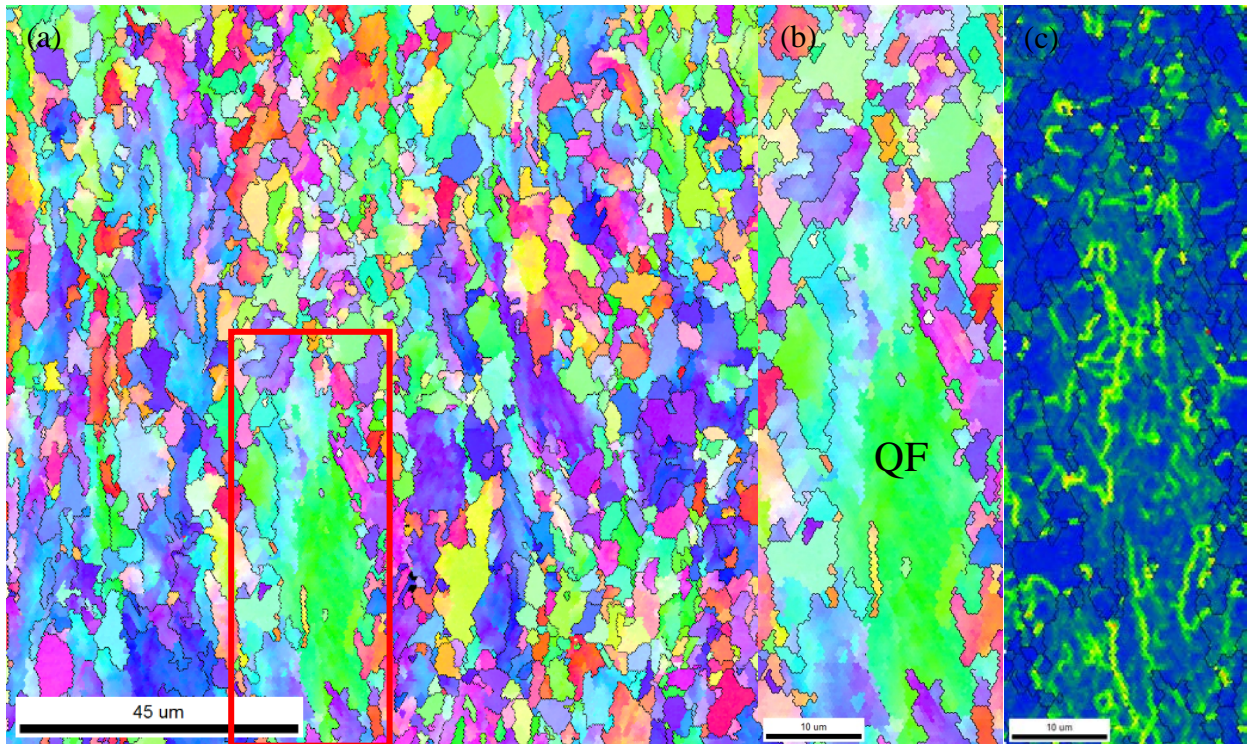


Figure 6.12: Subgrain structure within quasi-polygonal ferrite grain from EBSD (a) IPF; (b) zoomed IPF; (c) KAM of the zoom area

Table 6.3: Kernel Average Misorientation, °

| | | | | |
|----------------------|------------------|------|------|------|
| Conventional EBSD | FRT, °C \ CT, °C | 610 | 530 | 450 |
| | 810 | 0.53 | 0.64 | 0.67 |
| High resolution EBSD | FRT, °C \ CT, °C | 870 | 810 | 730 |
| | 810 | 0.45 | 0.57 | 0.61 |

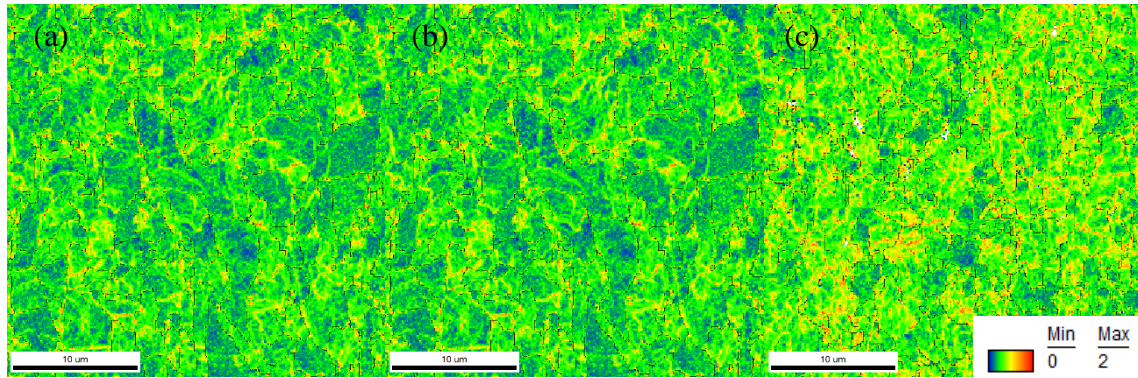


Figure 6.13: KAM results ° (a) 610°C; (b) 530°C; (c) 450°C

From the KAM values listed in the table and the KAM map, the green color indicates a low KAM value region (low lattice distortion) and yellow color indicates a higher KAM value region. It can be seen that the KAM maps vary in a similar way as the KAM data within a 15° threshold. The steels with a coiling temperature of 610°C also show lowest KAM value and the, and the steels with lower coiling temperatures have higher KAM values within a 2° threshold. However, in these maps, from Table 6.3, it can be seen that the KAM value increases as the coiling temperature decreases. That is possibly due to the formation of quasi-polygonal ferrite and bainite with higher dislocation density as the coiling temperature decreases.

According to the equation, the dislocation density based on the KAM from the EBSD can be calculated, and the result is shown in Table 6.4.

Table 6.4: Dislocation density based on KAM, mm⁻²

| FRT, °C \ CT, °C | 610 | 530 | 450 |
|------------------|---------|---------|---------|
| 810 | 3.3E+14 | 4.3E+14 | 4.6E+14 |

6.2 THE INFLUENCE OF THE THERMOMECHANICAL PROCESSING PARAMETERS ON THE MECHANICAL PROPERTIES

6.2.1 The influence factors on the strength

Based on the hardness and tensile results, the strength varies between each thermomechanical processing parameter. The finish rolling temperatures can have effects in multiple ways, i.e. the acceleration of the transformation and the refinement of the microstructure by the decrease of the finish rolling temperature. The finish rolling temperatures involved in this study were 870°C, 810°C and 750°C, which were above the Ar₃ temperature (700°C). As Figure 5.18 shows, for steels with a coiling temperature of 610°C, as the finish rolling temperature decreases from 870°C to 750°C, the tensile strength also drops. However, for steels with lower coiling temperatures, as the finish rolling temperature decreases, the tensile strength increases. A possible explanation for that is at the coiling temperature of 610°C, fine carbides precipitates form during the coiling in the ferrite grains. As the vanadium has very high solubility in the steels, there should be a considerable amount of vanadium still remaining in the solid solution after finish rolling. Therefore, as the finish rolling temperature decreases, the solubility of vanadium is lower, and there is less element remaining in the solid solution, and during the coiling process, the steel with a higher finish rolling temperature is more saturated than the steel with a lower finish rolling temperature, therefore, the

steels with lower finish rolling temperature have less potential to have precipitation strengthening, as a result, the strength will be lower, but the difference is not too much.

For the steels with coiling temperatures of 530°C and 450°C, which according to the CCT diagram, both are in the bainitic transformation region. In the meantime, due to the lower coiling temperatures, there wasn't enough fine precipitates formed during coiling to provide extra strengthening. However, the precipitates formed during hot rolling can still make a difference. Because of the lower solubility product and high strain involved when the steels were deformed in a lower finish rolling temperature, resulting in a higher fraction of strain-induced precipitates. However, those precipitates were probably coarser than the precipitates formed during coiling in the ferrite grains and may have not been able to increase strength. Besides that, another factor to alter the strength is the matrix microstructure. From the SEM microstructure and KAM results, it is already known that the lower coiling temperatures can result in quasi-polygonal ferrite, granular bainite and even upper bainite, all of which contain a high density of dislocations. From Figure 6.1, it is known that the finish rolling temperatures were all below the recrystallization temperature, and the prior austenite grains become more elongated as the finish rolling temperature decreases, indicating higher strain introduced into the grains and the dislocation accumulated within them. In the meantime, from previous results, the dislocation density increases as the coiling temperature decreases which makes a different contribution to the final strength.

The contribution from dislocation strengthening to the total yield strength is calculated as the following equation:

$$\sigma_p = M\alpha Gb\sqrt{\rho} \quad (6.6)$$

where M is the Tyler factor ($M=1.84^{[157]}$), α is a numerical factor dependent on the structure ($\alpha=0.24^{[158]}$), G is the shear modulus ($G=83\text{GPa}$) and b is the Burger's vector and ρ is the dislocation density. The calculated results are shown in Table 6.5.

Table 6.5: Contribution from dislocation strengthening from EBSD data, MPa

| FRT, °C \ CT, °C | 610 | 530 | 450 |
|------------------|-----|-----|-----|
| 810 | 165 | 189 | 195 |

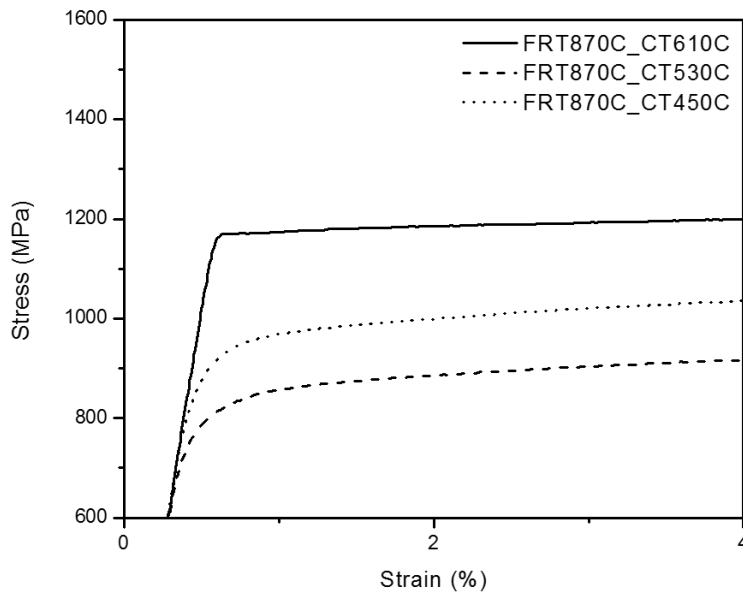


Figure 6.14: Engineering stress-strain curve zoomed in with a finish rolling temperature of 870°C

Figure 6.14 shows the zoomed in room temperature stress-strain curve of the steels with the highest finish rolling temperature. It can be seen that the steel with a coiling temperature of 610°C has a yield point, showing a discontinuous yielding behavior, while steels with lower coiling temperatures show continuous yielding behavior. Other steels with lower finish rolling temperatures show the similar behavior. N. J. Kim et al. explained the effect of hard secondary phases on the yield behavior in acicular ferrite-based structures^[17]. The increased in the volume fraction of secondary hard phases or low temperature transformation products is associated with

the continuous yielding behavior and low yield ratio because the increased volume fraction of secondary phases promotes the movement of dislocations at boundaries between the secondary phases and nearby soft phases^[159]. This phenomenon is very common in dual phase (DP) steels which consists of both ferrite and martensite. In this study, from previous results, it is known that secondary hard phase like martensite/austenite constituents (MA) and low temperature transformation products like granular bainite (GB) or upper bainite (UB) exist in the steels with lower coiling temperatures. While in the steels with a coiling temperature of 610°C, the microstructure is mostly polygonal ferrite. The second phases in the steels with lower coiling temperatures introduce a large density of mobile dislocations on the interface of ferrite and second hard phase, also because of the lack of precipitated carbides, resulting in a continuous yield behavior. According to Cottrell and Bilby^[160], the appearance of yield point is attributed to the mechanism based on the lack of mobile dislocations. In the steels with a coiling temperature of 610°C, the existence of huge amount of fine carbides can hinder the movement of the dislocations, as the deformation continues, until the accumulated dislocations break through the obstacles, resulting in the yield point. Similar phenomenon was observed in a Nb-Ti-Al alloy that dislocation is pinned by precipitates of ω -phase instead of a cloud of interstitial atoms^[161].

The yield ratio is a function of both yield strength and work hardening rate^[162, 163]. From Figure 6.15, it can be seen although all the steels have high yield ratio, the steels with a coiling temperature of 610°C have higher yield ratio than those with lower coiling temperatures, indicating a higher working hardening capacity for those steels with lower coiling temperatures.

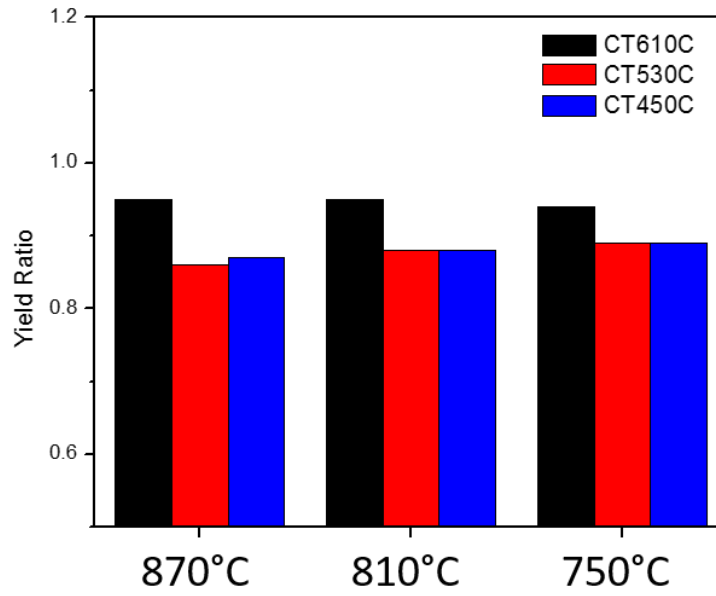


Figure 6.15: Yield ratio bar chart of all the steels

In this part, we assume that the strength from the highest coiling temperature is coming from the precipitation strengthening during coiling. This theory was proved by the JMatPro calculation shown in Figure 6.16. It shows carbides formed in the steels quenched from 870°C and held at 610°C, 530°C and 450°C for different amount of time. It can be seen that the phase fraction of MC carbides decrease as the holding temperature drops, while on the contrary, the fraction of M₂C carbides increase as the holding temperature decreases. However, the particle size of MC carbides increase as the holding temperature decreases. However, the particle size of MC carbides is always smaller than M₂C carbides, especially at 450°C, the M₂C carbides can easily reaches to hundreds of nanometers, whereas, the MC carbides always keep in a small size. And it is well known that coarse particles have less or do not have the effect of strengthening. Therefore, from the JMatPro results, the most effective precipitates for strengthening during coiling is the MC type carbides at 610°C due to it fine size and high volume fraction.

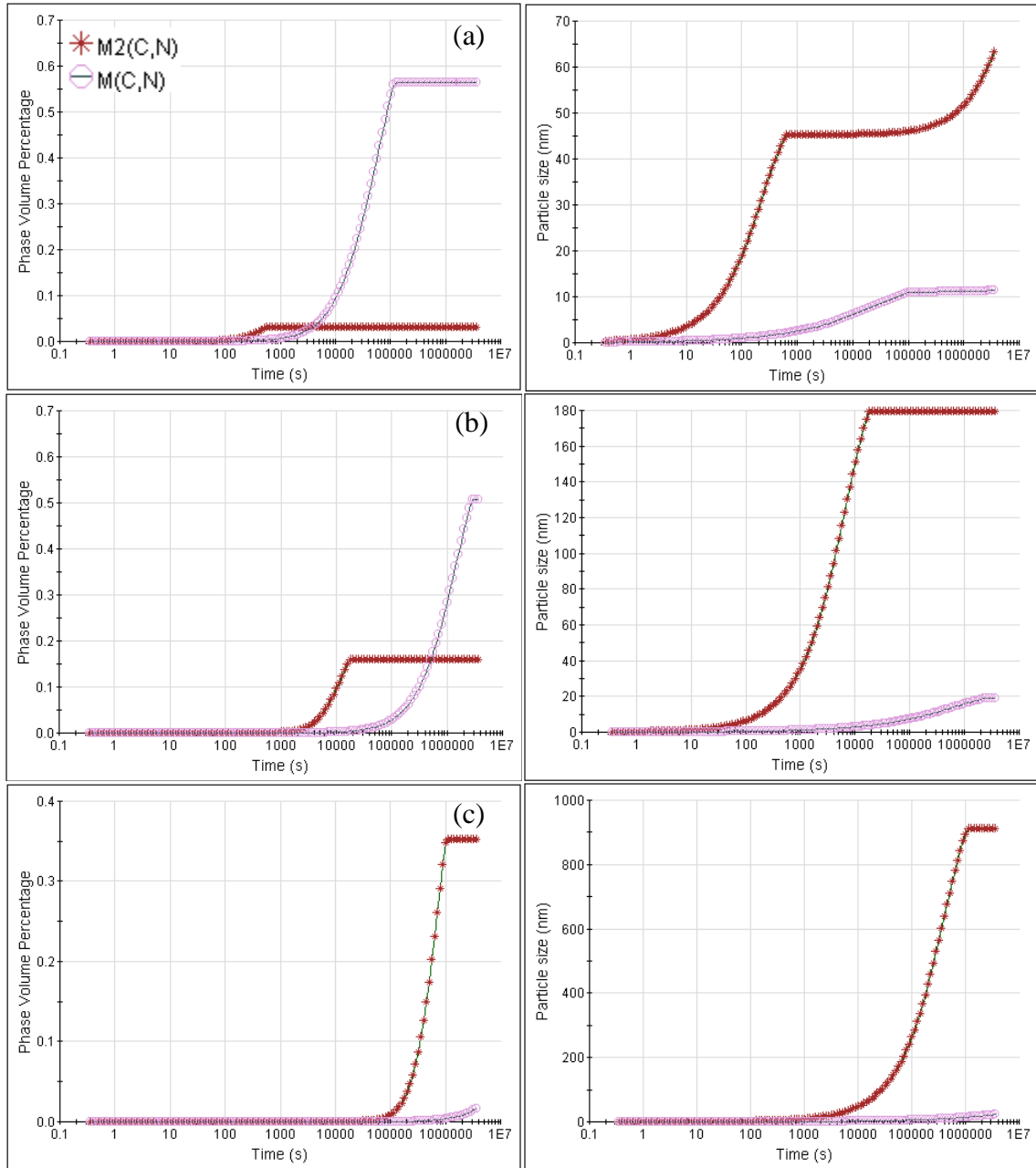


Figure 6.16: JMatPro calculation of volume fraction and particle size of carbides at different holding temperatures (a) 610°C; (b) 530°C; (C) 450°C

Based on the particle size and volume fraction from the JMatPro results, and according to the Equation 6.7 ^[164] which is an alternative of the Ashby-Orowan Equation 6.8^[104]:

$$\Delta\sigma_p = 8.995 \times 10^3 \frac{f_v^{\frac{1}{2}}}{d} \ln(2.417d) \quad (6.7)$$

$$\Delta\sigma_P = \frac{5.9\sqrt{f}}{\bar{x}} \cdot \ln\left(\frac{\bar{x}}{2.5 \times 10^{-4}}\right) \quad (6.8)$$

where f is the volume fraction and d or \bar{x} is the particle size. The contribution from the precipitates during coiling from finish rolling temperature of 870°C is shown in Table 6.6.

Table 6.6: Strengthening contribution from different types of carbides precipitates, MPa

| Temperature, °C | MC | M ₂ C | Total |
|-----------------|-----|------------------|-------|
| 610 | 201 | 19 | 220 |
| 530 | 64 | 12 | 76 |
| 450 | 6 | 2 | 8 |

From Table 6.6, it can be seen the large difference in the strengthening effect of carbides at different coiling temperatures. At the coiling temperature of 610°C, the total contribution is 220MPa, of which 201MPa is coming from MC carbides. As for the lower coiling temperatures, the strengthening effect is much lower, 76MPa from 530°C and 8 MPa from 450°C. At every holding temperature, the majority of the precipitation strengthening comes from the MC carbides. Although this is a simulated result, it clearly shows the effect of coiling temperatures on the precipitation strengthening. The results calculated from Eq.6.8 is a little lower than the data in Table 6.6, but they also show the similar trend that precipitation strengthening in the coiling temperature of 610°C is the highest, and most of the contribution is coming from the MC type particles.

In order to prove that the coiling temperature is the key factor to result in the steels with a high strength, the coiling temperature of 610°C showed very high strength compared to those with lower coiling temperatures. One speculation is the precipitation strengthening proceeded thoroughly during the 1h slow cooling at 610°C, while at the lower coiling temperatures of 530°C and 450°C, the temperature wasn't high enough to allow the precipitates to form completely. Thus, one group of conditions were picked to verify this assumption.

The conditions were selected are those with finish rolling temperature of 870°C and variations of coiling temperatures. To accelerate this precipitation process, a 30% reduction pre-cold reduction was performed, then the steels were aged at 600°C for different time and evaluated by the Vicker's hardness test. Figures 6.17 to 6.19 are the 2% Nital etched optical microstructures of the cold rolled steels after being aging for 0 minute (as cold rolled), 10 minutes, 30 minutes, 1 hours, 2 hours and 4 hours. As it shows, after aging for different amount of time at 600°C, the microstructure did not change too much with the holding time, and all the grains were still elongated along the rolling direction. According to the CCT diagram shown in Figure 6.5, 600°C lies on the bottom of the ferritic transformation region or at the top of the bainitic transformation region. Furthermore, the temperature of 600°C is not high enough to drive the recrystallization of ferrite to occur. Thus, the effect of microstructure change of the matrix on the hardness can be eliminated.

Figure 6.20 shows the VHN (300gf) value of all the cold rolled and aged steels. As the matrix microstructures were not changed too much, the reason causing the difference in the hardness is the formation of the precipitates during the aging process. As shown before in the Table 5.2, the yield ratio of the steels with a coiling temperature of 610°C is very high, which means they have very low working hardening behavior. For those as cold rolled steels, it can be seen from Figure 6.20 that after 30% cold reduction and aging at 600°C, the steels with a coiling temperature of 610°C did not have much increase in the hardness, while those with lower coiling temperatures showed a large jump in the hardness because they had a lower yield ratio with much solute still in solution after coiling.

For the steels with a coiling temperature of 610°C, no matter how aging time extends, the hardness value remains at a high and relatively constant level. However, for the steels that have

lower coiling temperatures, as the holding time prolongs, the hardness increases. By the time of holding for 4 hours, the VHN values of steels with coiling temperatures of 530°C and 450°C are even higher than the steels with a coiling temperature of 610°C.

This JMatPro simulation and the cold rolling and aging experiment shows the incompleteness of precipitation process at lower coiling temperatures which cause the lower strength in those conditions. However, the high strength from the highest coiling temperature of 610°C is due to more complete precipitation strengthening.

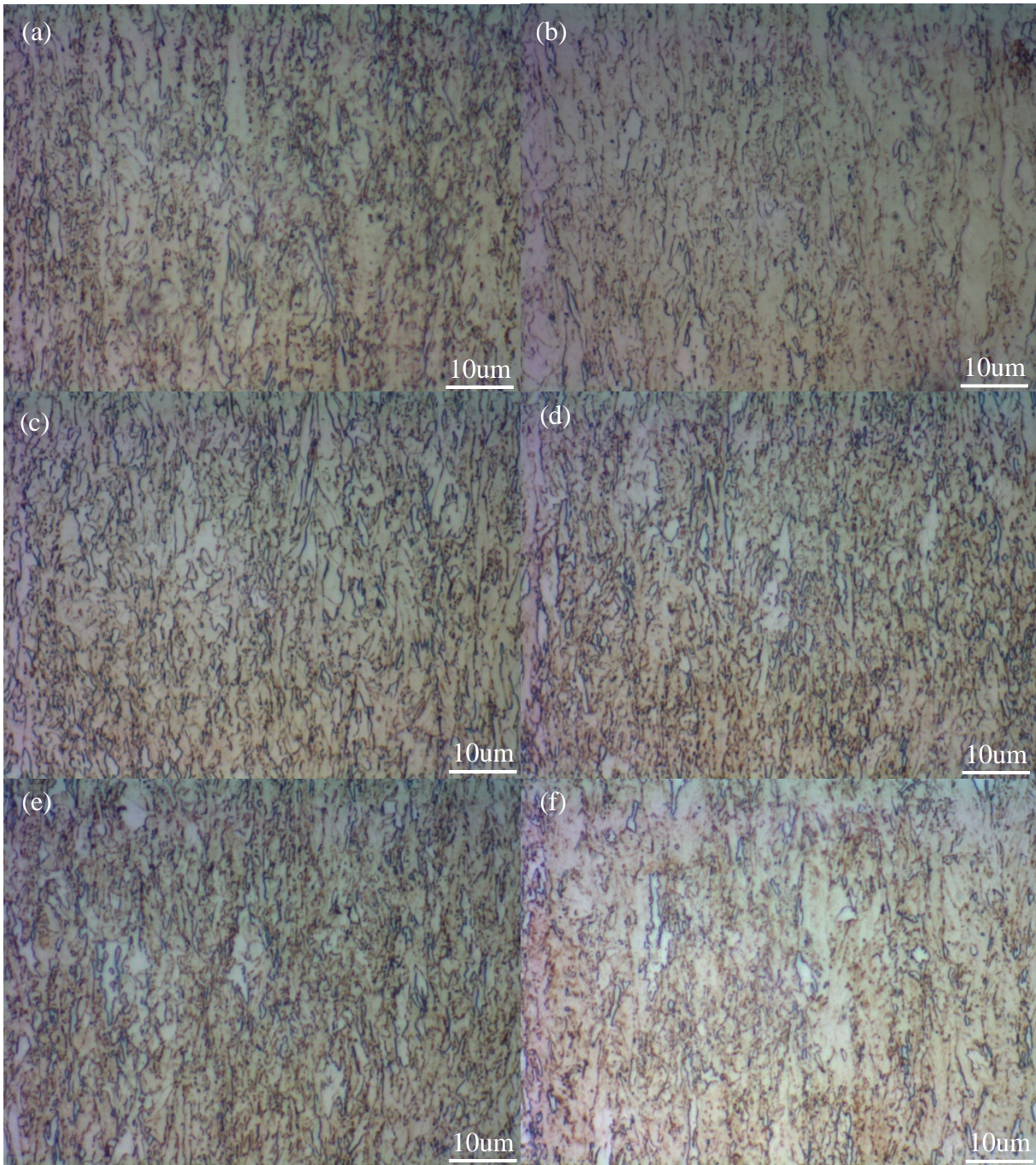


Figure 6.17: Optical micrograph of 30% cold rolled steel with a finish rolling temperature of 870°C and coiling temperature of 610°C aged at 600°C for (a) 0min; (b) 10min; (c) 30min; (d) 60min; (e) 120min; (f) 240min

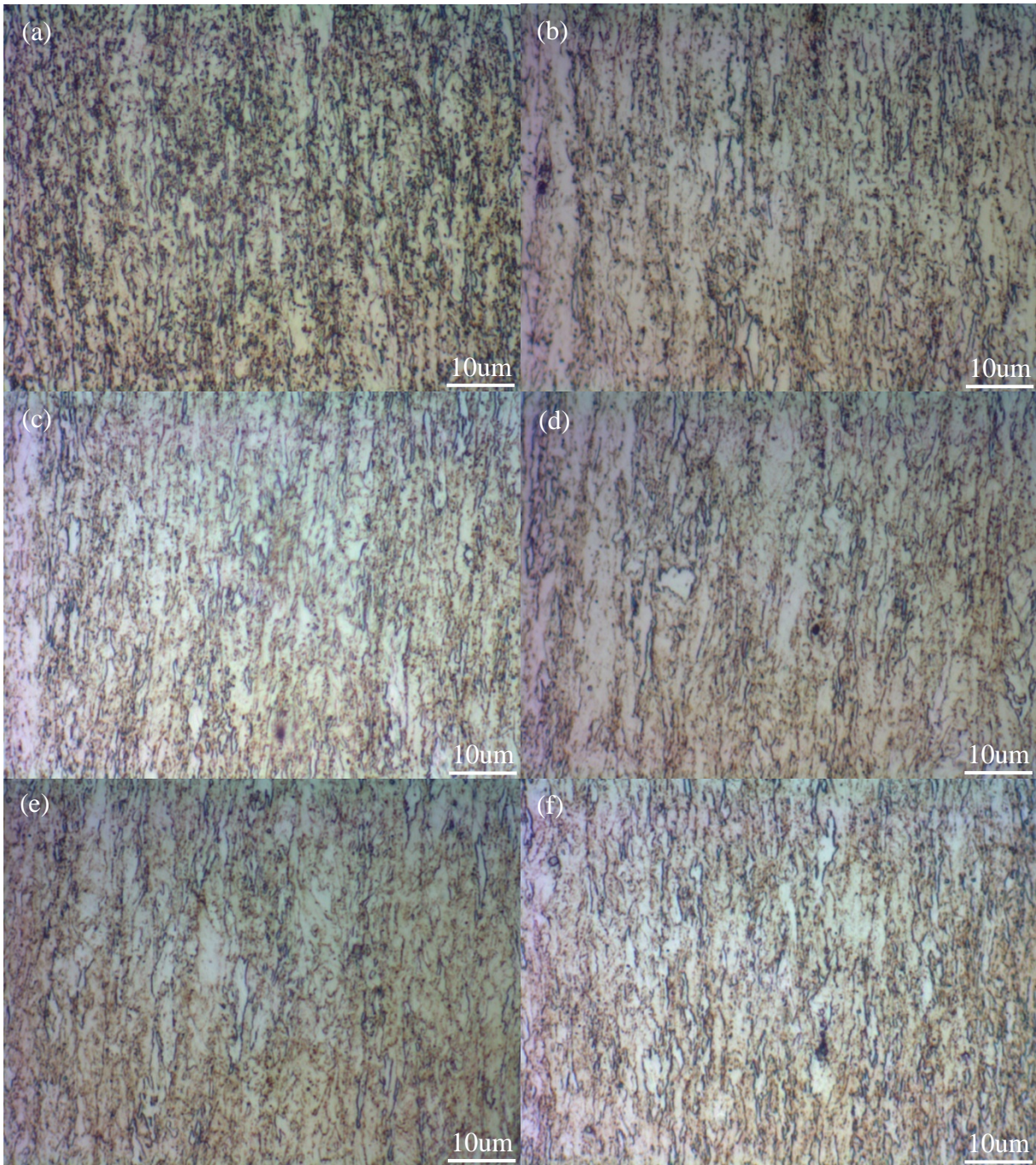


Figure 6.18: Optical micrograph of 30% cold rolled steel with a finish rolling temperature of 870°C and coiling temperature of 530°C aged at 600°C for (a) 0min; (b) 10min; (c) 30min; (d) 60min; (e) 120min; (f) 240min

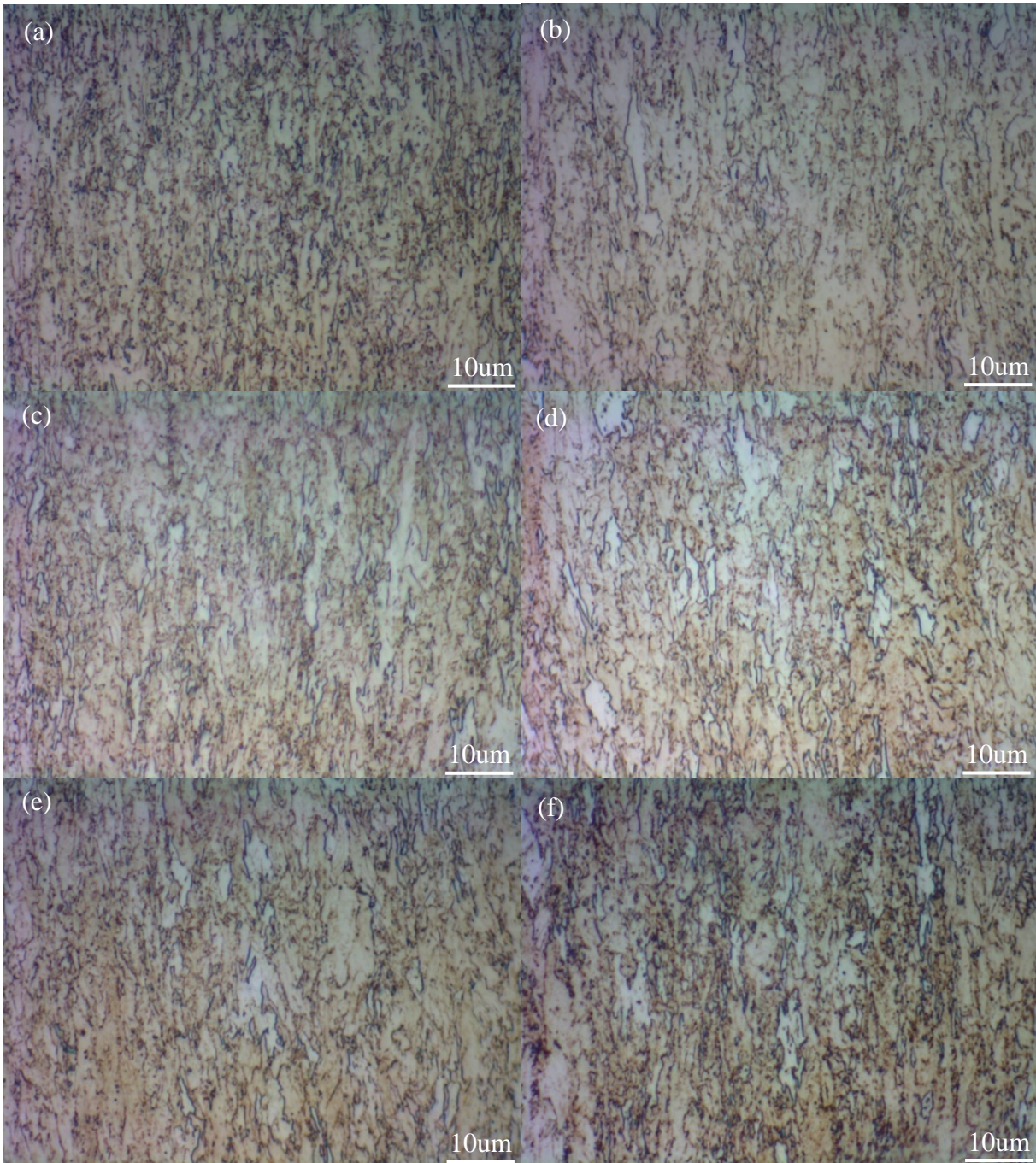


Figure 6.19: Optical micrograph of 30% cold rolled steel with a finish rolling temperature of 870°C and coiling temperature of 450°C aged at 600°C for (a) 0min; (b) 10min; (c) 30min; (d) 60min; (e) 120min; (f) 240min

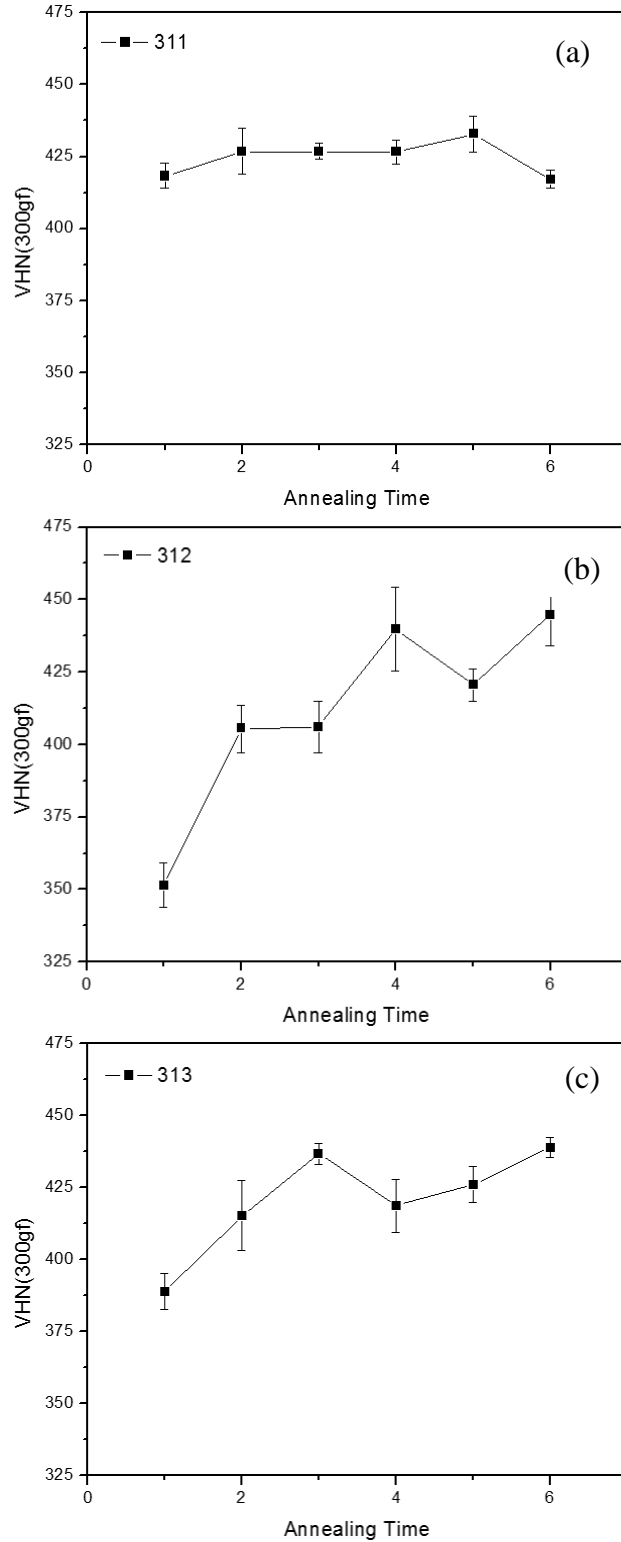


Figure 6.20: Vicker's hardness number of the cold rolled and aged steels with a finish rolling temperature of 870°C and a coiling temperature of (a) 610°C; (b) 530°C; (c) 450°C

As Figure 6.21 shows, the fracture surface exhibits mainly dimpled rupture, which indicates the ductile fracture. However, in the center of the fracture surface, secondary micro-cracks can be seen across the cross section area. Also, the width of the cracks increases as the strength of steels increase. Very large TiN inclusions with several microns on a side can be seen on the fracture surface as shown in Figure 6.22.

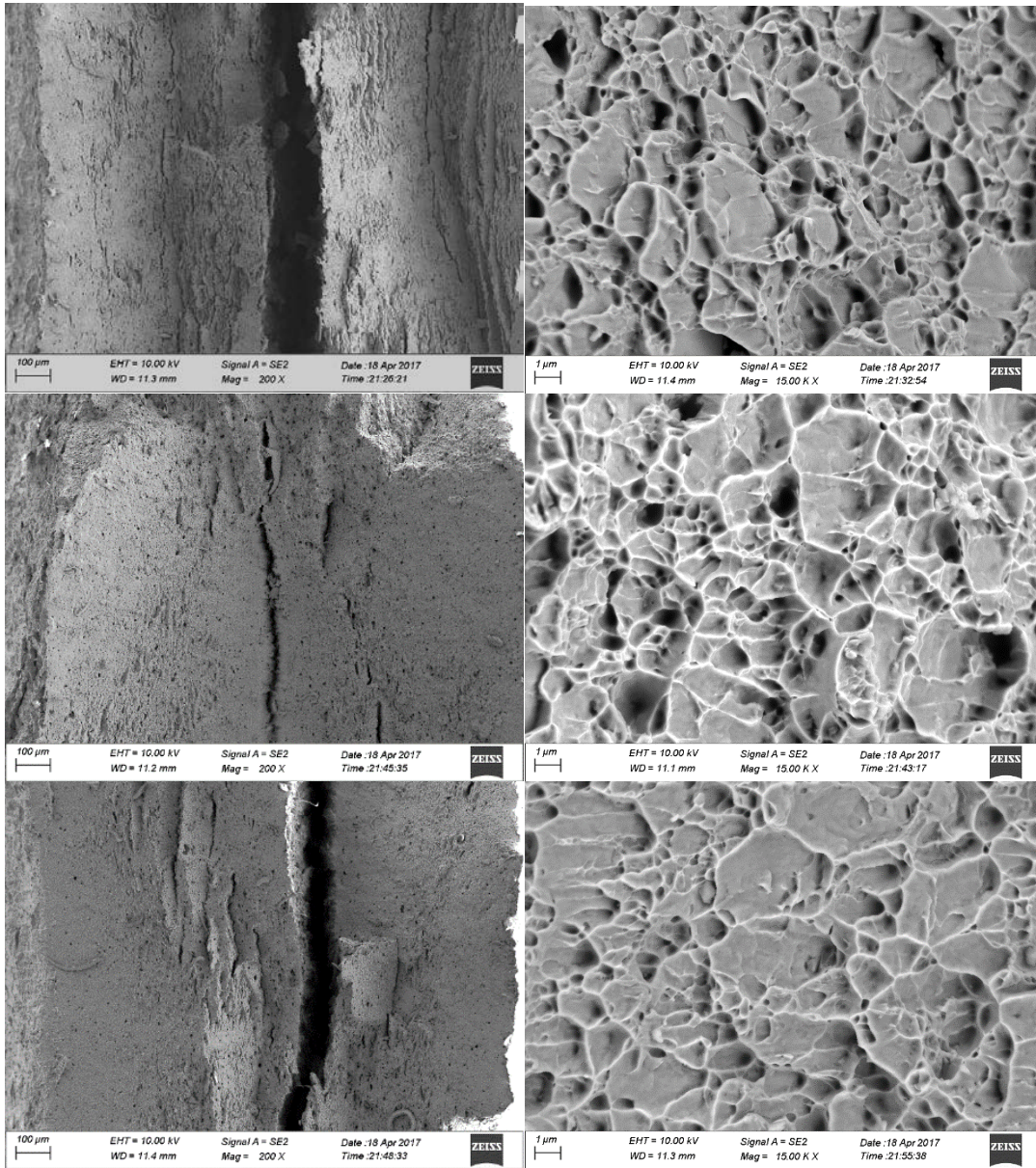


Figure 6.21: Fracture surface on the tensile specimens with a finish rolling temperature of 750°C and a coiling temperature of (a) 610°C; (b) 530°C; (c) 450°C

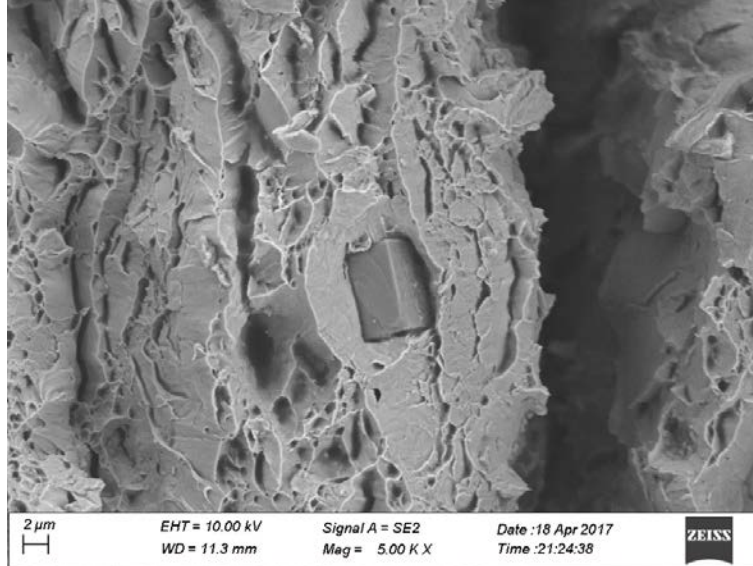


Figure 6.22: Observation of TiN on the fracture surface of a tensile specimen

6.2.2 The influence factors on the toughness

The toughness of the steels is strongly dependent on the ferrite grain size and precipitation hardening. A refinement of grain size can improve the cleavage resistance and thereby improve toughness, whereas, precipitation tends to deteriorate the toughness^[52, 165]. The relationship has been incorporated into an equation for ferrite-pearlite microstructures by Pickering and Gladman which is shown as^[166]:

$$ITT(^{\circ}C) = -19 + 44(\text{pct Si}) + 700(\sqrt{\text{pct N}_f}) + 2.2(\text{pct P}) - 11.5(d\alpha)^{-0.5} \quad (6.9)$$

where $d\alpha$ is the ferrite grain size in millimeters, P is volume fraction of pearlite, N_f is the free nitrogen and Si is the solute Si.

From Figure 6.1 and Table 6.1, it is known that the Sv did not vary much based on the different finish rolling temperatures, therefore, similar ferrite grain size was expected with the same coiling temperature. In general, low finish rolling temperature result in finer ferrite grain size^[111, 167], however, from the EBSD results given in Table 6.2, the grain size of all the steels were

quite close. Steels with lower coiling temperatures sometimes had a little larger average grain size due to the formation of coarser quasi-polygonal ferrite grains, and those coarse, elongated grains will be detrimental to the toughness of the steels.

Figure 6.23 is the accumulated distribution of the grain size of all the steels. It can be seen that the steels with a coiling temperature of 610°C have much more uniform grain size distribution than other steels with lower coiling temperatures. The extending tails of the curves of the steels with lower coiling temperatures was the result of the existence of coarse quasi-polygonal ferrite. These tails would be expected to reduce the toughness by reducing the resistance to cleavage cracking.

From Figure 5.19, steels with a coiling temperature of 610°C show the worst toughness, and steels with a coiling temperature of 530°C have the best toughness, steels with a coiling temperature of 450°C show intermediate toughness. One interesting thing is that at lower coiling temperatures, the steels with a finish temperature of 810°C exhibit higher absorbed energy than other finish rolling temperatures. According to Table 6.2, for lower coiling temperatures, the steels with a finish rolling temperature of 810°C have smaller average grain size. Figure 6.4(b) and (c) show the accumulated area frequency curve of steels with coiling temperature 530°C and 450°C and different finish rolling temperatures. It can be seen the red curve which represents the steel with a finish rolling temperature of 810°C, always stands above the other curves or shorter than the other two, which means the microstructures either have a higher fraction of fine grains or lower fraction of coarse grains. This smaller average grain size is a combined result of the higher fraction of fine grains and lower fraction of larger grains. Since the refinement of the grains has a very large influence on the toughness, it is no wonder that the steel with lower coiling temperatures have the best toughness in the intermediate finish rolling temperature.

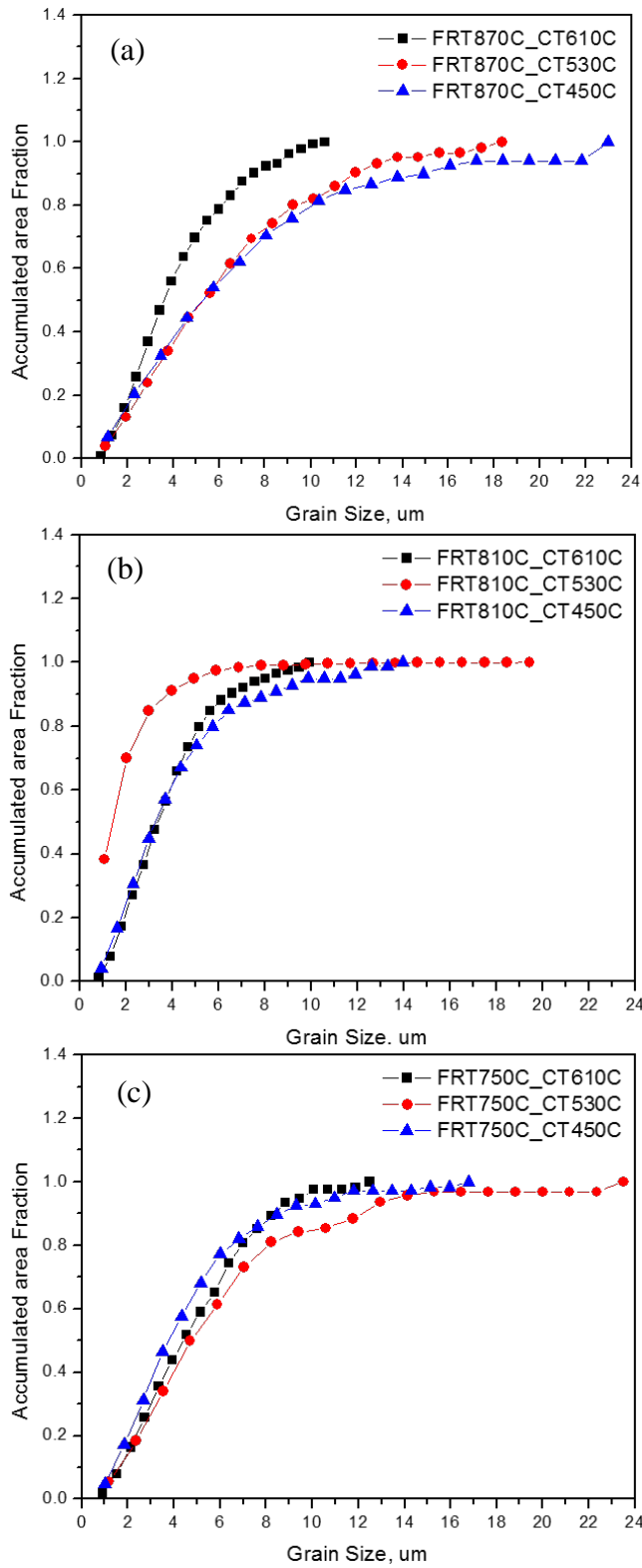


Figure 6.23: Accumulated grain area fraction curve of steels at finish rolling temperature of (a) 870°C; (b) 810°C; (c)

750°C

A finer grain structure is assumed to be beneficial to the toughness; however, in the steels with a coiling temperature of 610°C, they show very low toughness. From the Eq6.8, it is known that the grain size is not the only factor that determines the toughness of the steels.

Figure 6.24 shows the effect of an aging process on the change of hardness and impact toughness^[168]. It can be seen that hardness value increases as the ageing time prolongs, which indicates the effect of precipitation strengthening. However, the impact toughness drops largely as the precipitates formation proceeds. From Figure 6.16, it can be seen that steels with a coiling temperatures of 610°C has a very large amount of fine precipitates, while in the steel with the lower coiling temperatures, the precipitation strengthening effect did not have a big influence. From the KAM results, it is known that the steels with lower coiling temperatures have higher fraction of dislocations or subgrain structures, and the dislocation density increases as the coiling temperature decreases. The existence of these defects will also deteriorate the toughness.

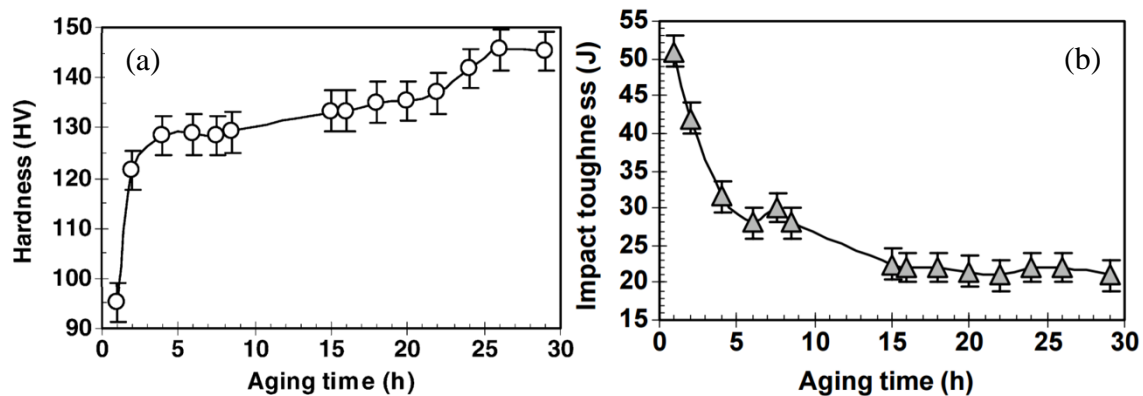


Figure 6.24: Variation in (a) hardness and (b) impact energy of 7020 alloy specimens aged at 413 K for various times following 96 h natural ageing

From Figures 5.7 to 5.11, it is known that the distribution of carbides and M/A constituents differ with each coiling temperatures. The M/A islands and carbides can be rarely found in the steels with the highest coiling temperature. However, fine M/A islands and uniformly distributed

carbides can be observed in the steels with intermediate coiling temperature, and in the steels with the lowest coiling temperature, not only coarser M/A islands can be seen, but carbides became segregated, all of which can be harmful to the toughness.

After the impact test, secondary cracks on the TD-RD face near the notch was investigated. In the optical micrograph shown in Figure 6.25, obvious secondary cracks can be only found in the steel with the highest coiling temperatures. From the figures, it can be seen that the crack mainly penetrates through the prior austenite grains, and sometimes, the crack could be deflected at grain boundaries and then propagates through another grain. Figure 6.26 shows the crack propagation through ferrite grains. In the steels with a coiling temperature of 610°C (Figure 6.26 (a), (b) and (c)), the crack path is quite straight, especially within some coarse grains, showing very brittle behavior, which is constant with the results shown in Figure 5.19 and 5.21, indicating the low toughness and almost pure cleavage on the fracture surface. While in the steel with a coiling temperature of 530°C (Figure 6.26 (d)), the crack was short, it is not easy to find through the optical microscope, and in the vicinity of the crack, the matrix is highly deformed, and the crack propagates along the deformation bands, which is unlike the microstructure near the crack in Figure 6.26(a), (b) and (c), the grain remained undeformed.

As in the fracture surface in the broken Charpy specimens, it is clear that large sizes of TiN can be seen from Figure 5.24. Besides that, from Figure 6.27, on the cleavage, inclusion sites can be found due to the presence of oxides, sulfides or carbides. From EDAX analysis, the inclusions found in Figure 6.27(c) is (Ti, Mo, V)C. Moreover, according to Isasti et al.^[110], an initiation site appears in a secondary phase with a morphology of M/A particles. Thus, in this steel, the presence of M/A could be an important factor controlling the crack initiation which can be reflected on the toughness. Since that steels with the lowest coiling temperature contain more and coarser M/A

constituents, they absorb less energy during the impact test than the steels with intermediate coiling temperature which has less and finer M/A constituents.

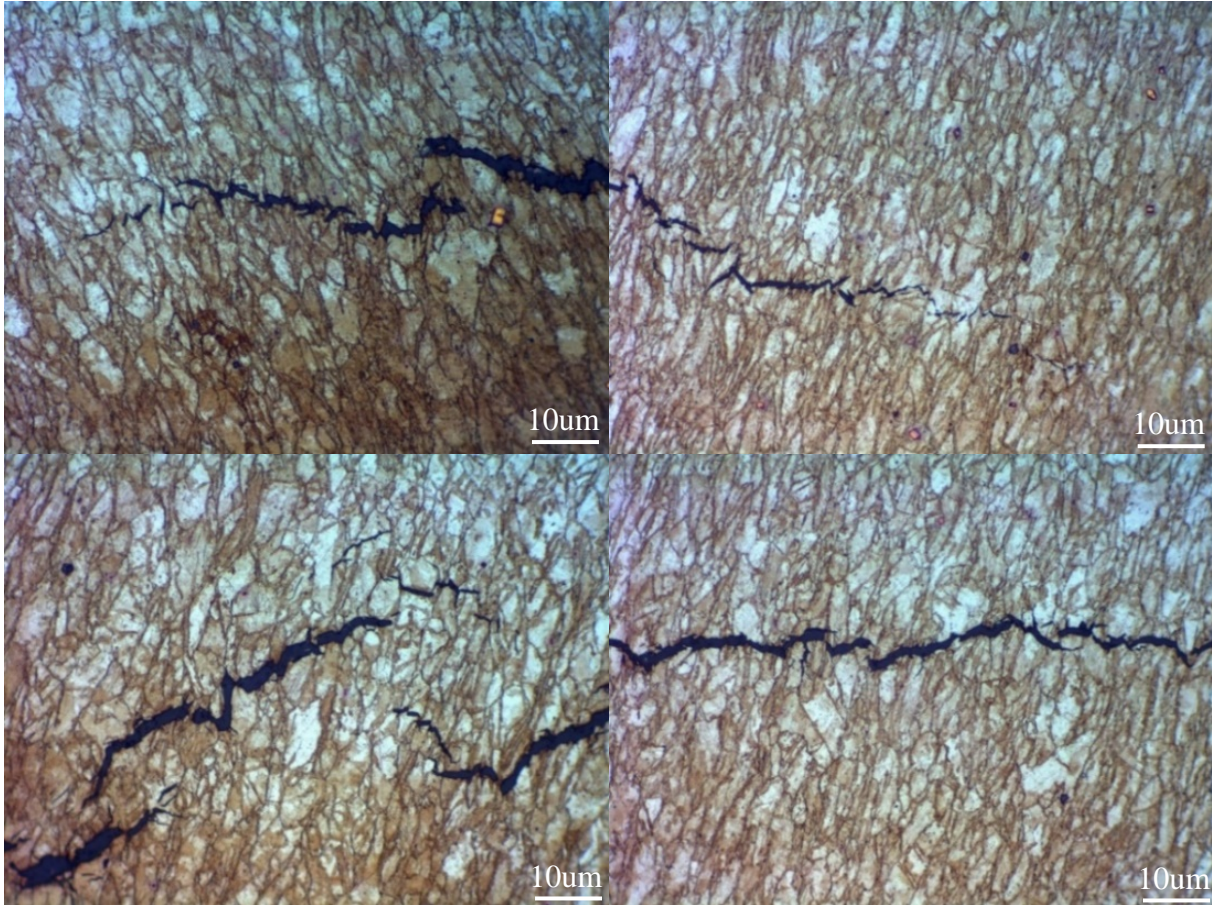


Figure 6.25: Optical micrograph of secondary crack through prior austenite grains

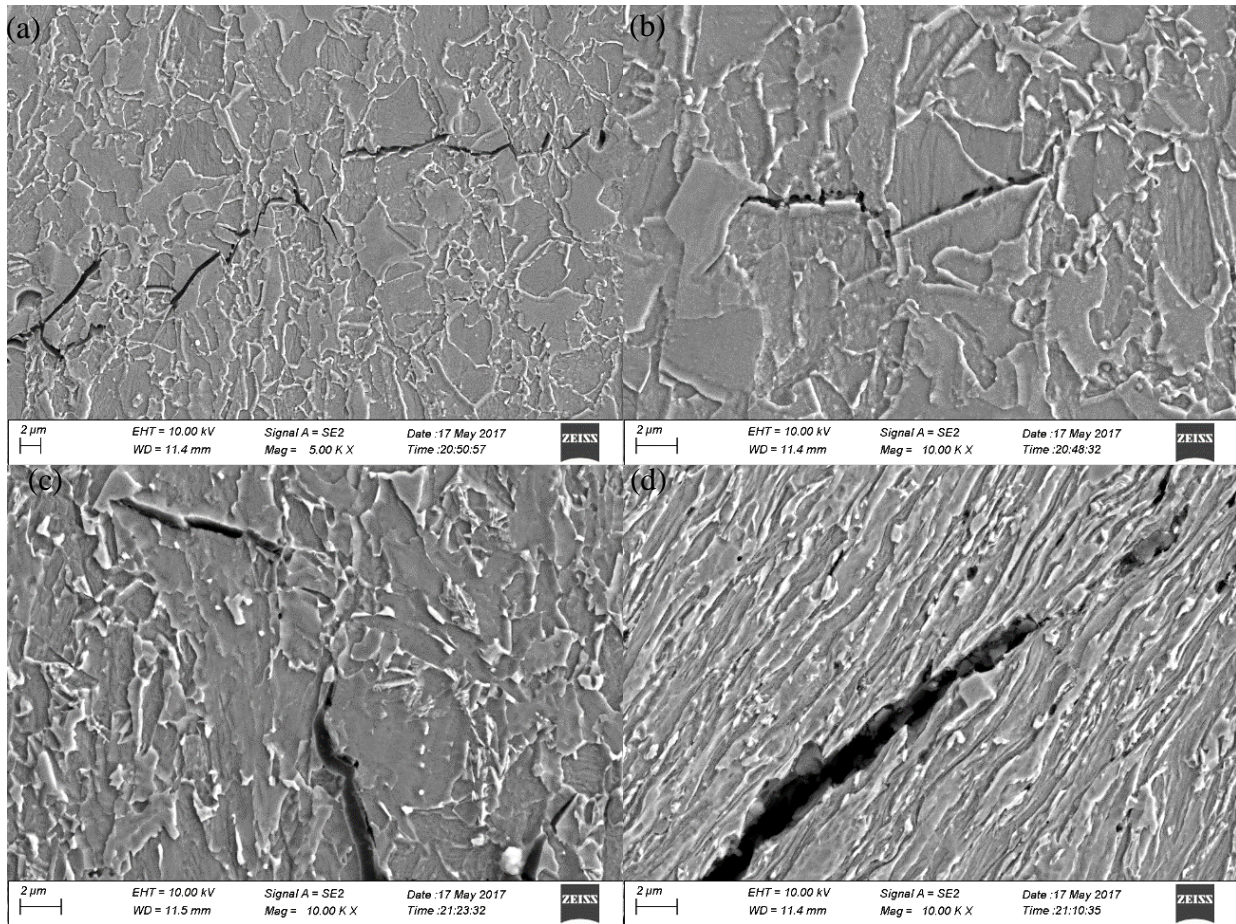


Figure 6.26: Optical micrograph of secondary crack through ferrite grains

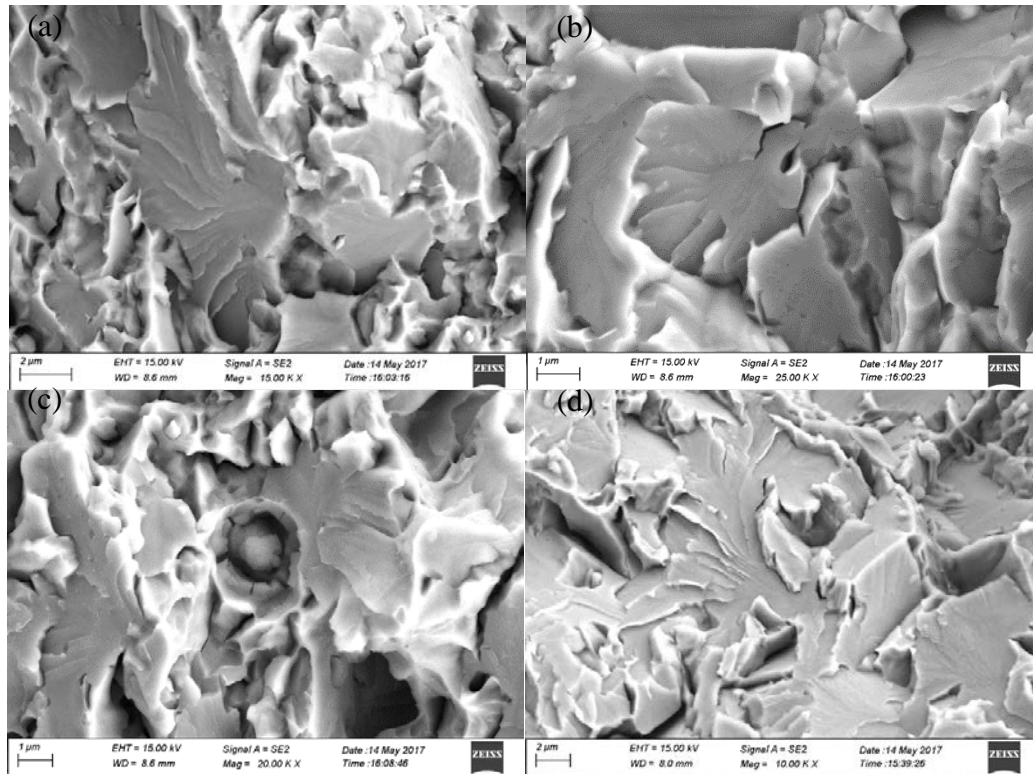


Figure 6.27: Cleavage initiation site on the fracture surface of Charpy specimens

6.2.3 The influence factors on the hole expansion test results

The hole expansion results show a similar tendency as the Charpy impact results, the steels with a coiling temperature of 610°C show the worst HER, and the steels with a coiling temperature of 530°C have the best performance in the test, the steels with a coiling temperature of 450°C have an intermediate HER. And the reasons are also similar to the causes of the performance in the impact test. The existence of the fine precipitates, the high fraction of dislocations and subgrain structures, the carbides, M/A constituents, all can lower the HER. Figures 6.28 and 6.29 show the crack on the specimen surface of steels with a 610°C coiling temperature. From both OM and SEM observation, it can be seen that the crack path is quite straight in the brittle matrix until it encounters coarse TiN inclusions. Because during the hole expanding, the force was coming from

the bottom of the specimens, and the upper surface being investigated was actually under tension, those TiN inclusions could be a stress concentration spot and became an initiation point for the crack to originate. Once the force underneath overcame the bond between the TiN and the matrix, a pit would form and those pits will act as a surface crack when the load applied is high enough, the crack would propagate, until it links other pits, the formation of surface crack would cause the upper surface to be torn which is shown as a smooth region in Figure 6.30(a). Near the tear region, the fracture surface is mainly consisted of cleavages, and of course, large size of TiN is observable.

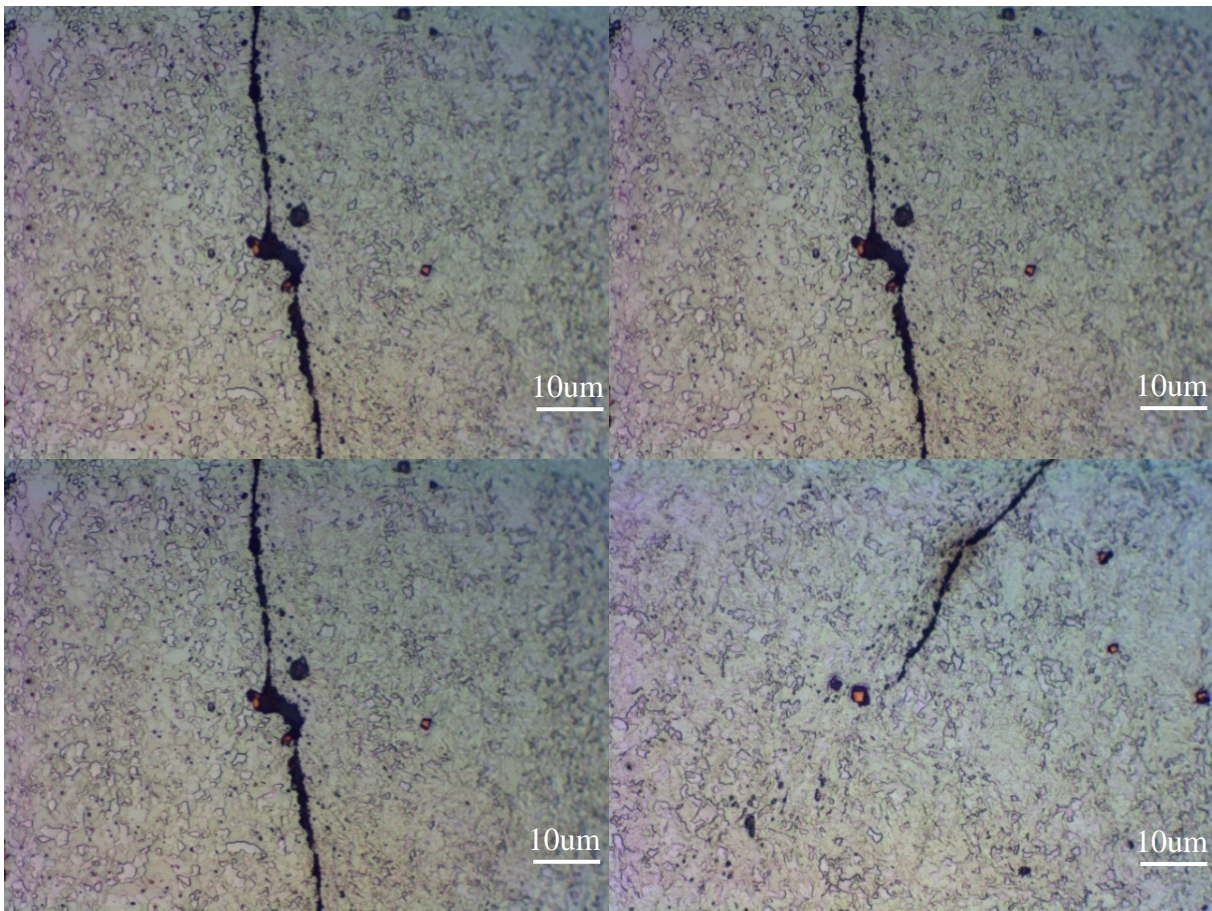


Figure 6.28: Optical micrograph of crack path on the surface of specimen with a coiling temperature of 610°C

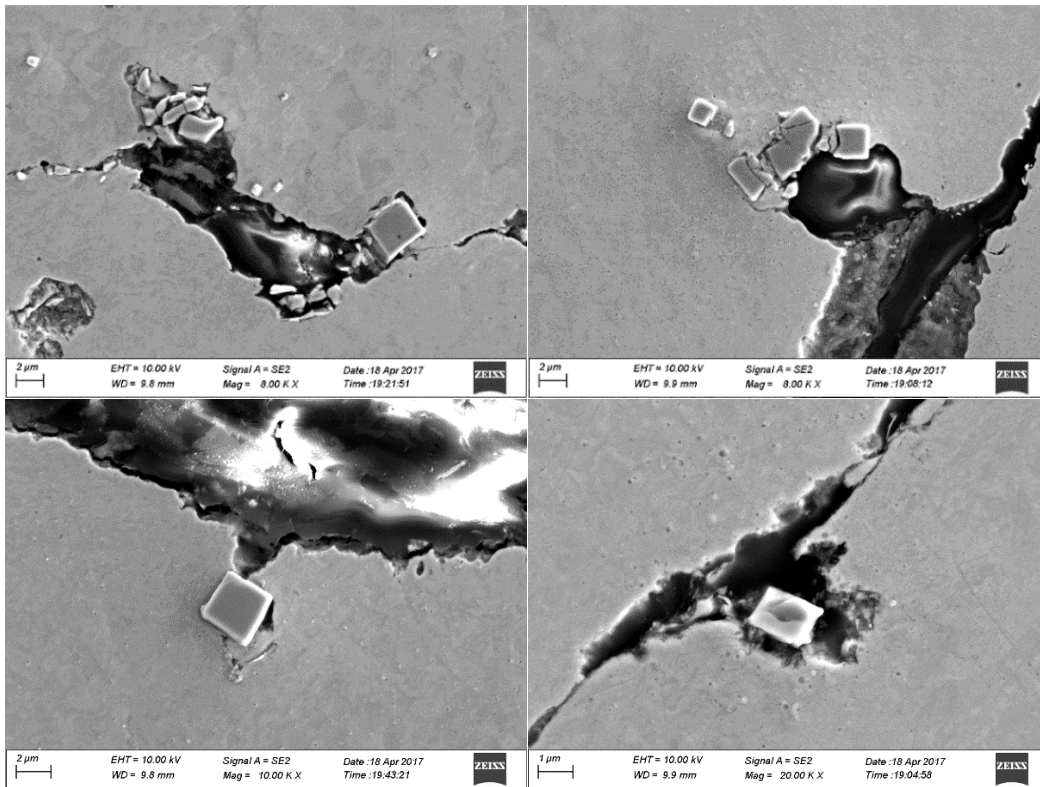


Figure 6.29: SEM micrograph of crack path on the surface of specimen with a coiling temperature of 610°C

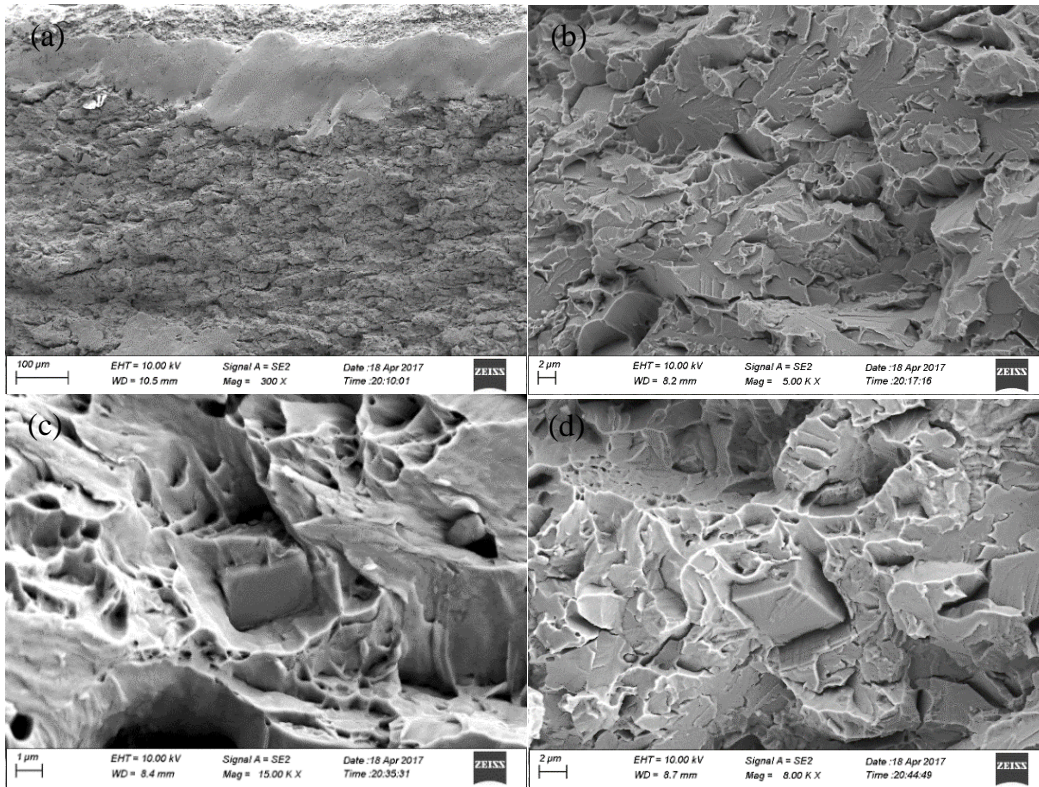


Figure 6.30: SEM micrographs of fracture surface specimen with a coiling temperature of 610°C

To investigate the effect of precipitates on the HER, two-hole expansion test specimens with a finish rolling temperature of 810°C and coiling temperature of 450°C were prepared, one was cold rolled about 30% reduction and the other was cold rolled about the same reduction and then held at 600°C for 1h. They were tested afterwards, and the result and OM are shown in Figure 6.31. It can be seen that after cold reduction, the HER value dropped from initial 7% to 4%, and after aging for 1 hour, the HER is almost 0 and the test piece failed in a similar way as those with a 610°C coiling temperature, indicating that the precipitation strengthening can cause damage to the HER.

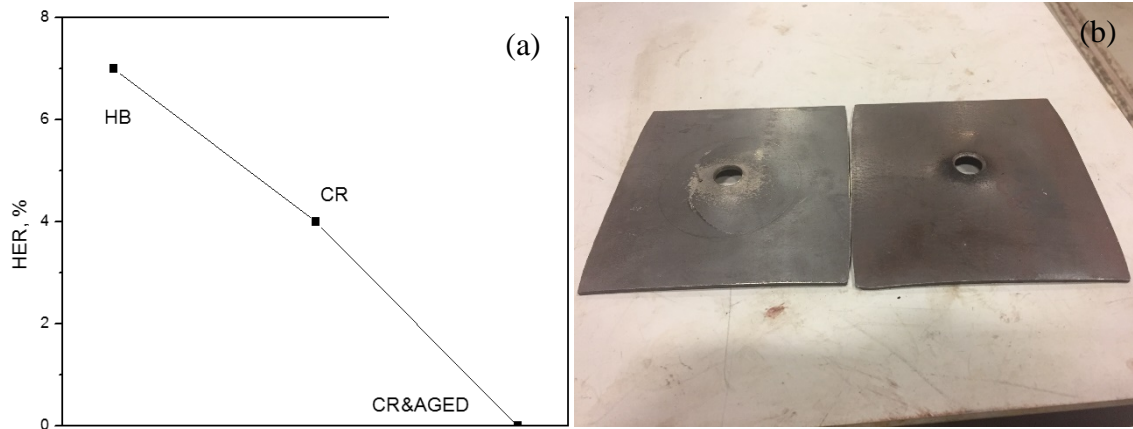


Figure 6.31: (a) HER of the hot band coil, cold rolled piece and cold rolled and aged piece; (b) Optical pictures of the hole expansion specimens after test

6.3 EFFECT OF TIN PARTICLES ON THE MECHANICAL PROPERTIES OF THE STEELS

The adding of Ti plays an important role in grain refinement and/or precipitation strengthening, and controls the sulfide shape ^[31, 169, 170]. Ti is a strong nitride-forming element and can easily combine with nitrogen and form TiN. As the solubility of the TiN particles is very low in the austenite region, thus, during isothermal holding at high temperature, a thermally stable TiN can effectively pin the prior austenitic grain boundaries, prevent the prior austenite grains from growing coarsely and thus improve the toughness. However, those TiN inclusions can also act as initiation sites for cleavage. In order to have the most pinning effective, TiN precipitates distribution should have the largest volume fraction and smallest particle size possible.

In a Ti microalloyed steels, Ti nitrides or Ti carbonitrides can occur at several stages of the manufacturing process and can be divided into three catalogs. The first type of precipitates can form prior to, during and immediately after solidification, depositing in the liquid, on the

liquid/solid phase boundaries and inter-dendritic regions between the δ -Fe dendrites. These precipitates cannot be re-dissolved in austenite during reheating, their size is too large and their distribution is too sparse, and they cannot retard the recrystallization of the deformed austenite. The second type of precipitates can form during the solidification and subsequent hot deforming in the austenite, the refinement of the microstructures of the HSLA steels is obtained through the interaction of this types of precipitates and the recrystallization process during controlled rolling. The last type of precipitates are formed during or after austenite-ferrite transformation, making a big contribution to the strength of the steels. TiN can be found in all conditions based on the segregation tendencies of Ti and N, except for the cleanest liquid^[171].

It is usually suggested that a lower Ti/N ratio value is desired to have a better toughness. The stoichiometric ratio of Ti to N is about 3.42, and in this study, the ratio of Ti to N is 27.2. Of course, extra Ti content is needed for other purpose like tying up C. However, a high Ti content tends to form coarser TiN particles, and those big particles no longer hold the effect to pin the prior austenite grain boundaries, instead, they could impair the toughness.

The solubility product of TiN in austenite is given by Inoue et al. shown in Equation 6.10^[172, 173]:

$$\log ([Ti][N])_{\gamma}=4.35-14890/T \quad (6.10)$$

where [Ti] and [N] are the Ti and N contents dissolved in the steel and T is the temperature.

If it is assumed that all the titanium and nitrogen were dissolved in the steel, then from Table 4.1, it can be known that there has 0.163 wt% Ti and 0.006% N in the steels. Then taking the [Ti] as 0.163 and [N] as 0.006, the initial TiN formation temperature was calculated to be 2026K (1753°C). However, from JMatPro calculation shown in Figure 6.32, the liquidus and solidus temperature for this chemistry should be 1510°C and 1458°C, so the TiN particles start to form

above the solidus temperature, which is out of the range of the application of Eq. 6.10. Therefore, in the liquid condition, Eq. 6.11^[174] can be used for calculation of solubility product of TiN.

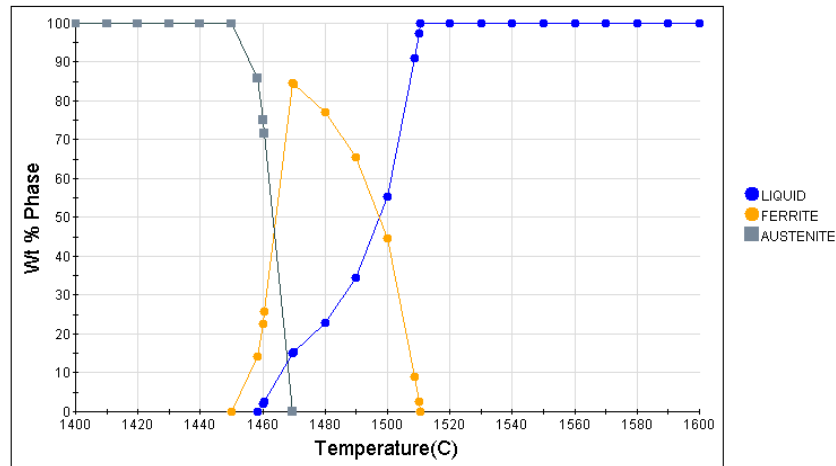


Figure 6.32: Phase diagram from JMatPro calculation

$$\log ([Ti][N])_l = 5.90 - 16586/T \quad (6.11)$$

If T is taken as 1783K (1510°C), then the product of [Ti] and [N] is 3.96×10^{-4} , as the precipitated TiN particles should match the stoichiometric ratio of Ti to N, Equations 6.12-6.14 should be applied, where k is the solubility product, and T_{tot} and N_{tot} is the total concentration of Ti and N, and the result is [Ti] = 0.151 and [N] = 0.0026, which means there are 0.151wt% of Ti and 0.0026wt% of N remained in the liquid. From Equation 6.15, the volume fraction of TiN precipitate at the liquidus temperature is 2×10^{-4} .

For inclusions formed above the solidus temperature, they would tend to grow to a larger size due to the rapid diffusion in the liquid and the size of them is not greatly affected by the cooling rate of the liquid steel. This results can be used as the total contents of Ti and N in the following calculation. During the solidification, a fast cooling rate is essential to refine the particles by causing them to form predominantly in the solid steel rather than liquid steel, as is the case for continuously casting. δ ferrite starts to form at 1510°C, and austenite starts to form at

1470°C and become fully austenitic phase at 1450°C. In order to calculate the solute Ti and N at reheating temperature and to simplify the situation, δ ferrite will not be included in the following calculation. And also assumed that 100% of liquid transform into 100% of austenite at 1450°C, and the result is shown in Table 6.7. From this table, it can be seen that at reheating temperature, nitrogen is almost depleted in the solution, which means there is no available nitrogen left to form nitride with elements other than Ti, such as V and Al. The whole calculation is based on the pre-assumption mentioned early in this paragraph. However, even if the δ ferrite was taken into account, because TiN has higher solubility in both liquid and austenite than in the ferrite, which means the precipitated TiN could be more and there actually would be even less solute Ti and N in the solution.

$$\frac{Ti_{tot}-[Ti]}{N_{tot}-[N]} = 3.42 \quad (6.12)$$

$$[N] = \frac{-(Ti_{tot}-3.42N_{tot})+\sqrt{(Ti_{tot}-3.42N_{tot})^2+4\times 3.42\times k}}{6.84} \quad (6.13)$$

$$[Ti] = \frac{(Ti_{tot}-3.42N_{tot})+\sqrt{(Ti_{tot}-3.42N_{tot})^2+4\times 3.42\times k}}{2} \quad (6.14)$$

$$f_V = \frac{(<Ti> + <N>)}{100} \cdot \frac{\rho_M}{\rho_{TiN}} \quad (6.15)$$

Table 6.7: Calculated volume fraction of TiN inclusions

| State | [Ti] | [N] | TiN |
|---------------------|-------|--------|--------|
| Liquid at 1510°C | 0.151 | 0.0026 | 2.0E-4 |
| Liquid at 1450°C | 0.146 | 0.0013 | 2.8E-4 |
| Austenite at 1450°C | 0.143 | 3.6E-4 | 3.3E-4 |
| Austenite at 1200°C | 0.142 | 1.2E-5 | 3.5E-4 |

From other researchers' work, coarse TiN particles (>0.5 microns) precipitate from liquid phase, and have little effect on strength as they do not prevent the grain growth. Fortunately, after solidification, there is still enough Ti to form fine Ti carbides precipitates in the solid phase which

hopefully, can prevent the coarsening of prior austenite grains and refine the microstructure. From the equations above, it can be seen that as the difference between Ti_{tot} and $3.42N_{tot}$ increases, which means the Ti/N ratio increases, the nitrogen remained in the solution is decreasing, and in order to keep the solubility product value constant, the titanium remained in the solution should be increasing, and as a result, a larger [Ti] would promote the coarsening rate for TiN.

Because of the heavily precipitated TiN inclusions from the hot band, it is necessary to check the slab which was hot rolled to form the 3mm plates in this study.

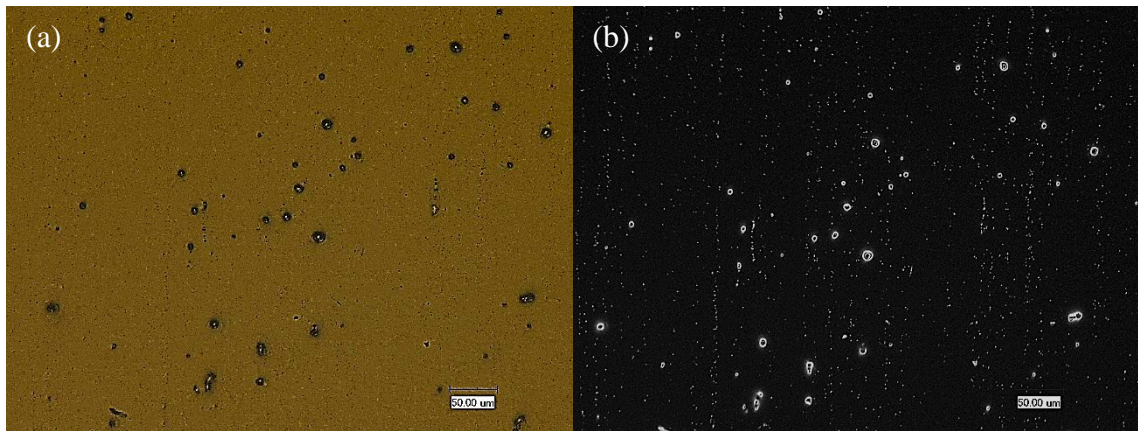


Figure 6.33: Comparison of optical micrograph in (a) bright field and (b) dark field

Figure 6.33 shows bright field and dark field OMs at the same spot. It can be seen that under the dark field, those inclusions can turn into bright dots with a black background of matrix, thus gives a better contrast of the particles and easier to analyze quantitatively and qualitatively. Figure 6.34 shows the dark field OM of both slab of one of the hot bands, it shows that in the slab, all inclusions, no matter what size they have, distributed in a random fashion; however, in the hot band, all the inclusions were lined up along the rolling direction. Higher magnification SEM of the inclusions in the slab and hot band can be seen in Figures 6.35 and 6.36. Overall, they all have very considerable amount of particles. From SEM and EDAX results, it can be confirmed that the larger

inclusion is TiN, with a particle size ranging from 2 to 5 microns and the smaller inclusion is (Ti, Mo, V)C with hundreds of nanometers in size, and this result is consistent with the SEM/EDAX results that was observed before. Those carbides inclusions were possibly formed before or during hot rolling by precipitating on the boundaries of the deformed prior austenite grains. This is because the mean distance between the fine inclusion bands is close to the width of the prior austenite grains.

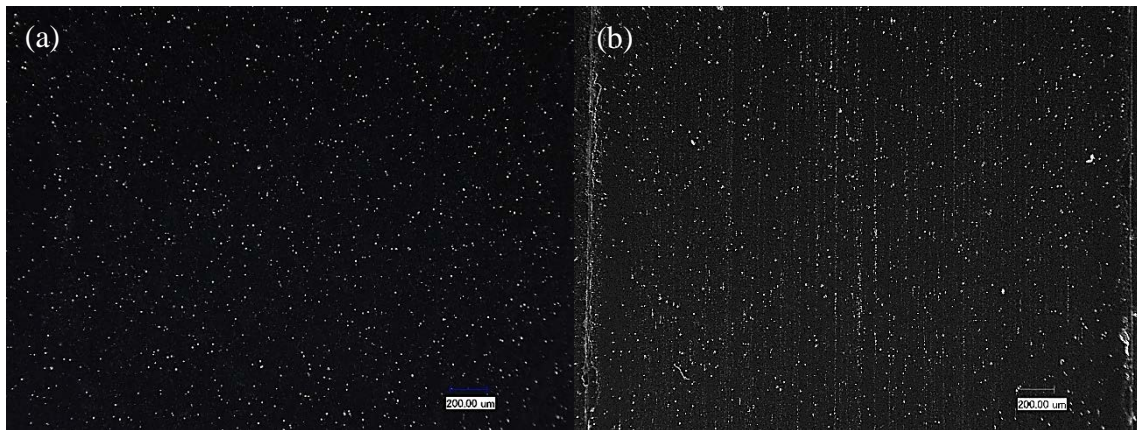


Figure 6.34: Dark field optical micrograph of (a) slab; (b) hot band steel

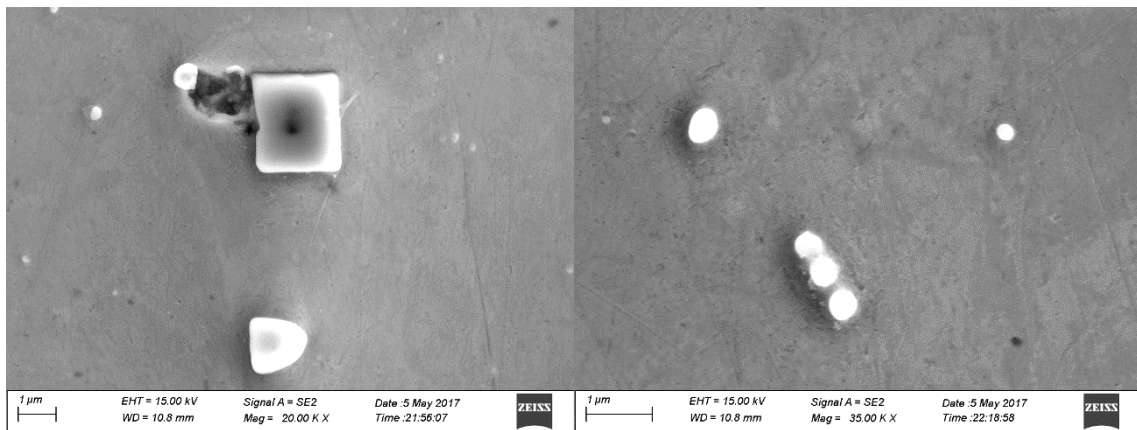


Figure 6.35: SEM micrographs of inclusions in the slab

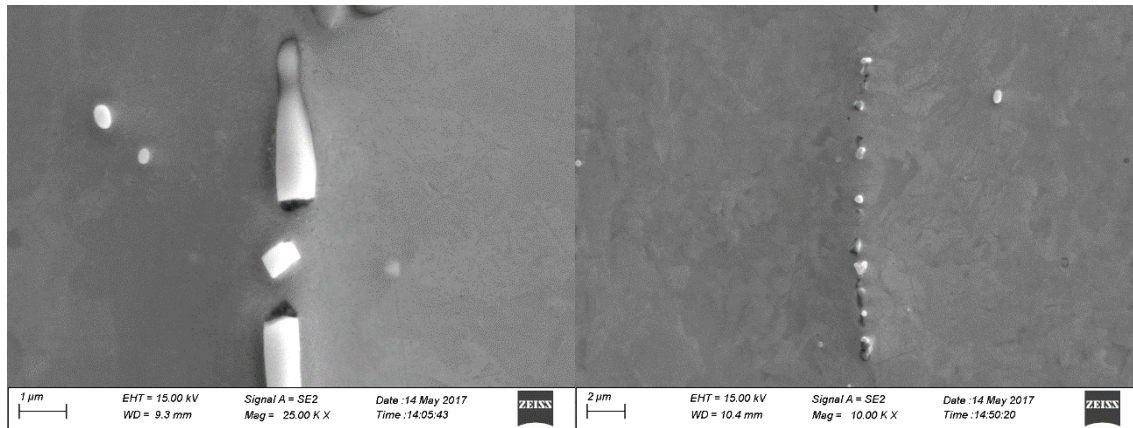


Figure 6.36: SEM micrographs of inclusions in the hot band

From the discussion above, it can be known that because of the high value of solubility product of Ti and N, there is a considerable amount of TiN inclusions, also due to the hyper-stoichiometric ratio between the Ti and N, the inclusions formed in the liquids can end up with a coarse size. No beneficial effects can be obtained from those huge particles, instead, they can be very detrimental to the mechanical properties. Figure 6.37 shows the TiN inclusions found on the fracture surface after the specimens were tested. The influence of TiN on the ductility is minimum, however, they can significantly reduce the toughness a lot. Figure 6.38 is a contour map of Charpy transition temperature with different combination of Ti and N^[175]. It can be seen that the transition temperature is the lowest when the Ti/N ratio is about 3.4 (stoichiometric), and it increases gradually with the departure from the value of 3.4.

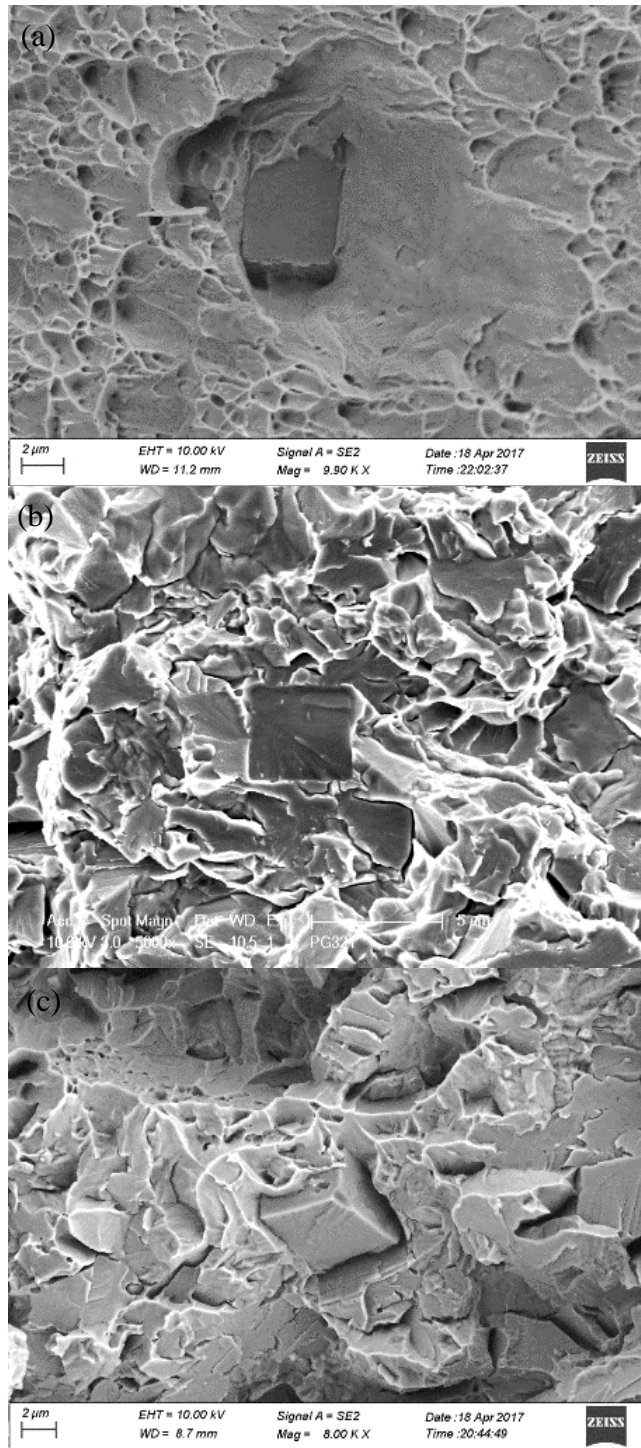


Figure 6.37: SEM micrographs of TiN inclusions on the fracture surface of (a) tensile specimen; (b) Charpy specimen; (c) hole expansion specimen

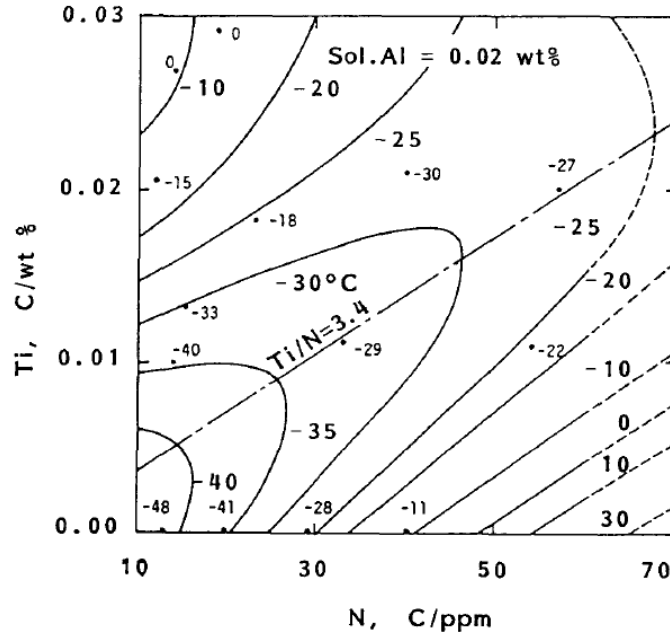


Figure 6.38: Contour map of Charpy transition temperature obtained by the polynomial expression in steel with 0.02wt% Sol.Al

Moreover, many studies showed that when the steels have the same microstructure and fine prior austenite grains, coarse TiN can cause cleavage fracture^[176]. In the impact test, the specimens were fractured at -40°C, the thermal expansion coefficient of the matrix is about $12 \times 10^{-6} \text{ } ^\circ\text{C}^{-1}$ and for TiN particles, the thermal expansion coefficient is $7 \times 10^{-6} \text{ } ^\circ\text{C}^{-1}$. Due to this thermal dilation difference between the TiN and the ferritic matrix, a large mismatch tension stress can be generated. Fairchild et al. found that the tension stress can be the driving force causing the TiN particles to crack and trigger the cleavage fracture^[177]. At lower test temperature, the stress can increase due to the differential contraction. And because TiN is very brittle, so only a small amount of energy needed combined with tension stress to crack the TiN from the matrix, and the larger the TiN inclusions, the easier they will crack.

Fracture toughness, as an inherent property, can also be affected by the existence of the TiN inclusions. From the work of Jing-Yuan Li et al.^[178], it was found that the fracture toughness

K_{IC} is influenced by the volume fraction, spacing and size of TiN inclusions. From Figure 6.39(a), it can be seen that the K_{IC} decreases in a linear relationship with the f_v when f_v is less than 0.1%. As for the inclusion spacing, from Figure 6.39(b), K_{IC} shows a linear relationship with the square root of spacing. Figure 6.40 shows the relationship between the fracture toughness and the allowable stress and crack size^[80], it can be seen at the same stress level, a material with a higher fracture toughness can survive with a larger critical crack size.

Besides that, the size of the TiN inclusion can affect the true fracture strain, and the relationship between the fracture toughness and the true fracture strain is shown in Equation 6.16:

$$J_{IC} = \sigma_0 \varepsilon_f l_0 \quad (6.16)$$

where σ_0 is the yield strength, ε_f is the true fracture strain and l_0 is the spacing between the microvoids ahead of the crack^[80]. It can be seen that a larger size of TiN can reduce the true fracture strain, and lower fracture strain leads to a lower fracture toughness. Therefore, the larger the size, the smaller strains it requires to accomplish fracture. To summarize, higher the volume fractions, smaller spacings and larger inclusion sizes of TiN can the lower the fracture toughness.

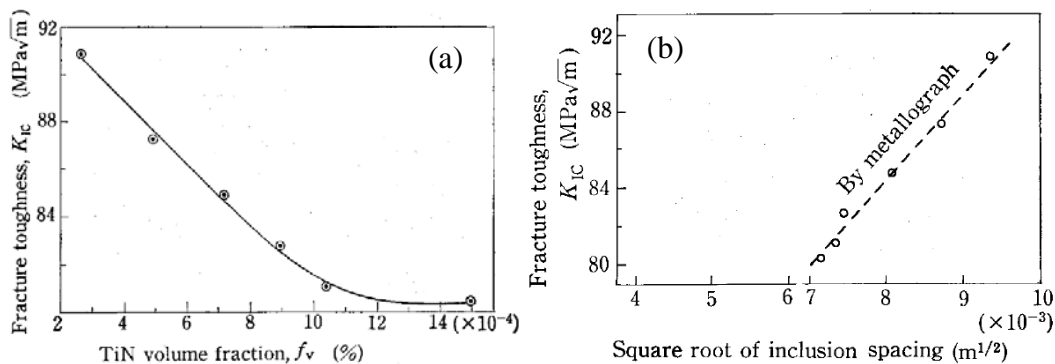


Figure 6.39: Influence of (a) TiN volume fraction and (b) TiN spacing on the fracture toughness

In these studied steels, TiN inclusions were most likely formed at higher temperature before being finish rolled, so they will have similar distribution features. And the existence of

coarse TiN inclusions will bring down the fracture toughness. From Figure 6.40, it can be seen that a material with a lower K_{Ic} , if a same stress load was applied, the allowed crack length should be much smaller.

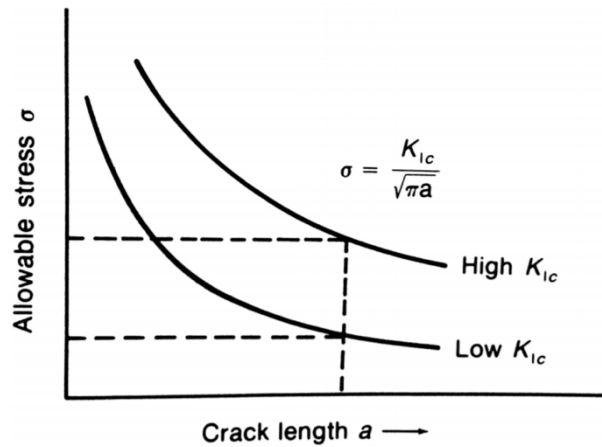


Figure 6.40: Relationship between fracture toughness and allowable stress and crack size

6.4 PRECIPITATION STRENGTHENING STUDY

During the cooling process, two types of precipitates formed. One is from the phase transformation of austenite to ferrite. Due to the difference in the crystal structure, the solubility of carbides in the two phases are quite different. And the lower solubility of ferrite will cause precipitates to form which were in the solid solution of austenite. Another type of precipitates is formed during isothermal holding or slow cooling at lower temperature from the supersaturated matrix.

From solubility calculation, it is known that all the N has already been consumed to form TiN at higher temperature. But, there is still a large amount of Ti left in the solid solution, and it can combine with carbon and precipitates out in the deformed austenite during hot rolling or in the ferrite during coiling in the form of fine dispersed TiC or (Ti, M)C particles.

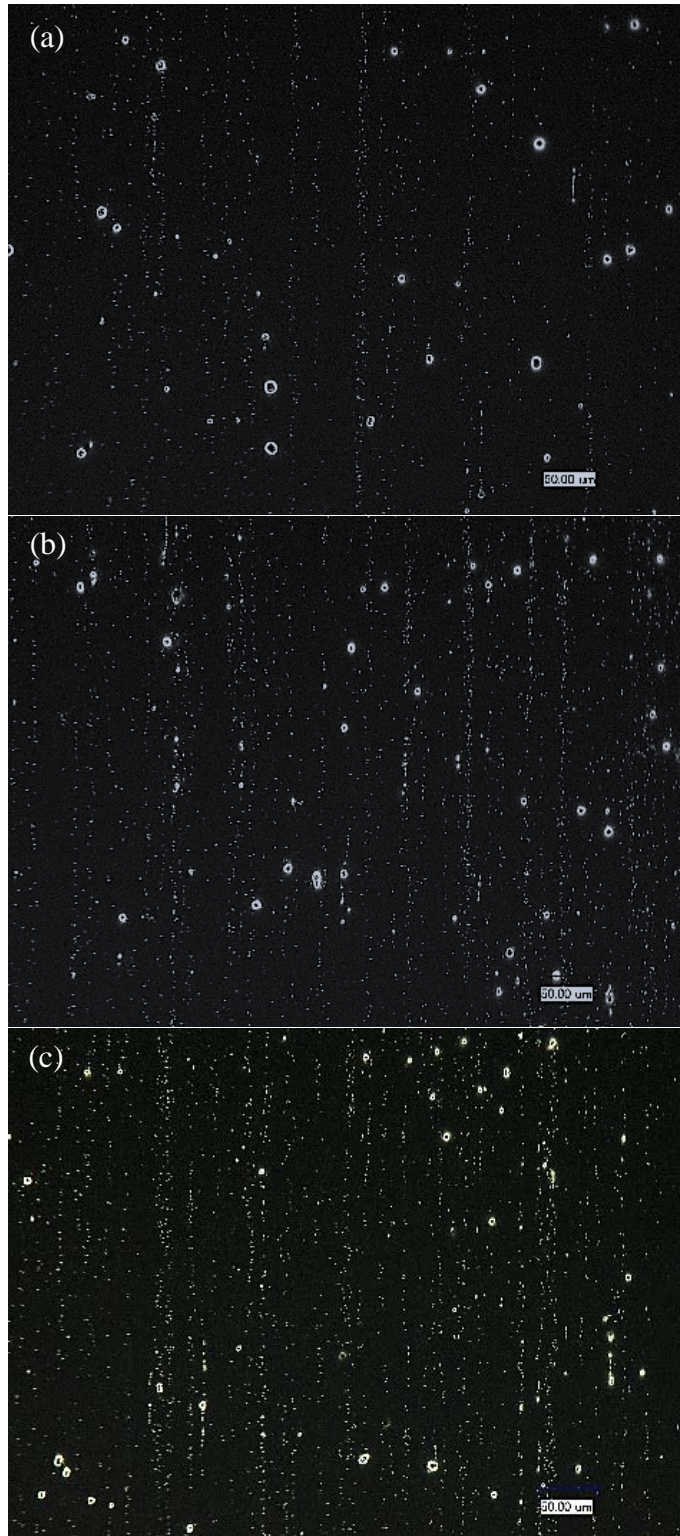


Figure 6.41: Dark field OM of steels with a coiling temperature of 610°C and finish rolling temperature of (a) 870°C; (b) 810°C; (c) 750°C

Figure 6.41 shows the distribution of inclusions at different finish rolling temperatures and the same coiling temperature of 610°C. From the last section, it is known that the big dots are TiN and the small dots are (Ti, Mo, V)C. It appears that as the finish rolling temperature decreases, there are more carbides formed. Those carbides were formed before entering into the coiling process, during hot deformation. However, those particles can have limited strengthening effect because of the increased amount of the incoherent particles with the matrix ferrite due to the coarsening.

For the TEM observation, carbon extraction replicas were prepared to investigate the precipitates in the steels. Figure 6.42 is the TEM results of a condition with a finish rolling temperature of 870°C and a coiling temperature of 610°C at different magnifications. From them, it can be seen that two sizes of precipitates can be found, one group with a size about 200 to 500 nm and the other with a size about 10 nm. From EDAX results, it can be seen that those precipitates both are (Ti, Mo, V)C carbides.

From the previous discussion, it is known that the high strength of the steels with a coiling temperature of 610°C is coming from the precipitates formed during coil cooling. And because of the lower coiling temperatures, steels with coiling temperatures of 530°C and 450°C did not have a sufficient amount of fine precipitates to strengthen the matrix which is proved by the cold rolling and aging experiment. Figure 6.43 shows the precipitates distribution of steels with different coiling temperatures in the TEM. It is obviously that the steels with a coiling temperature of 610°C show large volume fraction of fine precipitates, and in the steel with a coiling temperature of 450°C, there are not many precipitates on the carbon replicas. The volume fraction of those precipitates under different coiling temperatures were shown in Table 6.8. The data are consistent

with the JMatPro simulation results. Those precipitates were formed during the slow furnace cooling which is a simulation of the coiling process.

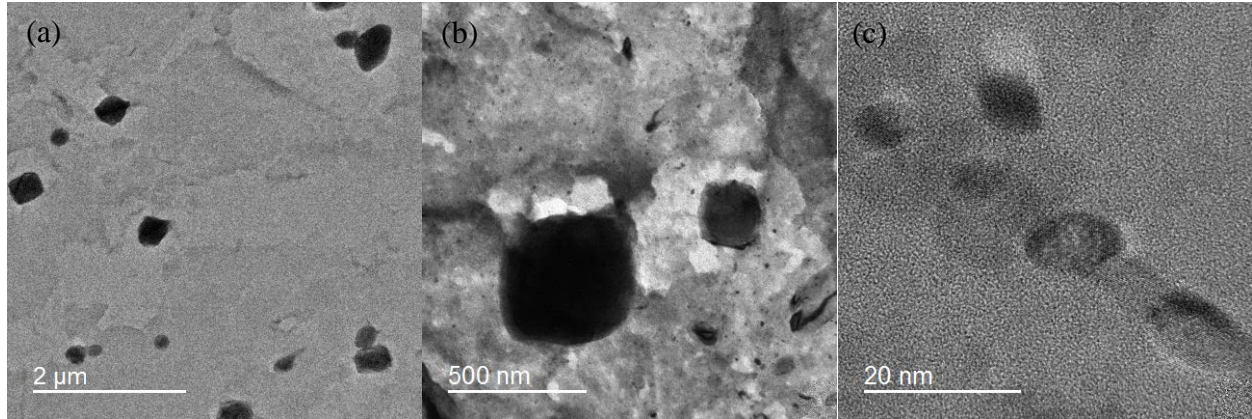


Figure 6.42: TEM micrograph of carbon replica of a steel with finish rolling temperature of 870°C and coiling temperature of 610°C at different magnifications

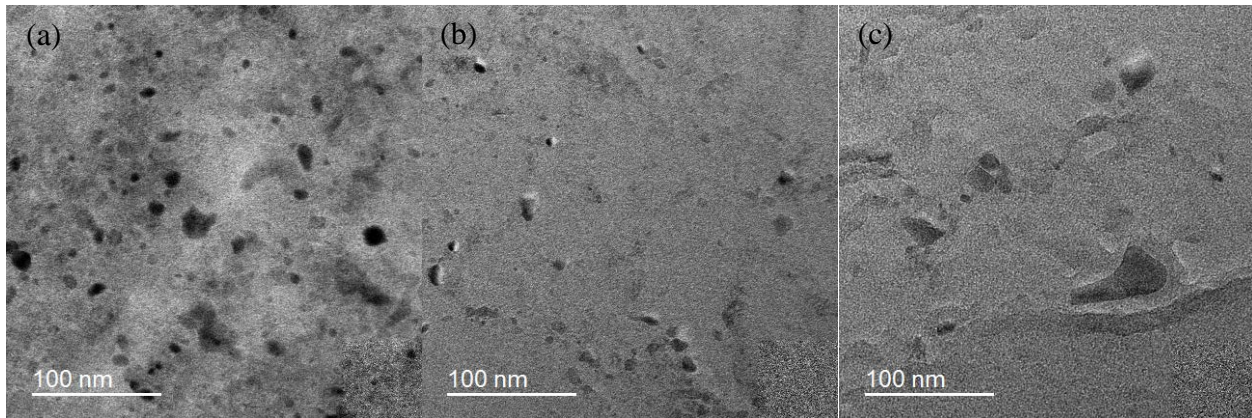


Figure 6.43: TEM carbon replica of precipitates in steel with a coiling temperature of (a) 610°C; (b) 530°C; (c) 450°C

Table 6.8: Volume fraction of precipitates during hot rolling with different CT (FRT 870°C)

| CT | 610°C | 530°C | 450°C |
|-------|-------|-------|-------|
| f_v | 4.6% | 2% | 0.3% |

7.0 CONCLUSION

This study is focusing on the development of a hot band steel with a good combination of strength, ductility and toughness by using conventional hot rolling process. The rolling parameters and chemical composition was designed and controlled in order to have the best result. The ideal steel should have a ductile uniform matrix microstructure with precipitates formed during phase transformation and coiling cooling. There have several factors needed to be considered in order to realize it, e.g., the austenite conditioning, the finish rolling temperature, the rolling strain, the coiling temperature, the cooling rate, etc. However, in this study, only the finish rolling temperature and coiling temperature have been discussed in detail, and the relationship to the corresponding mechanical properties have been analyzed. It was found that the finish rolling temperature didn't have much effect on the microstructures or the mechanical properties, whereas, the coiling temperature can make a significant change in the microstructures and corresponded mechanical properties. The difference in the tensile strength, toughness and hole expansion ratio is a result of microstructure change (ferrite or bainite) and precipitation strengthening behavior. Besides, inclusions of TiN were found to have a big influence on the toughness or hole expansion results. The main conclusions have been drawn and will be given in the following part.

1. Finish rolling in the temperature range below recrystallization temperature resulted in deformed prior austenite grains with a high S_v value, and it didn't have much effect on the grain size of the ferrite, and the microstructure did not change as finish rolling temperature differs. However, the

microstructure varies a lot with different coiling temperatures. The microstructure of steel at the coiling temperature of 610°C is mixed with equiaxed ferrite and acicular ferrite grains, and the microstructure of the steel at the coiling temperature of 530°C is granular bainite, ferritic matrix with martensite and retained austenite (M/A) constituents dispersed within it and coarse quasi-polygonal ferrite. As the coiling temperature dropped to 450°C, microstructure is very similar except more quasi-polygonal ferrite can be found and upper bainite start to appear. The appearance of large quasi-polygonal ferrite can be harmful to the toughness.

2. M/A can be seen in the steels with lower coiling temperatures. The M/A islands were small and carbides were distributed uniformly in the steels with a coiling temperature of 530°C, however, in the steels with a coiling temperature of 450°C, more and coarser M/A islands appeared, carbides became more segregated which could be detrimental to the toughness.

3. The steels with a coiling temperature of 610°C have a higher fraction of high angle grain boundaries with a misorientation angle between 20° to 50° due to the formation of equiaxed ferrite grains. And the steels with lower coiling temperatures have a higher fraction of low angle grain boundaries and high angle grain boundaries with a misorientation around 60°, which is a result of the formation of low temperature products like bainite, quasi-polygonal ferrite. A high fraction of HAGB is beneficial to the toughness and a high fraction of LAGB can contribute to the strength.

4. Steels with a coiling temperature of 610°C shows the highest strength, worst toughness and hole expansion ratio. Steels with a coiling temperature of 530°C show the lowest strength, best toughness and hole expansion ratio. Steels with a coiling temperature of 450°C show an intermediate mechanical properties. Highest strength in the steels with highest coiling temperature comes from the 10nm (Ti, Mo, V)C precipitates formed during coiling process, the coiling temperature of 610°C is high enough to provide sufficient driving force for the precipitation to

complete thoroughly. While after slow cooling from temperatures of 530°C and 450°C, there was still considerable amount of solutes left in the supersaturated solid solution which cannot form precipitates to provide strengthening to the steel. While the coarser (Ti, Mo, V)C precipitates with a size from 200nm to 500nm formed during the hot deformation will not have a significant effect on the strength. The dislocation density increase as the coiling temperature decreases. The higher strength of the steels with the lowest coiling temperature is due to the higher dislocation density coming from bainite or quasi-polygonal ferrite grains.

5. The low toughness and hole expansion ratio in the steels with a coiling temperature of 610°C is caused by the excessively formed precipitates at a large extent. A fine grain microstructure can increase the toughness of steels with lower coiling temperatures. The formation of M/A constituents can be harmful to the toughness.

6. The low toughness and hole expansion ratio can be also related to the inclusions. Those inclusions can be an initiation point to the cleavage fracture to occur. The high content Ti and low content of N with a hyper-stoichiometric ratio between the Ti and N cause TiN formed in the liquid and interdendritic regions between the δ -Fe dendrites, resulted in high volume fraction of TiN inclusions with a size several microns. The tension stress caused by the different thermal expansion coefficient can crack the TiN and matrix easily with a little extra energy. And the fracture toughness can be lowered with the appearance of large TiN inclusions which can cause the high strength steel more sensitive to the micro-cracks inside it.

8.0 FUTURE WORK

In this current study, it is able to produce single-phase ferritic steels through a conventional hot strip mill processing with a tensile strength over 1200MPa, yield strength over 1000MPa and total elongation around 20% at a coiling temperature of 610°C, but their toughness and hole expansion value are very low, in order to improve the these mechanical properties, several suggestions were made for the further work:

1: Since the low toughness and low hole expansion ratio were partially caused by the excessively formed precipitates during the hot deformation and coiling process, the precipitates formed during hot deformation can act as the initiation points to facilitate the brittle fracture and they do not contribute to the strength of the steels too much. Thus, it is necessary to reduce the volume fraction of those particles. One possible approach is to raise the deformation temperature, because with a higher finish rolling temperature, more carbides will remain in the solid solution. However, this will result in even more fine precipitates formed during coiling and cause lower toughness and HER.

2: In order to improve the toughness and HER, it is necessary to reduce the volume fraction of fine precipitates during coiling process. Increasing the coiling temperature is an option, by that, the driving force to form precipitates will be lower, and the solubility of the carbides is higher. However, there is a risk to lose too much strength of the steel. Therefore, more experiments and tests need to be done in the further.

3: A better toughness and HER value generally comes with a steel with a finer microstructure. A higher roughing strain and more grain refinement can result in a higher Sv value which would result in a finer microstructure.

4: The steel used in this study has a very high concentration of Ti and low concentration of N, which results in a high volume fraction of coarse TiN. In order to prove the toughness and HER, the N concentration should be further lowered to reduce the volume fraction of TiN, since most of the strengthening particles are carbides.

5: Since martensite/austenite constituents were able to have negative effect on the toughness, so reduce the volume fraction and size of M/A particles is important. Elements like C, Mo, Mn can increase the formation of M/A. Thus, reducing the concentration of them can decrease the volume fraction of M/A. Besides that, a proper combination of transformation temperature and cooling rates can also result in less and finer M/A constituents.

BIBLIOGRAPHY

- [1] M. Rashid, "High-strength, low-alloy steels," *Science*, vol. 208, pp. 862-869, 1980.
- [2] M. Cohen and W. S. Owen, "Microalloying 75," in *Proceedings*, 1977, p. 2.
- [3] S. Keeler, "Advanced high strength steel (AHSS) application guidelines," *AHSS-World Auto Steel*, versão, vol. 4, 2009.
- [4] R. Kuziak, R. Kawalla, and S. Waengler, "Advanced high strength steels for automotive industry," *Archives of civil and mechanical engineering*, vol. 8, pp. 103-117, 2008.
- [5] S. Dinda and R. Diaz, "The partnership for a new generation of vehicles (PNGV) and its impact on body engineering," *Proc. IBEC 95, Advanced Technologies and Processes*, vol. 5, 1995.
- [6] A. Jambor and M. Beyer, "New cars—new materials," *Materials & design*, vol. 18, pp. 203-209, 1997.
- [7] T. Senuma, "Physical metallurgy of modern high strength steel sheets," *ISIJ international*, vol. 41, pp. 520-532, 2001.
- [8] B. K. Zuidema, S. G. Denner, B. Engl, and J.-O. Sperle, "New high strength steels applied to the body structure of ULSAB-AVC," *SAE Technical Paper 0148-7191*, 2001.
- [9] L. Xu, F. Barlat, M. Lee, K. Choi, and X. Sun, "Hole expansion of dual phase steels," *WIT Transactions on The Built Environment*, vol. 124, pp. 75-83, 2012.
- [10] G. E. Totten, L. Xie, and K. Funatani, *Handbook of mechanical alloy design* vol. 164: CRC press, 2003.
- [11] P. Åkerström, "Modelling and simulation of hot stamping," *Luleå tekniska universitet/Tillämpad fysik, maskin-och materialteknik/Hållfasthetslära*, 2006.
- [12] H. Karbasian and A. E. Tekkaya, "A review on hot stamping," *Journal of Materials Processing Technology*, vol. 210, pp. 2103-2118, 2010.

- [13] D. W. Fan, H. S. Kim, and B. C. De Cooman, "A review of the physical metallurgy related to the hot press forming of advanced high strength steel," *Steel Research International*, vol. 80, pp. 241-248, 2009.
- [14] T. Shimizu, Y. Funakawa, and S. Kaneko, "High Strength Steel Sheets for Automobile Suspension and Chassis Use High Strength Hot-Rolled Steel Sheets with Excellent Press Formability and Durability for Critical Safety Parts," JFE technical report, vol. 4, pp. 25-30, 2004.
- [15] A. B. Rolf Arjan Rijkenberg, Paul Bellina, Chris Wooffindin, "Advanced High Stretch-Flange Formability Steels for Chassis & Suspension Applications," presented at the Steels in Cars and Trucks 2014 (SCT2014), Braunschweig, Germany, 2014.
- [16] N. K. M. Morita, S. Masui, T. Kato, T. Higashino and N. and Aoyagi, *CAMP-ISIJ*, vol. 5, p. 1863, 1992.
- [17] N. Kim, A. Yang, and G. Thomas, "Effect of finish rolling temperature on the structure and properties of directly quenched nb containing low carbon steel," *Metallurgical and Materials Transactions A*, vol. 16, pp. 471-474, 1985.
- [18] M. Mekkawy and K. El-Fawakhry, "Effect of Finish-Rolling Temperature on Microstructure and Strength of Vanadium- and Titanium-Microalloyed Steels," *Scandinavian Journal of Metallurgy*, vol. 19, pp. 246-256, 1990.
- [19] V. Pogorzelskyj, Y. Matrosov, and A. Nasibov, "Controlled Rolling of Micro-Alloyed Steels," in *Proc. Conf. on Microalloying 75*, 1977, 100-106, 1977.
- [20] W. Choo, "New challenge to develop ultra fine grain steel with 1 μ m grain size," *Journal of the Korean Institute of Metals and Materials(South Korea)*, vol. 36, pp. 1945-1958, 1998.
- [21] S. Zajac, T. Siwecki, B. Hutchinson, and M. Attlegård, "Recrystallization controlled rolling and accelerated cooling for high strength and toughness in V-Ti-N steels," *Metallurgical and Materials Transactions A*, vol. 22, pp. 2681-2694, 1991.
- [22] T. Abe, K. Tsukada, and I. Kozasu, "Mechanism of Ferrite Grain Refinement in Low Carbon Steel in the Case of Accelerated Cooling After Controlled Rolling," *Tetsu-to-Hagane(J. Iron Steel Inst. Jpn.)*, vol. 74, pp. 505-512, 1988.
- [23] T. Siwecki, B. Hutchinson, and S. Zajac, "Recrystallization controlled rolling of HSLA steels," in *International conference microalloying*, 1995, pp. 197-211.
- [24] Y. H. Bae, J. S. Lee, J.-K. Choi, W.-Y. Choo, and S. H. Hong, "Effects of austenite conditioning on austenite/ferrite phase transformation of HSLA steel," *Materials Transactions*, vol. 45, pp. 137-142, 2004.
- [25] V. Pogorzelskyj, Y. J. Matrosov, and A. Nashilov, "Microalloying'75," in *Proc. Intl. Symp.*, Washington DC, 1975, p. 100.

- [26] Y.-Z. Zheng, A. DeArdo, R. M. Fix, and G. Fitzsimons, "Achieving Grain Refinement Through Recrystallization-Controlled Rolling and Controlled Cooling in V--Ti--N Microalloyed Steels," *HSLA Steels, Technology and Applications*, pp. 85-94, 1983.
- [27] L. Cuddy, "The effect of microalloy concentration on the recrystallization of austenite during hot deformation," *The Metallurgical Society/AIME*, pp. 129-140, 1982.
- [28] S. Yamamoto, C. Ouchi, and T. Osuka, "The effect of microalloying elements on the recovery and recrystallization in deformed austenite," *Thermomechanical Processing of Microalloyed Austenite*, pp. 613-639, 1981.
- [29] T. Tanaka, "Science and technology of hot rolling process of steel," in *Proceedings of the International Conference Microalloyed*, 1995, pp. 165-181.
- [30] I. Kozasu, C. Ouchi, T. Sampei, and T. Okita, "Hot rolling as a high-temperature thermo-mechanical process," in *Proc. Conf. on Microalloying 75*, 1977, 120-125, 1977.
- [31] T. Siwecki, A. Sandberg, W. Roberts, and R. Lagneborg, "The influence of processing route and nitrogen content on microstructure development and precipitation hardening in vanadium-microalloyed HSLA-steels," *Thermomechanical Processing of Microalloyed Austenite*, pp. 163-194, 1981.
- [32] A. J. DeArdo, G. Ratz, and P. Wray, *Thermomechanical processing of microalloyed austenite: proceedings of the International Conference on the Thermomechanical Processing of Microalloyed Austenite: Metallurgical Society of AIME*, 1982.
- [33] C. Mackenzie and R. Young, "METHOD FOR THE MEASUREMENT OF THE PHASE-TRANSFORMATION TEMPERATURE IN STEEL DURING COOLING AFTER ROLLING," *J IRON STEEL INST*, vol. 209, pp. 918-920, 1971.
- [34] M. Economopoulos, N. Lambert, and L. Habraken, *Diagrammes de transformation des aciers fabriques dans le Benelux: Centre National de Recherhces Metallurgiques*, 1967.
- [35] Y. Smith and C. Siebert, "Continuous cooling transformation kinetics of thermomechanically worked low-carbon austenite," *Metallurgical and Materials Transactions B*, vol. 2, pp. 1711-1725, 1971.
- [36] W. Lehnert and K.-A. Behr, "EFFECT OF DEFORMATION ON THE KINETICS OF AUSTENITE TRANSFORMATION," *Neue Hutte*, vol. 15, pp. 355-35, 1970.
- [37] S. SEKINO and S. TAMUKAI, "Behaviours of Recrystallization and Transformation Observed by Hot-Rolling of Nb-containing Steels," *Tetsu-to-Hagane*, vol. 58, pp. 1044-1053, 1972.
- [38] M. Fukuda, T. Hashimoto, and K. Kunishige, "Effects of Controlled Rolling and Micro-Alloying on Properties of Strips and Plates," in *Proc. Conf. on Microalloying 75*, 1977, 136-150, 1977.

- [39] B. Bramfitt and J. Speer, "A perspective on the morphology of bainite," Metallurgical transactions A, vol. 21, pp. 817-829, 1990.
- [40] E. Davenport, "u. EC Bain: Trans. Amer. Inst. min. metallurg. Engr," Iron Steel Div, pp. 117-144, 1930.
- [41] R. Mehl, "Hardenability of alloy steels," ASM, Metals Park, OH, vol. 1, 1939.
- [42] R. Hehemann, K. Kinsman, and H. Aaronson, "A debate on the bainite reaction," Metallurgical Transactions, vol. 3, pp. 1077-1094, 1972.
- [43] J. Christian and D. Edmonds, "Phase Transformations in Ferrous Alloys," TMS-AIME, Warrendale, PA, p. 293, 1984.
- [44] Y. Ohmori, H. Ohtani, and T. Kunitake, "Bainite in Low-Carbon Low-Alloy High-Strength Steels," TRANS IRON STEEL INST JAP, vol. 11, pp. 250-259, 1971.
- [45] H. K. D. H. Bhadeshia and I. O. Materials, Bainite in steels: Inst. of Metals, 1992.
- [46] J. Reynolds, WT, H. Aaronson, and G. Spanos, "A summary of the present diffusionist views on bainite," Materials Transactions, JIM, vol. 32, pp. 737-746, 1991.
- [47] J. Speer, A. Streicher, D. Matlock, F. Rizzo, G. Krauss, E. B. Damm, et al., "Austenite formation and decomposition," ISS/TMS, Warrendale, PA, pp. 505-522, 2003.
- [48] W. Steven and A. Haynes, "The temperature of formation of martensite and bainite in low-alloy steels," Journal of the Iron and Steel Institute, vol. 183, pp. 349-359, 1956.
- [49] T. Kunitake and Y. Okada, "The estimation of bainite transformation temperatures in steels by the empirical formulas," Tetsu-to-Hagane(Journal of the Iron and Steel Institute of Japan)(Japan), vol. 84, pp. 137-141, 1998.
- [50] J. Kirkaldy and D. Venugopalan, "Phase Transformations in Ferrous Alloys, ed. by AR Marder and JI Goldstein," TMS-AIME, Warrendale, PA, vol. 125, 1984.
- [51] H. Bhadeshia and R. Honeycombe, "Steels: microstructure and properties. 2006," BH Pub, pp. 42-44.
- [52] G. Krauss, Steels: processing, structure, and performance: Asm International, 2015.
- [53] H. Bhadeshia, "The lower bainite transformation and the significance of carbide precipitation," Acta metallurgica, vol. 28, pp. 1103-1114, 1980.
- [54] B. Josefsson, H. Andren, S. David, and J. Vitek, "Recent Trends in Welding Science and Technology," ASM Inst., OH, vol. 243, 1989.
- [55] L. Habraken, "Bainitic transformation of steels," Revue de Metallurgie, vol. 53, p. 930, 1956.

- [56] K. Ridal and J. McCann, "Physical Properties of Martensite and Bainite, Special Report 93," Iron and Steel Institute (London), pp. 147-148, 1965.
- [57] L. Habraken and M. Economopoulos, "Transformation and hardenability in steels," Ann Arbor, Mich.: Climax Molybdenum Co, p. 81, 1967.
- [58] X. Liang, "The complex phase transformation of austenite in high strength linepipe steels and its influence on the mechanical properties," University of Pittsburgh, 2012.
- [59] F. Matsuda, K. Ikeuchi, H. OKADA, I. HRIVNAK, and H.-S. PARK, "Effect of MA Constituent on Fracture Behavior of 780 and 980MPa Class HSLA Steels Subjected to Weld HAZ Thermal Cycles (Materials, Metallurgy & Weldability)," 1994.
- [60] F. Matsuda, K. IKEUCHI, Y. FUKADA, Y. HORII, H. OKADA, T. SHIWAKU, et al., "Review of mechanical and metallurgical investigations of MA constituent in welded joint in Japan," 1995.
- [61] S.-C. Wang and J.-R. Yang, "Effects of chemical composition, rolling and cooling conditions on the amount of martensite/austenite (M/A) constituent formation in low carbon bainitic steels," Materials Science and Engineering: A, vol. 154, pp. 43-49, 1992.
- [62] C. L and M. H, " The discussion of formation mechanism, metallurgical morphology and recognition proof of granular bainite," Transactions of Materials and Heat Treatment, vol. 1, p. 003, 1981.
- [63] M. Farooque and D. Edmonds, "XII Int. Cong. Electron Microscopy, Material Sciences," in Proc, 1990, p. 910.
- [64] T. NILAN, "Austenite Decomposition," in Transformation and hardenability in steels: symposium, 1967, p. 57.
- [65] J. Barford and W. Owen, "The effect of austenite grain size and temperature on the rate of bainite transformation," Met. Sci. Heat Treat. Met, vol. 4, pp. 359-360, 1961.
- [66] S.-J. Lee, J.-S. Park, and Y.-K. Lee, "Effect of austenite grain size on the transformation kinetics of upper and lower bainite in a low-alloy steel," Scripta Materialia, vol. 59, pp. 87-90, 2008.
- [67] P. Vasudevan, L. Graham, and H. Axon, "The kinetics of bainite formation in a plain carbon steel," JISI, vol. 12, p. 386, 1958.
- [68] R. Freiwilgig, J. Kudrman, and P. Chráska, "Bainite transformation in deformed austenite," Metallurgical Transactions A, vol. 7, pp. 1091-1097, 1976.
- [69] J. Wang, P. Van Der Wolk, and S. Van Der Zwaag, "On the influence of alloying elements on the bainite reaction in low alloy steels during continuous cooling," Journal of Materials Science, vol. 35, pp. 4393-4404, 2000.

- [70] J. Wang, P. J. v. d. Wolk, and S. v. d. Zwaag, "Effects of Carbon Concentration and Cooling Rate on Continuous Cooling Transformations Predicted by Artificial Neural Network," *ISIJ international*, vol. 39, pp. 1038-1046, 1999.
- [71] V. Biss and R. Cryderman, "Martensite and retained austenite in hot-rolled, low-carbon bainitic steels," *Metallurgical and Materials Transactions B*, vol. 2, pp. 2267-2276, 1971.
- [72] X. Li, Y. Fan, X. Ma, S. Subramanian, and C. Shang, "Influence of martensite–austenite constituents formed at different intercritical temperatures on toughness," *Materials & Design*, vol. 67, pp. 457-463, 2015.
- [73] C. Davis and J. King, "Cleavage initiation in the intercritically reheated coarse-grained heat-affected zone: Part I. Fractographic evidence," *Metallurgical and materials transactions A*, vol. 25, pp. 563-573, 1994.
- [74] Y. Li and T. Baker, "Effect of morphology of martensite–austenite phase on fracture of weld heat affected zone in vanadium and niobium microalloyed steels," *Materials Science and Technology*, vol. 26, pp. 1029-1040, 2010.
- [75] H. F. B. B, X. Z, Y. Z, X. Z and R. F, "The morphology and phase transformation of granular bainite," *Acta Metallurgica Sinica*, vol. 22, pp. 5-142, 1986.
- [76] E. Hall, "The deformation and ageing of mild steel: III discussion of results," *Proceedings of the Physical Society. Section B*, vol. 64, p. 747, 1951.
- [77] N. Hansen and B. Ralph, "The strain and grain size dependence of the flow stress of copper," *Acta Metallurgica*, vol. 30, pp. 411-417, 1982.
- [78] N. Petch, "The cleavage strength of polycrystals," *J. Iron Steel Inst.*, vol. 174, pp. 25-28, 1953.
- [79] H. Conrad, "On the mechanism of yielding and flow in iron," *Atomics International. Div. of North American Aviation, Inc., Canoga Park, Calif.* 1961.
- [80] G. E. Dieter and D. J. Bacon, *Mechanical metallurgy vol. 3: McGraw-Hill New York*, 1986.
- [81] F. B. Pickering, *Physical metallurgy and the design of steels: Applied Science Publishers*, 1978.
- [82] F. B. Pickering, "High strength low alloy steels," *Materials Science and Technology*, 2006.
- [83] R. W. Hertzberg, *Deformation and fracture mechanics of engineering materials: Wiley*, 1996.
- [84] A. Cottrell, "Report of a Conference on Strength of Solids," *Physical Society, London*, vol. 30, 1948.
- [85] F. Pickering, "The structure and properties of bainite in steels," 1967.

- [86] P. Kelly and J. Nutting, "The morphology of martensite," *J. Iron Steel Inst*, vol. 197, pp. 199-211, 1961.
- [87] H.-C. Chen and G.-H. Cheng, "Effect of martensite strength on the tensile strength of dual phase steels," *Journal of Materials Science*, vol. 24, pp. 1991-1994, 1989.
- [88] J. Hatch, "Aluminum Properties and Physical Metallurgy," American Society for Metals, Metals Park, OH, May 1984," ed: APPENDICES.
- [89] H. Gleiter and E. Hornbogen, "Precipitation hardening by coherent particles," *Materials Science and Engineering*, vol. 2, pp. 285-302, 1968.
- [90] E. Orowan, "Classification and nomenclature of internal stresses," *JOURNAL OF THE INSTITUTE OF METALS*, vol. 73, pp. 47-59, 1947.
- [91] E. Orowan, "Discussion in The Symposium on Internal Stresses in Metals and Alloys, Inst," *Metals*, London, vol. 451, 1948.
- [92] M. Gensamer, "General Survey of the Problem of Fatigue and Fracture," *Fatigue, and Fracture of Metals*, John Wiley & Sons, Inc., New York, 1952.
- [93] C. C. Crussard, J. Plateau, R. Tamhankar, G. Henry, and D. Lajeunesse, "A comparison of Ductile and Fatigue Fractures," in *ICF0*, Swampscott-MA (USA) 1959, 2012.
- [94] J. Gurland and J. Plateau, "The mechanism of ductile rupture of metals containing inclusions," *Brown Univ., Providence; Institut de Recherches de la Siderugie, St.-Germain-en-Laye, France* 1963.
- [95] D. François, A. Pineau, and A. Zaoui, *Mechanical Behaviour of Materials: Volume II: Fracture Mechanics and Damage* vol. 191: Springer Science & Business Media, 2012.
- [96] T. Gladman, B. Holmes, and I. McIvor, "Effect of second-phase particles on the mechanical properties of steel," *Iron and Steel Institute*, London, pp. 68-78, 1971.
- [97] K. Puttick, "Ductile fracture in metals," *Philosophical magazine*, vol. 4, pp. 964-969, 1959.
- [98] A. Argon, J. Im, and R. Safoglu, "Cavity formation from inclusions in ductile fracture," *Metallurgical Transactions A*, vol. 6, pp. 825-837, 1975.
- [99] A. Argon and J. Im, "Separation of second phase particles in spheroidized 1045 steel, Cu-0.6 pct Cr alloy, and maraging steel in plastic straining," *Metallurgical Transactions A*, vol. 6, pp. 839-851, 1975.
- [100] S. Goods and L. Brown, "Overview No. 1: The nucleation of cavities by plastic deformation," *Acta Metallurgica*, vol. 27, pp. 1-15, 1979.
- [101] J. Fisher and J. Gurland, "Void nucleation in spheroidized carbon steels part 1: experimental," *Metal Science*, vol. 15, pp. 185-192, 1981.

- [102] F. Beremin, "Cavity formation from inclusions in ductile fracture of A508 steel," *Metallurgical Transactions A*, vol. 12, pp. 723-731, 1981.
- [103] R. V. Stone, T. Cox, J. Low, and J. Psioda, "Microstructural aspects of fracture by dimpled rupture," *International Metals Reviews*, vol. 30, pp. 157-180, 1985.
- [104] T. Gladman, D. Dulieu, and I. D. McIvor, "Structure/property relationships in high-strength micro-alloyed steels," in *Proc. Conf. on Microalloying 75*, 1977, 32-55, 1977.
- [105] A. A. Benzerga, "Micromechanics of coalescence in ductile fracture," *Journal of the Mechanics and Physics of Solids*, vol. 50, pp. 1331-1362, 2002.
- [106] T. B. Cox and J. R. Low, "An investigation of the plastic fracture of AISI 4340 and 18 Nickel-200 grade maraging steels," *Metallurgical Transactions*, vol. 5, pp. 1457-1470, 1974.
- [107] J. Hodge, R. Frazier, and F. Boulger, "The effects of sulfur on the notch toughness of heat-treated steels," *TRANSACTIONS OF THE AMERICAN INSTITUTE OF MINING AND METALLURGICAL ENGINEERS*, vol. 215, pp. 745-753, 1959.
- [108] W. Baldwin and B. Edelson, "The effect of second phases on the mechanical properties of alloys," *ASM TRANS Q*, vol. 55, pp. 230-250, 1962.
- [109] A. Birkle, R. Wei, and G. Pellissier, "Analysis of Plane-Strain Fracture in a Series of 0.45 C-Ni-Cr-Mo Steels with Different Sulfur Contents," *ASM Trans Quart*, vol. 59, pp. 981-990, 1966.
- [110] N. Isasti, D. Jorge-Badiola, M. L. Taheri, and P. Uranga, "Microstructural Features Controlling Mechanical Properties in Nb-Mo Microalloyed Steels. Part II: Impact Toughness," *Metallurgical and Materials Transactions A*, vol. 45, pp. 4972-4982, 2014.
- [111] G. Larzabal, N. Isasti, J. M. Rodriguez-Ibabe, and P. Uranga, "Evaluating Strengthening and Impact Toughness Mechanisms for Ferritic and Bainitic Microstructures in Nb, Nb-Mo and Ti-Mo Microalloyed Steels," *Metals*, vol. 7, p. 65, 2017.
- [112] T. Hanamura, F. Yin, and K. Nagai, "Ductile-brittle transition temperature of ultrafine ferrite/cementite microstructure in a low carbon steel controlled by effective grain size," *ISIJ international*, vol. 44, pp. 610-617, 2004.
- [113] C. Wang, M. Wang, J. Shi, W. Hui, and H. Dong, "Effect of microstructural refinement on the toughness of low carbon martensitic steel," *Scripta Materialia*, vol. 58, pp. 492-495, 2008.
- [114] A. Norma, "E92-82 (1997) E3 Standard Test Method for Vickers Hardness of Metallic Materials," *Filadelfia (EE. UU.): American Society for Testing and Materials*, 1997.

- [115] E. ASTM, "Standard test methods for tension testing of metallic materials," Annual book of ASTM standards. ASTM, 2001.
- [116] A. Standard, "E23-09: Standard Test Method for Notched Bar Impact Testing of Metallic Materials," Annual Book of ASTM Standards, ASTM, West Conshohocken, PA, 2009.
- [117] T. Maitland and S. Sitzman, Electron backscatter diffraction (EBSD) technique and materials characterization examples vol. 14: Springer Berlin, 2007.
- [118] E. Bonnevie, G. Ferriere, A. Ikhlef, D. Kaplan, and J. Orain, "Morphological aspects of martensite–austenite constituents in intercritical and coarse grain heat affected zones of structural steels," *Materials Science and Engineering: A*, vol. 385, pp. 352-358, 2004.
- [119] H. Ikawa, H. Oshige, and T. Tanoue, "Effect of martensite-austenite constituent on HAZ toughness of a high strength steel," *Transactions of the Japan Welding society*, vol. 11, pp. 87-96, 1980.
- [120] A. ASTM, "370," Standard test methods and definitions for mechanical testing of steel products, 2003.
- [121] A. Srivastava, L. Ponson, S. Osovski, E. Bouchaud, V. Tvergaard, and A. Needleman, "Effect of inclusion density on ductile fracture toughness and roughness," *Journal of the Mechanics and Physics of Solids*, vol. 63, pp. 62-79, 2014.
- [122] Y. Han, J. Shi, L. Xu, W. Cao, and H. Dong, "Effect of hot rolling temperature on grain size and precipitation hardening in a Ti-microalloyed low-carbon martensitic steel," *Materials Science and Engineering: A*, vol. 553, pp. 192-199, 2012.
- [123] Y. M. Kim, H. Lee, and N. J. Kim, "Transformation behavior and microstructural characteristics of acicular ferrite in linepipe steels," *Materials Science and Engineering: A*, vol. 478, pp. 361-370, 2008.
- [124] L. Fan, D. Zhou, T. Wang, S. Li, and Q. Wang, "Tensile properties of an acicular ferrite and martensite/austenite constituent steel with varying cooling rates," *Materials Science and Engineering: A*, vol. 590, pp. 224-231, 2014.
- [125] B. Guo, L. Fan, Q. Wang, Z. Fu, Q. Wang, and F. Zhang, "Effect of Finish Rolling Temperature on the Microstructure and Tensile Properties of Nb–Ti Microalloyed X90 Pipeline Steel," *Metals*, vol. 6, p. 323, 2016.
- [126] Y. W. Kim, J. H. Kim, S.-G. Hong, and C. S. Lee, "Effects of rolling temperature on the microstructure and mechanical properties of Ti–Mo microalloyed hot-rolled high strength steel," *Materials Science and Engineering: A*, vol. 605, pp. 244-252, 2014.
- [127] R. Bjorhovde, M. F. Engestrom, L. G. Griffis, L. A. Kloiber, and J. O. Malley, *Structural Steel Selection Considerations: A Guide for Students, Educators, Designers, and Builders*: ASCE Publications, 2001.

- [128] M. Enomoto, "The mechanisms of ferrite nucleation at intragranular inclusions in steel," in THERMEC 97: International Conference on Thermomechanical Processing of Steels and Other Materials, 1997, pp. 427-431.
- [129] T. Kimura, A. Ohmori, F. Kawabata, and K. Amano, "Ferrite grain refinement through intra-granular ferrite transformation on VN precipitates in TMCP of HSLA steel," in THERMEC 97: International Conference on Thermomechanical Processing of Steels and Other Materials, 1997, pp. 645-651.
- [130] T. Ochi, T. Takahashi, and H. Takada, "Improvement of the toughness of hot forged products through intragranular ferrite formation," in 30 th Mechanical Working and Steel Processing Conference., 1988, pp. 65-72.
- [131] T. Hanamura, H. Shibata, Y. Waseda, H. Nakajima, S. Torizuka, T. Takanashi, et al., "In-situ observation of intragranular ferrite nucleation at oxide particles," ISIJ international, vol. 39, pp. 1188-1193, 1999.
- [132] F. Ishikawa, T. Takahashi, and T. Ochi, "Intragranular ferrite nucleation in medium-carbon vanadium steels," Metallurgical and Materials Transactions A, vol. 25, pp. 929-936, 1994.
- [133] S. Jones and H. K. Bhadeshia, "Competitive formation of inter-and intragranularly nucleated ferrite," Metallurgical and Materials Transactions A, vol. 28, pp. 2005-2013, 1997.
- [134] F. Ishikawa and T. Takahashi, "The formation of intragranular ferrite plates in medium-carbon steels for hot-forging and its effect on the toughness," ISIJ international, vol. 35, pp. 1128-1133, 1995.
- [135] A. DeArdo, C. Garcia, W. Gao, and M. Hua, "Thermomechanical processing of microalloyed steels: grain refinement revisited," in International Conference on Thermomechanical Processing: Mechanics, Microstructure and Control, The University of Sheffield, England, 2002, pp. 97-106.
- [136] T. Kimura, F. Kawabata, K. Amano, A. Ohmori, M. Okatsu, K. Uchida, et al., "Heavy gauge H-shapes with excellent seismic-resistance for building structures produced by the third generation TMCP," in International Symposium on Steel for Fabricated Structures, 1999, pp. 165-171.
- [137] H. Satoh, S. Yoshida, K. Yamamoto, and M. Kurokawa, "Thermo-Mechanical Control Process for H-shapes and its characteristics," in 41 st Mechanical Working and Steel Processing Conference, 1999, pp. 911-922.
- [138] S. A. Saltykov, "Stereometric metallography," Metallurgizdat, Moscow, vol. 267, 1958.
- [139] C. S. Smith and L. Guttman, "Measurement of internal boundaries in three-dimensional structures by random sectioning," Trans. Aime, vol. 197, pp. 81-87, 1953.

- [140] Q. Microscopy, "RT DeHoff and FN Rhines, eds," ed: McGraw-Hill, New York, NY, 1968.
- [141] E. Underwood, "Quantitative Stereology Addison," ed: Wesley Publishing Company, Reading, Massachusetts, 1970.
- [142] G. Speich, "Formation of Ferrite From Controlled Rolled Austenite," Proc. Phase Transformations in Ferrous Alloys,(Warrendale, PA: TMS-AIME, 1984), pp. 341-390.
- [143] N. Kang, Y. Lee, S. Byun, K. Kim, J. Chung, and K. Cho, "Quantitative analysis of microstructural and mechanical behavior for Fe-0.1 C-(V, Nb) steels as a function of the final rolling temperature," Materials Science and Engineering: A, vol. 499, pp. 157-161, 2009.
- [144] H. K. Sung, S. S. Sohn, S. Y. Shin, S. Lee, N. J. Kim, S. H. Chon, et al., "Effects of finish rolling temperature on inverse fracture occurring during drop weight tear test of API X80 pipeline steels," Materials Science and Engineering: A, vol. 541, pp. 181-189, 2012.
- [145] T. Araki, I. Kozasu, H. Tankechi, K. Shibata, M. Enomoto, and H. Tamehiro, "Atlas for Bainitic microstructures," ISIJ, Tokyo, Japan, pp. 1-100, 1992.
- [146] T. A. a. K. SHIBATA, in HSLA Steels '95, Beijing, China, 1995, p. 13.
- [147] P. Cizek, B. Wynne, C. H. Davies, B. Muddle, and P. Hodgson, "Effect of composition and austenite deformation on the transformation characteristics of low-carbon and ultralow-carbon microalloyed steels," Metallurgical and Materials Transactions A, vol. 33, pp. 1331-1349, 2002.
- [148] E. Wilson, "The $\gamma \rightarrow \alpha$ transformation in low carbon irons," ISIJ international, vol. 34, pp. 615-630, 1994.
- [149] G. Krauss and S. W. Thompson, "Ferritic microstructures in continuously cooled low-and ultralow-carbon steels," ISIJ international, vol. 35, pp. 937-945, 1995.
- [150] T. Massalski, "Massive transformations," PAPER FROM PHASE TRANSFORMATIONS, ASM. 1970, 433-486, 1970.
- [151] M. Hillert, :Metall. Trans. A, p. 411, 1984.
- [152] M. Olasolo, P. Uranga, J. Rodriguez-Ibabe, and B. López, "Effect of austenite microstructure and cooling rate on transformation characteristics in a low carbon Nb-V microalloyed steel," Materials Science and Engineering: A, vol. 528, pp. 2559-2569, 2011.
- [153] S. Zajac, V. Schwinn, and K. Tacke, "Characterisation and quantification of complex bainitic microstructures in high and ultra-high strength linepipe steels," in Materials Science Forum, 2005, pp. 387-394.

- [154] C.-P. Reip, M. Frommert, and M. Reifferscheid, "EBSD-Analysis of non-polygonal ferrite microstructures of HSLA steel."
- [155] L. Kubin and A. Mortensen, "Geometrically necessary dislocations and strain-gradient plasticity: a few critical issues," *Scripta materialia*, vol. 48, pp. 119-125, 2003.
- [156] N. Isasti, D. Jorge-Badiola, J. Alkorta, and P. Uranga, "Analysis of Complex Steel Microstructures by High-Resolution EBSD," *JOM*, vol. 68, pp. 215-223, 2016.
- [157] V. H. P., "Text Microstruct," 1988.
- [158] N. Hansen, "Hall–Petch relation and boundary strengthening," *Scripta Materialia*, vol. 51, pp. 801-806, 2004.
- [159] R. Davies, "Early stages of yielding and strain aging of a vanadium-containing dual-phase steel," *Metallurgical Transactions A*, vol. 10, pp. 1549-1555, 1979.
- [160] A. H. Cottrell and B. Bilby, "Dislocation theory of yielding and strain ageing of iron," *Proceedings of the Physical Society. Section A*, vol. 62, p. 49, 1949.
- [161] R. Grylls, S. Banerjee, S. Perungulam, R. Wheeler, and H. Fraser, "On the discontinuous yielding phenomena observed in a Nb□Ti□Al alloy," *Intermetallics*, vol. 6, pp. 749-752, 1998.
- [162] A. Bannister, J. R. Ocejo, and F. Gutierrez-Solana, "Implications of the yield stress/tensile stress ratio to the SINTAP failure assessment diagrams for homogeneous materials," *Engineering Fracture Mechanics*, vol. 67, pp. 547-562, 2000.
- [163] S. Y. Han, S. S. Sohn, S. Y. Shin, J.-h. Bae, H. S. Kim, and S. Lee, "Effects of microstructure and yield ratio on strain hardening and Bauschinger effect in two API X80 linepipe steels," *Materials Science and Engineering: A*, vol. 551, pp. 192-199, 2012.
- [164] Q. Yong, "Secondary phases in steels," *Metallurgical Industry Press, Beijing*, p. 83, 2006.
- [165] E. ERİŞİR, "Strain induced precipitation in microalloyed steels containing Nb, Ti and V," 2012.
- [166] F. Pickering and T. Gladman, "Metallurgical developments in carbon steels," *ISI Special Report*, vol. 81, 1963.
- [167] N. Isasti, D. Jorge-Badiola, M. Taheri, and P. Uranga, "Microstructural and precipitation characterization in Nb-Mo microalloyed steels: Estimation of the contributions to the strength," *Metals and Materials International*, vol. 20, p. 807, 2014.
- [168] C. Gür and İ. Yıldız, "Non-destructive investigation on the effect of precipitation hardening on impact toughness of 7020 Al–Zn–Mg alloy," *Materials Science and Engineering: A*, vol. 382, pp. 395-400, 2004.

- [169] T. Siwecki, A. Sandberg, and W. Roberts, "Processing Characteristics and Properties of Ti-V-N steels," in Int. Conf. on Technology and Applications of HSLA Steels, American Society of Metals, OH, 1983.
- [170] S. C. Wang, "The effect of titanium and nitrogen contents on the austenite grain coarsening temperature," *Journal of materials science*, vol. 24, pp. 105-109, 1989.
- [171] A. DeArdo, R. Marraccini, M. Hua, and C. Garcia, "CSP Production of Value-Added Niobium Bearing Steels."
- [172] K. Inoue, I. Ohnuma, H. Ohtani, K. Ishida, and T. Nishizawa, "Solubility product of TiN in austenite," *ISIJ international*, vol. 38, pp. 991-997, 1998.
- [173] L. F. Dumitrescu and M. Hillert, "Reassessment of the Solubility of TiC and TiN in Fe," *ISIJ international*, vol. 39, pp. 84-90, 1999.
- [174] T. Gladman, *The physical metallurgy of microalloyed steels* vol. 615: Maney Pub, 1997.
- [175] S. MUKAE, K. NISHIO, and M. KATOH, "Solution of TiN during synthetic weld thermal cycling and heat affected zone toughness in low carbon steels," *Transactions of the Japan Welding Society*, vol. 18, pp. 148-158, 1987.
- [176] W. Yan, Y. Shan, and K. Yang, "Effect of TiN inclusions on the impact toughness of low-carbon microalloyed steels," *Metallurgical and Materials Transactions A*, vol. 37, pp. 2147-2158, 2006.
- [177] D. Fairchild, D. Howden, and W. A. Clark, "The mechanism of brittle fracture in a microalloyed steel: part II. Mechanistic modeling," *Metallurgical and Materials Transactions A*, vol. 31, pp. 653-667, 2000.
- [178] J.-Y. Li and W.-Y. Zhang, "Effect of TiN inclusion on fracture toughness in ultrahigh strength steel," *ISIJ International*, vol. 29, pp. 158-164, 1989.